Master's thesis

NTNU
Norwegian University of Science and Technology
Faculty of Engineering
Department of Marine Technology

Benjamin Hilmar Uteng Berntsen

Spectral wave modelling for determining wave exposure in Norwegian aquaculture

Master's thesis in Marine Technology
Supervisor: Pål Lader
Co-supervisor: Weizhi Wang
June 2021

NTNU
Norwegian University of
Science and Technology

Benjamin Hilmar Uteng Berntsen

Spectral wave modelling for determining wave exposure in Norwegian aquaculture

Master's thesis in Marine Technology
Supervisor: Pål Lader
Co-supervisor: Weizhi Wang
June 2021

Norwegian University of Science and Technology
Faculty of Engineering
Department of Marine Technology

NTNU
Norwegian University of
Science and Technology

Abstract

A sensitivity study was performed on the way the SWAN wave model is applied to site assessment in the Norwegian aquaculture industry. Two locations were chosen for the study. Site assessments were already performed by commercial service providers at both locations, which allowed valuable input from industry actors on their choices when setting up SWAN.

A literature review was conducted to build up the knowledge base required to both set up and analyze results from SWAN. The literature review provided an overview of approximation methods that are implemented in SWAN, and the use of SWAN in Norwegian coastal areas. This was related to the aquaculture industry standard NS9415 and input from industry actors in Norwegian aquaculture. SWAN was found to have limited accuracy in very shallow waters and in locations where diffraction is of importance. However, a qualitative assessment of results at the two sites indicated that SWAN should be suitable for an analysis of wave exposure. Grid resolution, placement of boundary conditions (by reducing computational domain dimensions), and implementation of wind were identified as input parameters that are expected to result in the largest variations in results between industry actors, and were chosen for three separate studies with the following results:

- Increased resolution affected H_s on-site, but due to lack of higher resolved bathymetry data it was not determined if the resolution properly resolved all spatial details.
- Reduced computational domain increased H_s on both sites. With a too small domain, there will be a mismatch between the location where the boundary conditions are measured (datapoint), and where it is placed in the model.
- H_s on-site was dependent on fetch when local wind was implemented in the model. When the fetch exceeded approximately 30 km H_s did not increase anymore, suggesting that the sea state was fully developed at this limit.

The numerical setup used to obtain the results was largely based on the setup of only one industry actor. In addition, it was never investigated how much the parameters actually differ between industry actors, and interpretations from results should therefore be treated with this in mind. The results highlight the sensitivity of the SWAN model, however, and a standardized method to set up SWAN in Norwegian aquaculture may be required to improve accuracy.

Abstrakt

Det ble utført en sensitivitetsstudie på bølgemodellen SWAN, slik den blir brukt for lokalitetsanalyser i norsk akvakultur. To lokasjoner ble valgt for studien. På begge lokasjonene var lokalitetsanalyser allerede gjennomført av kommersielle aktører, noe som muliggjorde verdifulle innspill om valgene de har gjort for oppsettet av SWAN på de to lokasjonene.

En litteraturstudie ble utført for å bygge opp kunnskapen som kreves for å sette opp SWAN og analysere resultatene. Litteraturstudiet ga en oversikt over approksimeringsmetoder som er implementert i SWAN, og bruk av SWAN i norske kystområder. Dette ble relatert til industristandarden i akvakultur NS9415, og innspill fra industriaktører i norsk akvakultur. Det ble funnet ut at SWAN har begrenset nøyaktighet på veldig grunt vann, og på lokasjoner hvor diffraksjon er viktig. En kvalitativ vurdering av resultatene på de to lokasjonene tydet imidlertid på at SWAN er egnet på de to lokasjonene. Oppløsning av gridden, plassering av grensebetingelser (ved å redusere dimensjonene til gridden), og implementering av vind ble identifisert som parametrene som vil gi størst variasjon i resultatene mellom industriaktører, og ble valgt til tre separate studier med følgende resultater:

- Økt oppløsning påvirket H_s på begge lokalitetene, men pga. manglende bunndata med høyere oppløsning ble det aldri fastslått om romlige detaljer ble tilstrekkelig oppløst.
- Reduserte grid-dimensjoner førte til overapproksimering av H_s på lokalitetene. Med for små grid-dimensjoner vil ikke plasseringen der grensebetingelsene måles stemme overens med hvor de plasseres i modellen.
- H_s på lokalitetene viste seg å være avhengig av fetchlengden når lokale vindforhold ble implementert i modellen. Når fetch overskrider 30 km økte ikke H_s mer, noe som tyder på at sjøtilstanden var fullt utviklet ved denne fetchlengden.

The numeriske oppsettet som ga resultatene ovenfor ble i stor grad basert på oppsettet fra kun én industriaktør. I tillegg ble det aldri undersøkt hvor mye de tre parametrene varierer mellom aktørene. Tolkninger fra resultatene bør derfor ta dette i betrakning. Resultatene fremhever imidlertid sensitiviteten til SWAN, og en standardisert metode for å sette opp SWAN innen lokalitetsanalyser i norsk akvakultur kan være nødvendig for å øke nøyaktigheten.

Preface

This master thesis has been written at the end of a five year integrated Master of Science degree in Marine Technology at Norwegian University of Science and Technology (NTNU). The thesis counts as 100% of the workload in a semester, corresponding to 30 credits.

I chose the topic after inspiration from two courses I had in the autumn of 2020. TBA4270 Coastal Engineering introduced me to wave modelling with SWAN, whereas TMR4140 Design of Marine Production Plants gave me an overview of how wave modelling was used in site assessments in Norwegian aquaculture.

I would like to express my sincerest appreciation to my supervisor Pål Lader, professor at Department of Marine Technology at NTNU, who has been essential for the progress of this thesis by sharing his knowledge and experience. I am very grateful for the great interest you have showed in my thesis, Pål, and for all the extra time you have set aside to help me.

Thank you to my co-supervisor Weizhi Wang, postdoctoral fellow at Department of Civil and Environmental Engineering at NTNU, who has been an important sparring partner for the technicalities of setting up the SWAN model, and assessment of the results. I am also very grateful to Weizhi for giving me the opportunity to work with this topic further, as we are going to compare the results from this thesis with a phase-resolved model.

Thank you to Multiconsult and Åkerblå who has shared their site assessments with me. I would especially like to express my gratitude to Edmond Hansen and Juliane Borge at Multiconsult who have helped me narrow the scope of my thesis, and shared from their experience of setting up the SWAN model for site assessments in Norwegian aquaculture.

I hope this thesis inspires for further work on the subject, and I think a close collaboration between the Department of Civil and Environmental Engineering and Department of Marine Technology can provide a good platform for further studies.

Benjamin Hilmar Uteng Berntsen
09/06/2021, Trondheim

Nomenclature

α	Phase shift of wave
α_{BJ}	Tunable coefficient for surf-breaking source term
δ_A	Diffraction parameter
γ	Peak enhancement factor for JONSWAP spectrum
γ_B	Breaker index of surf-breakers
λ	Wave length
ω	Angular frequency
ϕ	Phase shift between waves
ρ_s	Density of sea water
σ	Wave frequency relative to ambient current
θ	Wave direction.
θ_{peak}	Peak wave direction.
θ_{wind}	Wind direction.
ζ	Sea surface elevation
ζ_A	Wave amplitude
C_g	Group velocity of a wave with diffraction and depth-induced refraction
C_w	Phase velocity of a wave with diffraction and depth-induced refraction
c_w	Phase velocity of a wave
c_x	The phase velocity in x-direction
c_y	The phase velocity in y-direction
c_σ	Rate of change of a wave's relative frequency (current-induced refraction)

$c_{\theta,\,dep}$	Turning rate because of depth-induced refraction
$c_{\theta,dif}$	Turning rate because of diffraction
$c_{\theta,\,cur}$	Turning rate because of ambient current
$c_{\theta,\,ref}$	Total turning rate because of current-induced and depth-induced refraction
c_g	Absolute group velocity of a wave
D	Directional spreading function
d	Water depth
d_{setup}	Water depth including the wave-induced setup
D_{surf}	Average dissipation ratio for surf-breaking
dd	Directional spreading coefficient
E	Energy density spectrum
E_{tot}	Total energy of a wave per unit area
g	Gravitational acceleration
H_{surf}	Max wave height before depth-induced wave breaking, surf breakers, occur
k	Wavenumber
K_{bfr}	Bottom friction coefficient
m_n	The n'th moment of the energy density spectrum
N	Action density
p	Pressure
S_{bfr}	Source term for bottom friction.
S_{diss}	Source term for total dissipation
S_{ice}	Source term for sea ice dissipation.
S_{in}	Source term for wave generation by wind
S_{mud}	Source term for mud dissipation.
S_{nl3}	Source term for triad wave-wave interactions
S_{nl4}	Source term for quadruplet wave-wave interactions
S_{nl}	Source term for total nonlinear wave-wave interaction
S_{surf}	Source term for surf-breaking waves.

S_{tot}	Total source term
S_{turb}	Source term for turbulence dissipation.
S_{wc}	Source term for white capping.
T	Wave period
t	Time
T_p	Peak wave period
U_{10}	Wind speed 10 m over the water surface.
V	Ambient current velocity

Contents

List of Figures

List of Tables

Chapter 1

Introduction

In this thesis, a sensitivity study is conducted on the spectral wave model SWAN, as it is applied in Norwegian aquaculture. SWAN is used by the aquaculture industry to analyze wave exposure at aquaculture sites, so that suitable sites are used, and that design is adapted to withstand wave conditions. A sensitivity study may reveal potential differences in analyses between actors, which, in turn, may highlight main sources of error if SWAN is not correctly configured.

Aquaculture plays an important role in UN's sustainable development goal to achieve zero hunger. The world population is constantly increasing and, with it, food demand. Even though land-based expansion of production is possible, it may aggravate climate change and compromise ecosystem services (Foley et al., 2005). Most of the increased demand must therefore be covered by increased seafood production. However, wild fish capture in the world's oceans are largely maximized, and the production rate is expected to remain at the same level according to projections for 2018-2030 (FAO, 2020). The increased production must therefore mainly come from aquaculture and The World Bank (2013) projects that by 2030 aquaculture will contribute with 62% of all fish supply in the world. The increase in Norwegian aquaculture production has been one of the success stories that lays foundation for further growth in aquaculture production globally: The technological innovation required to achieve the increased production volume can inspire solutions in other aquaculture industries, thus also creating positive effects on a global scale. The volume of produced salmon and trout in Norway was 1.4 million tonnes in 2019, a 40% increase from 2009 (Fauske, 2020). The vision of the Norwegian seafood industry is to double value creation by 2030, and increased production in aquaculture is a vital part of this vision (Sjømat Norge, 2018).

Increase in aquaculture production has resulted in a lack of sheltered aquaculture locations in Norwegian coastal areas, and new sites are typically located in areas that are more exposed to waves coming in from offshore areas. Compared to traditional sheltered sites, exposed aquaculture sites provide a higher rate of water exchange. This leads to more stable growth conditions from higher oxygen supply, in addition to a greater distribution of waste materials (Kraugerud,

2021). Exposed facilities are also further away from wild salmon in coastal areas, which may help to reduce the negative environmental consequences caused by salmon lice and escapes. On the other hand, the fish farms will be subjected to stronger currents and more energetic waves than where the sheltered locations conventional fish cages are situated (Faltinsen and Shen, 2018). Dimensioning new fish cage design to more demanding environmental conditions will, in turn, increase the importance of estimating wave exposure correctly.

Analyses of wave exposure at Norwegian aquaculture sites must be done according to the prevailing Norwegian standard NS9415 (2009). Each site must be classified with respect to environmental conditions, and for waves this is the significant wave height, H_s, which is the mean height of the 1/3 highest waves, and corresponding peak wave period, T_p, which is the period of the most energetic waves. Each of these parameters must be calculated for waves with a return period of 10 years and 50 years.

NS9415 suggest to use the fetch analysis to estimate wave exposure due to local wind, and Stemsrud (2018) found it to be the most common method used for wind wave estimation in Norwegian aquaculture. The fetch method is done by first finding the length over which the wind blows freely (the fetch length), before approximation formulas or tables given in the standard are used to calculate the significant wave height and peak wave period. According to Lader et al. (2017) the method is crude, as waves from offshore areas, i.e. waves made by distant weather systems, are not included. The effect of bathymetry is also not included - meaning deep water conditions are assumed all over.

The other widely applied method for analyzing wind waves is the numerical wave model SWAN (Stemsrud, 2018). SWAN (*SWAN*, 2020) is an open-source computer model that computes realistic estimates of random, short-crested, wind-generated waves in coastal and inland waters. SWAN uses a spectral method, meaning that the wave field is represented as a spatial distribution of wave energy, which in turn is based on linear wave theory. Contrary to the fetch analysis, SWAN enables analyses which accounts for the effect of swell and bathymetry, and is therefore a more comprehensive tool which will give more accurate results in areas where such effects are important. There are even more comprehensive wave models available, such as the REEF3D (2020) flow model. The balance between computational efficiency and accuracy of results must correspond to the problem at hand, however, and the extensive use of SWAN in Norwegian aquaculture indicates that it fits well with requirements for the vast majority of Norwegian aquaculture sites.

Setting up a SWAN model for a location requires input data and modelling choices. Many of these are not standardized in Norwegian aquaculture, and the results from SWAN simulations may as a consequence differ between actors that conduct site analyses. A sensitivity study of the numerical setup is required to find out which of the parameters has the most impact on the results. Such a study may suggest which parameters are most important to validate and, in turn, include in future standards for Norwegian aquaculture.

There are several published studies on use of SWAN in Norwegian coastal areas. Stefanakos and Eidnes (2014) showed the use of SWAN in a fjord in Northern Norway. In recent years, Christakos, Furevik, Aarnes, Breivik, Tuomi and Byrkjedal (2020) investigated the importance of wind forcing in fjord wave modelling, whereas Christakos, Björkqvist, Tuomi, Furevik and Breivik (2020) investigated the performance of some of the approximation methods available in SWAN, with respect to typical fjord geometries, and Stefanakos et al. (2020) investigated the importance of boundary conditions in Norwegian coastal areas. In addition, Wang (2020) analyzed the performance of SWAN in areas with very complex topography compared to the potential flow models available in the open source hydrodynamics program REEF3D (REEF3D, 2020). However, a thorough search in literature yields no sensitivity study conducted with a setup comparative to the one used by actors in Norwegian aquaculture. Nor are there studies investigating what input different actors in the industry use.

1.1 Objectives

The main objective of this thesis is **to perform a sensitivity study on the most important parameters of the SWAN wave model applied to site assessment in the Norwegian aquaculture industry.** To achieve this, the following secondary objectives are identified:

1. Identify Norwegian aquaculture locations suitable for a sensitivity study. That is, locations where studies have been conducted by one or more industry and where their assessments when setting up a numerical model at the locations are available.
2. Get a thorough understanding of SWAN by conducting a literature review on the underlying wave theory used to model and approximate wave physics in SWAN.
   (a) Relate the theory to wave modelling in Norwegian coastal areas.
   (b) Relate the theory to NS9415 (2009), in addition to input from industrial actors in Norwegian aquaculture.
3. Choose parameters for a sensitivity study based on findings from literature and input from industry actors, and develop numerical experiments to investigate their influence.
   (a) Establish a numerical setup in SWAN for the chosen locations. The setup should resemble the setups used by industry actors in Norwegian aquaculture and be in line with NS9415 (2009).
4. Investigate the results of the sensitivity study and propose future studies.

1.2 Structure

The remainder of this thesis is organized with regards to the objectives above as follows:

Chapter 2	Objective 1	Two locations are chosen for case studies. The challenging hydrographic characteristics of the locations are described, and their suitability for a case study are evaluated.
Chapter 3	Objective 2	A brief presentation of linear wave theory is given, a prerequisite for spectral wave modelling. Then, a presentation of the underlying concepts of spectral wave modelling, the founding principle of SWAN. The governing equation of SWAN is presented. Relevant approximation methods available in SWAN is presented and discussed with respect to literature on modelling in Norwegian coastal areas. This is followed by an overview of characteristic wave transformation phenomena in coastal waters, and how these typically can be expected to influence wave patterns in Norwegian coastal areas.
Chapter 4	Objective 3	The parameters deemed as suitable for a sensitivity analysis are presented, and the experiments are designed to investigate the influence of each parameter. A numerical setup for the two locations is established on the basis of the literature study in chapter 3.
Chapter 5	Objective 4	Results from the sensitivity study established in chapter 4 is presented.
Chapter 6	All objectives	The results from the two locations will be discussed with regards to the main objective. In addition, an assessment will be made of potential uncertainties of the study with respect to the limitations of SWAN, and the modelling choices. A conclusion on the achievement of the main objective will be given, and suggestions of future studies will be proposed.

Chapter 2

Locations

To conduct a sensitivity study on SWAN in Norwegian aquaculture, suitable sites must be chosen for case studies. Sites in Norwegian coastal areas can in general be split into exposed and sheltered sites. There are no clear distinctions between the two categories, but the term exposed is frequently used for sites where the most common sea state is more energetic than at a sheltered site (Lader et al., 2017). That is, they are more exposed to high-energy waves from offshore areas (swell). There are of course variations in both categories with regards to topography, bathymetry, currents, and wind.

Only a limited number of locations are chosen for the sensitivity study for practical reasons (each site requires pre-processing of data for the numerical setup). Hence, some criteria are established to make sure that the locations are suitable. First and foremost, it is prioritized to look at locations where analyses have already been performed by aquaculture industry actors. This allows for valuable input from the industry actors on how they chose their numerical setup. Moreover, the locations should be exposed. With an increasing trend of exposed aquaculture sites, it is preferred to analyze sites that have the same characteristics as what is expected for new site locations both now and in near future.

Two locations, hereafter called location Alpha and Beta, are chosen. These are showed in figure 2.1 and figure 2.2. The aquaculture site at each location is indicated with red dots. SWAN simulations have been run by Multiconsult (Vaardal-Lunde et al., 2018) at location Alpha, and by both Multiconsult (Borge and Nilsen, 2021) and Åkerblå (Hestnes and Torkildson, 2021) at location Beta. The two sites were chosen in consultation with Edmond Hansen and Juliane Borge at Multiconsult, and Pål Lader and Weizhi Wang at NTNU, and are regarded as suitable candidates based on the chosen criteria.

Location Alpha is exposed to swell from western directions, whereas location Beta is exposed to swell from northwestern directions. Since there are large open fetch in both areas, it is also expected to be areas with high wind velocity that will impact the incoming swell.

Both locations have a bathymetry which is characteristic for the Norwegian coast, where there are fast water depth variations between deep and shallow waters, which is in contrast to the mild water depth gradient as at a typical beach. Moreover, both locations have a topography with skerries in proximity of the fish farms, also a typical feature of Norwegian coastal areas. These skerries are north/north-west of the aquaculture sites. Both locations will be described further in chapter 4.1.

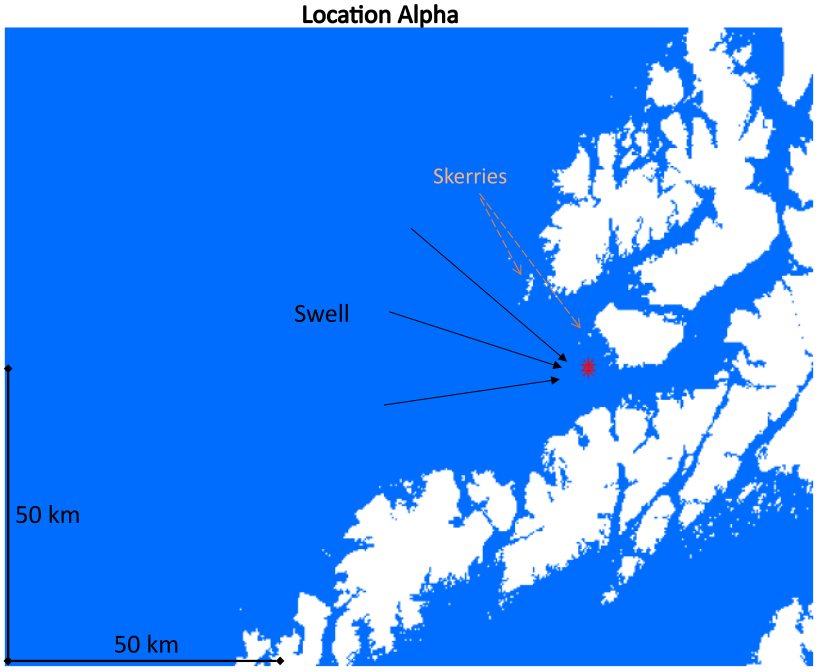

Figure 2.1: Placement of aquaculture site (red) at location Alpha.

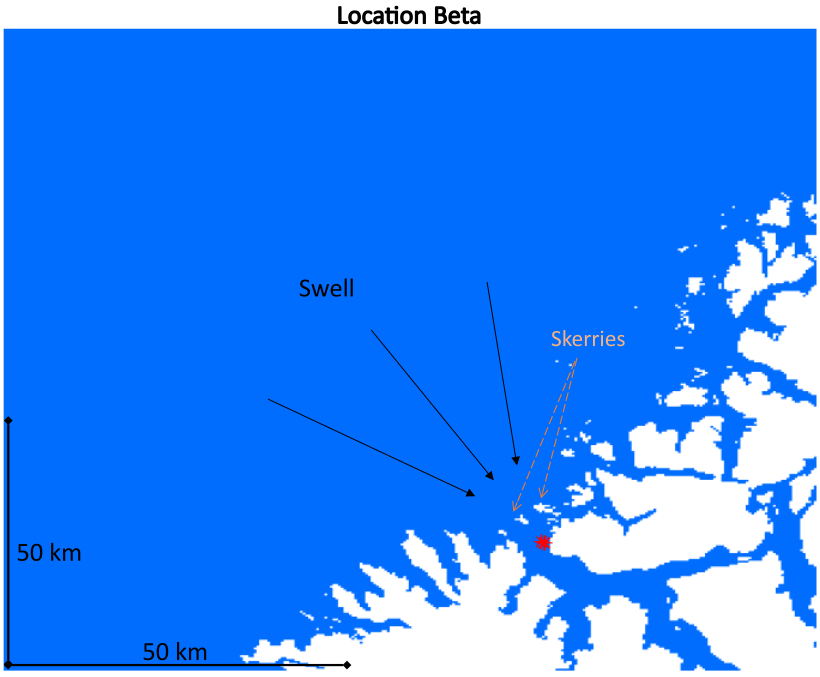

Figure 2.2: Placement of aquaculture site (red) at location Beta.

Chapter 3

Spectral wave modelling in Norwegian aquaculture

Modelling a location with SWAN and analyzing the results requires knowledge of spectral description of wave fields, since SWAN is build around this concept. To set up a numerical model in SWAN for a location, some data must be given as input, and approximation methods of local changes in energy must be chosen. The concept of SWAN will be treated in this chapter, more specifically its treatment of wave energy and wave transformations in coastal waters. This will be related to literature concerning SWAN wave modelling in Norwegian coastal areas, and relevant regulations from NS9415 (2009). The information will lay the foundation for the numerical setup of SWAN for the two locations chosen for a sensitivity study in chapter 2, in addition to being a prerequisite for understanding and analyzing the outputs of the model.

Modelling of waves in coastal waters follows the same principals as in deep water. Every wave component is followed from an input location at the boundary to the output location at the site. On the way all effects of wave propagation, wave-wave interactions, generation and dissipation must be accounted for. SWAN follows an Eulerian approach, meaning that the waves are described by gridding a control volume. In each grid cell the wave's rate of change is described, and computed with the action balance equation. The concept is illustrated with an example of a salmon farming site in Trælvik, Senja in Northern Norway in figure 3.1.

The spectral method used in SWAN implies that the wave field is represented by the wave energy through energy spectra, and the governing equation describes the evolution of energy in the computation area. This is a phase-averaging approach, and the time history of the wave surface elevation can not be represented, contrary to phase-resolving models. It has a much higher computational efficiency however, and is therefore suitable for the large-scale areas that are relevant in the majority of aquaculture wave exposure analyses. SWAN is a third-generation wave model, which means that the energy spectrum is set at the boundary, but it is free to develop inside the computational domain.

Figure 3.1: The concept of SWAN modelling shown for a site location in Trælvik, Senja in Northern Norway. For illustrative purposes.

Information about the location is provided through input data to SWAN. The following input will be covered in this chapter:

- Boundary condition. The energy spectrum set at the boundary of the grid is referred to as the boundary condition. Treated in chapter 3.3.
- Wind. Velocity and direction. Increases energy in the wave field. Covered in chapter 3.5.1.
- Current. Velocity and direction. Induces refraction. Covered in chapter 3.6.2.
- Bathymetry/topography. Provided through a 3-coordinate system (x,y,z) where x and y are the coordinates in the plane and z is the depth from a chosen reference point. It is required input data to run the model, and the effect of objects (skerries/shoals etc.) and depth on energy and transformations of the wave field will be a recurring topic throughout this chapter. The amount of data points (x,y,z) per area is referred to as the *bathymetry resolution*.

The theory of the SWAN model and the underlying physics in this chapter is based on the work of Holthuijsen (2007) and *SWAN* (2020). Only the stationary mode of SWAN will be treated in this thesis.

3.1 Linear wave theory in coastal waters

Linear wave theory must be valid to derive physical properties and characteristics of wind-generated waves from the energy spectra of the wave field. It is based on two fundamental equations and four boundary equations which describes the kinematic and dynamic relationships of the waves. The equations are presented in Appendix A.

In linear wave theory it is assumed that the amplitude of the waves are small relative to the wave length and depth so that nonlinear effects can be neglected. Hence, steep waves and/or waves in very shallow water do not follow linear wave theory. If the nonlinear effects are weak or only occur sporadic however, then the linear wave theory can be applied on a larger scale with small nonlinear correction. Depth-induced wave breaking (surf-breaking) is an example that locally has a highly nonlinear effect, but on a larger scale, i.e. averaged over a large number of waves, the nonlinear effect is weak and the related energy dissipation can be treated with linear wave theory.

Further, it is assumed that sea water is an ideal fluid and that the forces on the water particles are induced only by gravitation. The assumption of ideal fluid entails that the water must be incompressible with constant density, inviscid, and irrotational water particles. In addition the water body is assumed to be continuous. A brief discussion of the assumptions are presented in Appendix A.

The assumptions and limitations to the theory is thoroughly covered in other literature, and will not be discussed in detail here. See e.g. (Holthuijsen, 2007, chapter 5) for a more in-depth coverage.

A wave propagating in positive x-direction follows a harmonic motion:

$$\zeta(x,t) = \zeta_A cos(\omega t - kx + \alpha), \tag{3.1}$$

where k is the wavenumber of the wave in its propagation direction, x, ζ_A is the wave amplitude, ω is the angular frequency, α is the phase shift.

Combination of the boundary conditions described in Appendix A gives the dispersion relationship

$$\omega^2 = kg\tanh(kd), \tag{3.2}$$

for the harmonic wave described by (3.1). The dispersion relates the angular frequency, ω, to the wavenumber, k, and the depth, d.

The phase velocity for a wave with wave length λ and period T is then

$$c_w = \frac{\lambda}{T} = \frac{\omega}{k} = \frac{g}{\omega}\tanh(kd). \tag{3.3}$$

The velocity of the wave envelope (group velocity) is essential in wave modelling, as it will be the velocity at which energy is conveyed along the wave. At an arbitrary depth this is

$$c_g = \frac{\partial \omega}{\partial k} = \frac{c_w}{2}\left(1 + \frac{2kd}{\sinh(2kd)}\right). \tag{3.4}$$

As a result of dispersion, the group velocity of low-frequency waves will be higher than high-frequency waves, which is why waves from offshore areas have a low frequency (more in chapter 3.3).

The wave theory in coastal waters must account for some of the complex conditions introduced by finite depth and topography, and assumptions of these affect how and where SWAN should be used. More in chapter 3.6.

3.2 Energy density spectrum

The energy density spectrum, hereafter energy spectrum, is the fundamental concept of SWAN and describes the energy in a wave field distributed over wave directions, θ, and wave frequencies, ω.

From linear wave theory the surface elevation ζ at a point can be interpreted as the sum of a large number (N) of harmonic waves

$$\zeta(t) = \sum_{i=1}^{N} \zeta_{A_i} cos(\omega_i t + \alpha_i), \tag{3.5}$$

where ζ_{A_i} ω_i, and α_i is the wave amplitude, angular frequency, and phase shift of wave component i respectively. The total energy in N wave components per unit area is then

$$E_{tot} = \sum_{i=1}^{N} \frac{1}{2}\rho_s g {\zeta_{A_i}}^2, \tag{3.6}$$

where ρ_s is sea water density, g is the gravitational acceleration. The total energy per unit area can also be distributed over the wave frequency and direction

$$E_{tot} = \int_0^{2\pi} \int_0^{\infty} E(\omega, \theta) \mathrm{d}\omega \mathrm{d}\theta, \tag{3.7}$$

where $E(\omega, \theta)$ is the energy density spectrum. Therefore, $E(\omega, \theta)$ is a measure of the energy in a wave distributed over its angular frequency ω and direction θ.

The energy spectrum is often presented for all directions in a one-dimensional spectrum:

$$E(\omega) = \int_0^{2\pi} E(\omega, \theta) \mathrm{d}\theta.$$

It can be derived (see e.g. (*SWAN*, 2020, chapter 2.1)) that the energy spectrum represents all physics of the wave-field as long as the ocean surface elevation ζ follows a stationary, Gaussian process, in addition to the initial assumption of linear wave theory. All results from SWAN concerning the wave-field are therefore obtained from $E(\omega, \theta)$, and often through the n'th moment of the spectrum which is defined as

$$m_n = \int_0^{\infty} \omega^n E(\omega) \mathrm{d}\omega. \tag{3.8}$$

See *SWAN: User manual* (2016) Appendix A, for definitions of all variables.

Note that the energy density spectrum can also be given as a function of frequency, f, instead of angular frequency, ω. These will of course give the same total energy, and are related through

$$E(\omega, \theta) = \frac{1}{2\pi} E(f, \theta). \tag{3.9}$$

For more information on the mathematical characteristics of the energy spectrum, see e.g. Newland (2012).

3.3 Boundary condition

The boundary condition is the wave spectrum set at the boundary of the grid, which is typically a parametric offshore wave spectrum.

The required parameters at the boundary can be obtained through *in situ* buoy measurements, but measurement campaigns are expensive (Stefanakos et al., 2020). A useful alternative is a type of modeling which Fergestad et al. (2018) refer to as Generation Scale Modeling. A generation scale model is also a spectral model and has a similar governing equation as will be presented for SWAN later on. Its calculation method is adapted to oceanic scale however, and is consequently less efficient and robust than SWAN in coastal waters. Two well-established models are WAM (Wamdi Group, 1988) and WaveWatch III (Tolman et al., 2009). An example of SWAN setup is given in figure 3.2, where Stefanakos and Eidnes (2014) set up SWAN to run in three consecutive runs in Nordfold in Northern Norway, where the input to the first run is from a WAM datapoint in the south-west corner of the figure. Stefanakos et al. (2020) showed the importance of setting these offshore boundaries correct with respect to various methods of reconstructing the input spectra from generation scale models.

In SWAN, the form of the wave spectrum on the boundary of the computation grid can be chosen

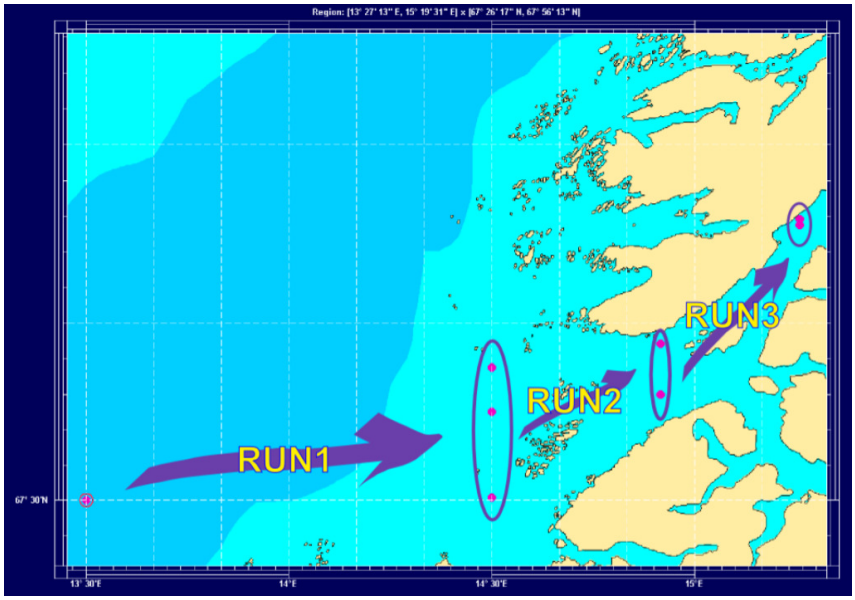

Figure 3.2: Setup of consecutive runs of SWAN model with input from a WAM datapoint in the south-west corner (Stefanakos and Eidnes, 2014).

between JONSWAP (Joint north Sea WAve Project), PM (Pierson-Moskowitz), Gaussian, or manually fitted spectrum. JONSWAP (Hasselmann et al., 1973) has proved to be a good fit for wind-generated waves for the vast majority of relevant fetch lengths. The fetch length is the length over which the wind blows without obstruction, and thus generate waves. JONSWAP follows a generic shape with one peak, but the *peakedness* of the spectrum can be tuned through the peak enhancement factor, γ. That is, for a high value of γ the spectrum will be more narrow and have a higher peak. The JONSWAP spectrum is also the standardized spectrum that shall be used according to the technical standard NS9415 (2009).

The SWAN the energy density spectrum given as input is described through the one-dimensional energy spectrum E(f), and a directional spreading coefficient, (*SWAN: User manual*, 2016)

$$E(f,\theta) = E(f) \cdot D(f,\theta(f)), \tag{3.10}$$

where $\theta(f)$ is the angle between mean wave direction and the direction at a frequency f. $D(f,\theta)$ must satisfy the condition

$$\int D(f,\theta)d\theta = 1 \tag{3.11}$$

Moreover the directional spreading of the wave is given as

$$D(f,\theta) = Q\cos^{dd}(\theta(f)), \tag{3.12}$$

where Q is a normalization factor that ensures (3.11) holds, see (Young, 1999, chapter 5.5) for a more thorough explanation. Here, the tunable coefficient is the directional spreading coefficient,

dd.

In this thesis, the computational areas at both locations are chosen so large that the boundaries are offshore, and the boundary condition is assumed to have the form as a spectrum for swell[1]. Swell is developed by distant weather systems in offshore areas. That is, it starts off as a wind sea (generated by local wind), with waves distributed over a large interval of directions and frequencies. As the waves travel over large distances from offshore to coastal areas, dispersion cause low-frequency waves to travel faster than high-frequency waves (frequency-dispersion). Moreover, the waves will disintegrate over the initial interval of directions from the storm (direction-dispersion). As a result, a swell energy spectrum is typically very narrow in direction, and has a sharper peak at a lower frequency than that of wind sea. A sketch of typical swell and wind sea spectra are given in figure 3.3.

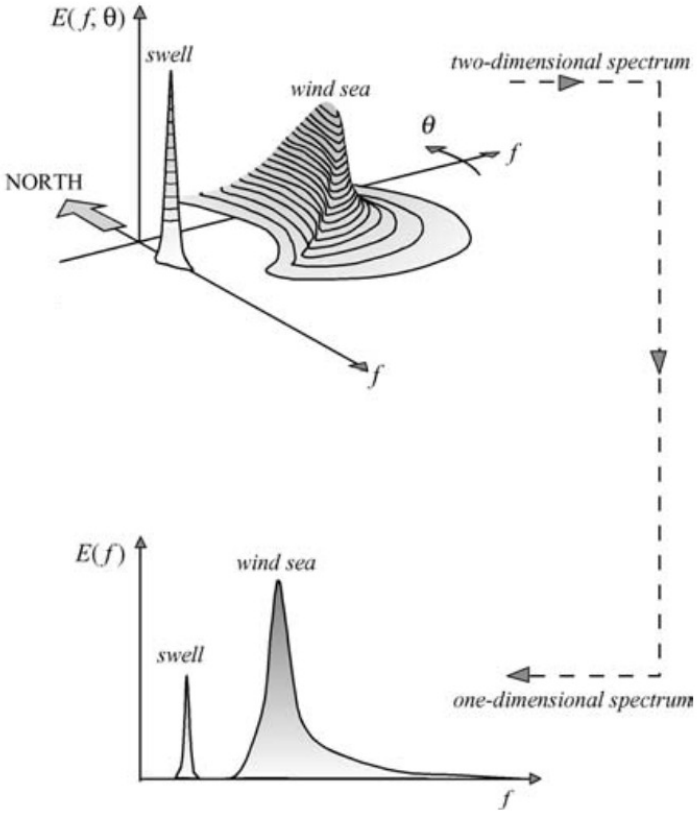

Figure 3.3: The energy spectrum for swell and wind sea (Holthuijsen, 2007).

As seen from chapter 2, swell should be an important part of the wave environment at location Alpha and Beta, where the offshore waves can propagate directly towards the aquaculture location without traveling around any obstacles to reduce its energy.

To obtain accurate results, the computational domain should be large enough so the input spec-

[1]This is a simplification however, more on that in chapter 4.

trum on the boundary is representative. That is, the spectrum should not be changed from the measured point (e.g. a WAM datapoint) to the boundary of the computational area by dissipation, wind, non-linear wave-wave interactions, or wave transformation. This is illustrated with an example for the Trælvik site in figure 3.4. These effects could change the spectrum between the measuring point and the boundary of the computational area. As a result, parameterization of waves at the measuring point may not be representative for the waves at the boundary. Personal communication with Edmond Hansen at Multiconsult revealed that there are no standardized method reassuring that industry actors running SWAN in Norwegian aquaculture have chosen their computational domain such that the boundary is in-line with a measured point, even though these effects are not studied.

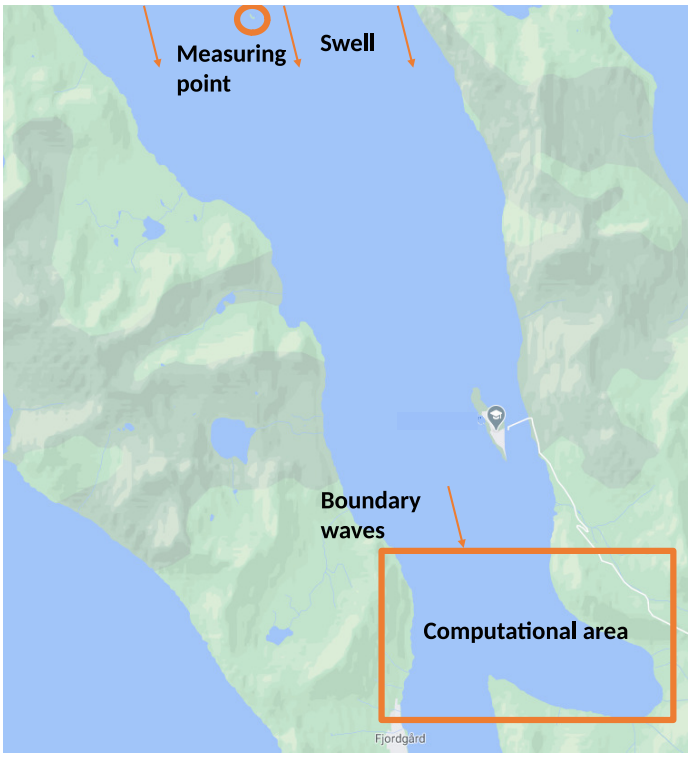

Figure 3.4: An example where the waves at the measuring point is potentially not representative for the boundary waves (Google Maps).

3.4 Governing equation

The action balance equation is the governing equation of SWAN, and relates all variables in the model. It is given as

$$\boxed{\frac{\partial N}{\partial t} + \frac{\partial c_x N}{\partial x} + \frac{\partial c_y N}{\partial y} + \frac{\partial c_\sigma N}{\partial \sigma} + \frac{\partial c_\theta N}{\partial \theta} = \frac{S_{tot}}{\sigma}}, \tag{3.13}$$

where x, y are coordinates, θ is the wave direction, and $N(\sigma, \theta)$ is the action density and S_{tot} is the total source term. σ is the angular wave frequency relative to ambient current. The action density is defined as

$$N(\sigma, \theta) = \frac{E(\sigma, \theta)}{\sigma}, \tag{3.14}$$

where $E(\sigma, \theta)$ is the energy spectrum. The reason for using the action density instead of the energy spectrum is that ambient current will influence the wave, and energy will actually not be conserved. Hence, σ is also substituted for ω in the energy spectrum. This is related to current-induced refraction and is discussed further in chapter 3.6.2.

The left hand side of (3.13) is the kinematic part, i.e. the rate of change of the action density. The first term describes the rate of change between time steps in the simulation, and the rest of the terms on the left hand side gives the rate of change in geographical space, i.e. over a grid cell. This can be interpreted as a new spectrum for each step in time and space. The wave propagation velocities, denoted by c, will be discussed further in chapter 3.6.

On the right hand side of (3.13), the total source term models all the local changes in energy, and is therefore described through the energy spectrum $E(\sigma, \theta)$. In SWAN the source term consists of generation, non-linear wave-wave interactions and dissipation:

$$S_{tot} = S_{in} + S_{nl} + S_{diss}. \tag{3.15}$$

All source terms will be covered in chapter 3.5.

3.5 Source terms

The full structure of the source term in SWAN is illustrated by figure 3.5. In this chapter, an overview of the underlying physics, and the concept for the approximation methods, will be presented for each source term. Literature covering SWAN wave modeling in Norwegian coastal areas, input from industrial actors, and the technical standard NS9415 (2009) will be related to relevant source terms. This will be the foundation for the choice of approximation method for each source term. For the wave generation by wind source term, presented in chapter 3.5.1, the input of wind speed and direction will be covered.

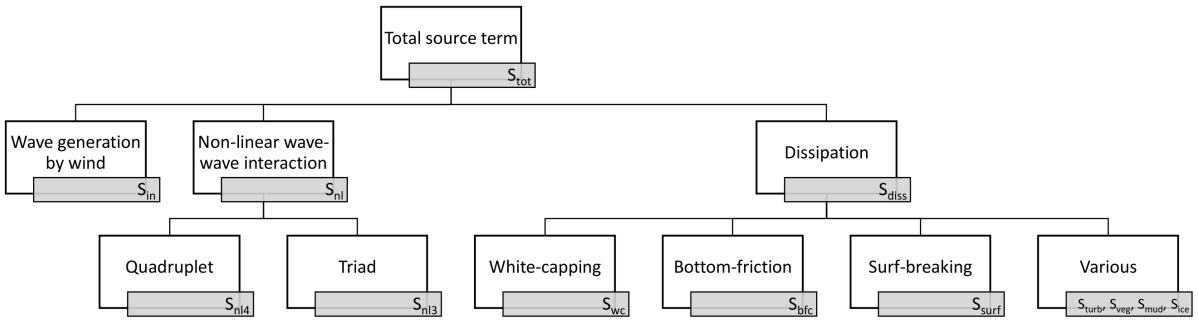

Figure 3.5: The construction of the source term in SWAN.

3.5.1 Wave generation by wind

Wind generates waves and, in turn, increases the energy in the wave field. In SWAN, a local wind field can be set in a chosen area of the computational domain, and is defined through the wind speed 10 m over the water surface, U_{10}, and its angle, θ_{wind}.

The wind consists of many harmonic air-pressure waves in different directions (but propagating in the wind direction in total). Some have the same wave period, velocity and direction as a water-wave component, and will therefore transfer their energy by resonance. That is, the wind induce pressure on the water surface that, in turn, results in generation of waves. The variation of pressure over a flat water surface is illustrated by figure 3.6.

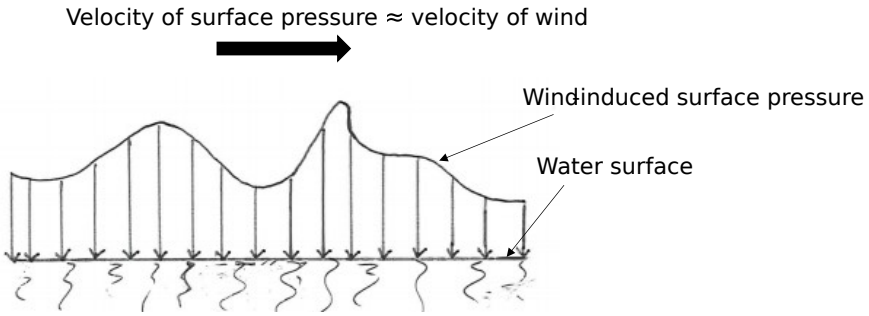

Figure 3.6: Sketch of wind-induced pressure varying over the water surface.

The source term for the generation of waves by wind is written as

$$S_{in}(\sigma, \theta) = \alpha + \beta E(\sigma, \theta), \tag{3.16}$$

where α represents the generation of waves on a flat water surface. As the wave propagates, the waves themselves will have a larger influence on the surface pressure, i.e. the process enforces itself. This is what the second term models, and is described by the energy spectrum and a growth parameter β. Both α and β are functions of the wind's and wave's direction and speed.

They are in SWAN computed from experimental results based on the two input parameters U_{10}, and θ_{wind}.

The form of the wave-generation source term (integrated over all directions) is showed in figure 3.7. The source term will broaden the spectrum, such that an input swell which has a narrow peak, will develop towards a characteristic wind sea.

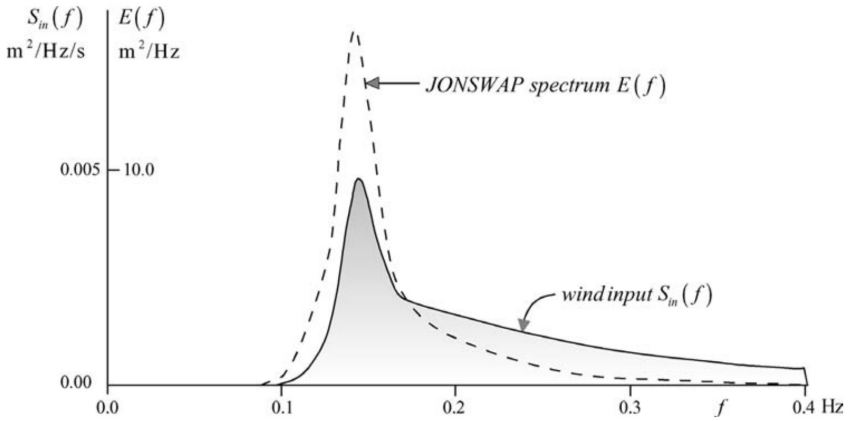

Figure 3.7: Example of a JONSWAP spectrum and resulting wave generation by wind source term (Holthuijsen, 2007).

The approximation method of the wave generation source term is closely connected to that of the white-capping source term that will be described later on. That is, when choosing the approximation method of white-capping it also makes use of a different expression to calculate the wave generation source term. The method described above is used in the standard KOMEN method for wave generation and white-capping, but there are also other methods available in SWAN. The WESTH method is based on laboratory results that has proved more accurate for strong wind conditions (van der Westhuysen et al., 2007), and makes use of an alternative expression for the wave generation source term, proposed by Yan (1987). The WESTH method is discussed further when the white-capping source term is described in chapter 3.5.3.1.

The fetch geometry affects the velocity of the wind. In figure 3.8 an example of an aquaculture site at Frøya, Norway is given. The open sectors are directions with a fetch longer than 40 km in this example. Wind with long fetch will typically result in high wind velocities and thus reinforce the incoming offshore waves from this sector. This will generate a lot of energy to the wave field and thus produce higher waves. Moreover, swell combined with wind waves may create a chaotic wave pattern when the wind and swell have different directions.

Christakos, Furevik, Aarnes, Breivik, Tuomi and Byrkjedal (2020) investigated the role of wind forcing in fjords partly exposed to incoming offshore waves, similar to conditions at location Beta. They found that no wind forcing failed to reproduce realistic significant wave heights and peak periods in both exposed and more sheltered areas. With input from different atmospheric models, they found that choice of wind forcing fields impacts the accuracy of results.

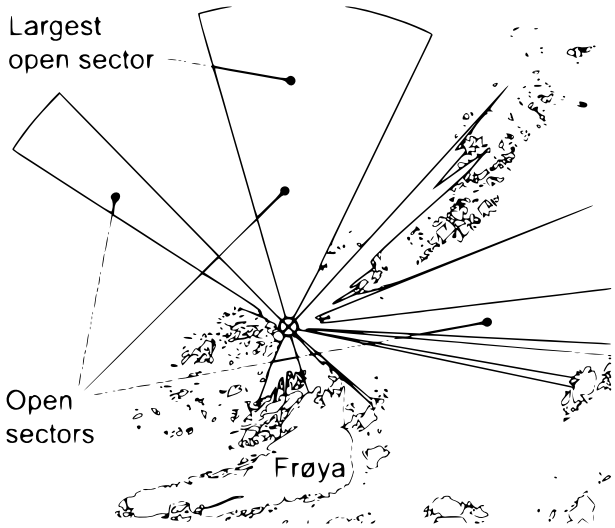

Figure 3.8: Open fetch sectors for an aquaculture site at Frøya in Trøndelag from Lader et al. (2017).

According to NS9415 (2009), the wind standard NS-EN 1991-1-4:2005+NA:2009 (2009) or wind from meteorological stations shall be used to set the wind speed and direction. The wind standard gives a reference value of wind speed for a given direction in a given municipality of Norway, based on extreme value analysis of wind measurements. The reference value is, in turn, adjusted for local terrain through tabulated data. According to personal communication with Edmond Hansen and Juliane Borge from Multiconsult, actors of the industry almost exclusively use the wind standard. The reason is that meteorological weather stations rarely have data for longer than 20 years, and extrapolating those data to e.g. a 50 year return period impose high uncertainty.

As mentioned, the wind field can be set in a chosen area of the computational domain, and Juliane Borge (Multiconsult) suggest that there may be differences between actors as to how large the implemented wind field is. Whereas some actors may set the wind in the full domain, some choose to set it only on a limited area around the site. More on this in chapter 4.

3.5.2 Non-linear wave-wave interaction

The non-linear wave-wave interactions is the energy transfer amongst waves because of resonance. A triad wave-wave interaction is illustrated in figure 3.9: Two waves with different frequencies and directions (wave 1 and wave 2) form a pattern of crests and troughs whose speed, direction and wave number is the sum of wave 1 and 2. A third incoming wave interchange energy with the pattern through resonance if it has the same wave length, velocity and direction as the pattern such as illustrated in the figure. This is triad wave-wave interaction. Triad wave-wave interaction does not occur in deep water because of dispersion, but the same

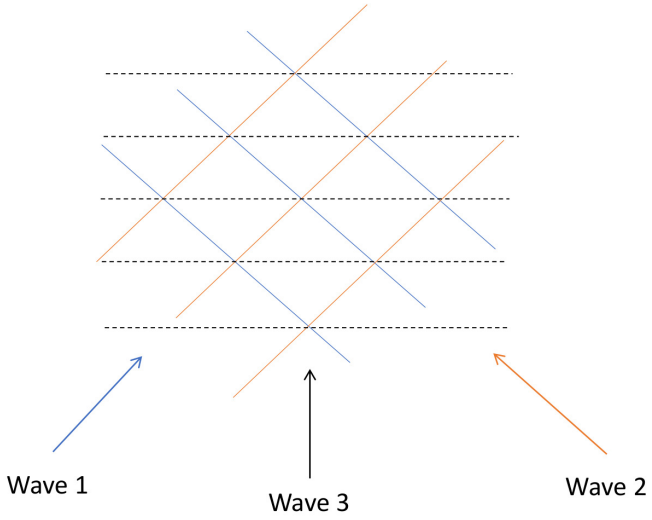

Figure 3.9: Sketch of triad wave-wave interaction.

effect is achievable with two pairs on deep water, where two patterns (four waves) interact. This is quadruplet wave-wave interaction.

The total non-linear source term is therefore because of both quadruplet and triad non-linear wave-wave interactions:

$$S_{nl} = S_{nl4} + S_{nl3}. \tag{3.17}$$

As figure 3.10 shows, the source term will be both negative and positive depending on the frequency. Quadruplets transfer wave energy from the spectral peak to lower frequencies, whereas triads transfer low-frequency waves to higher frequencies. Note that the source terms *redistribute* the energy between waves, i.e. no energy is generated or dissipated from the wave field.

The non-linear wave-wave interaction source terms are in SWAN found by approximation from empirical formulas. The standard approximation method is discrete-interaction approximation (DIA) for quadruplet wave-wave interaction, and lumped-triad approximation (LTA) for triad wave-wave interaction. In addition to the the energy spectrum, $E(\sigma, \theta)$, both approximations

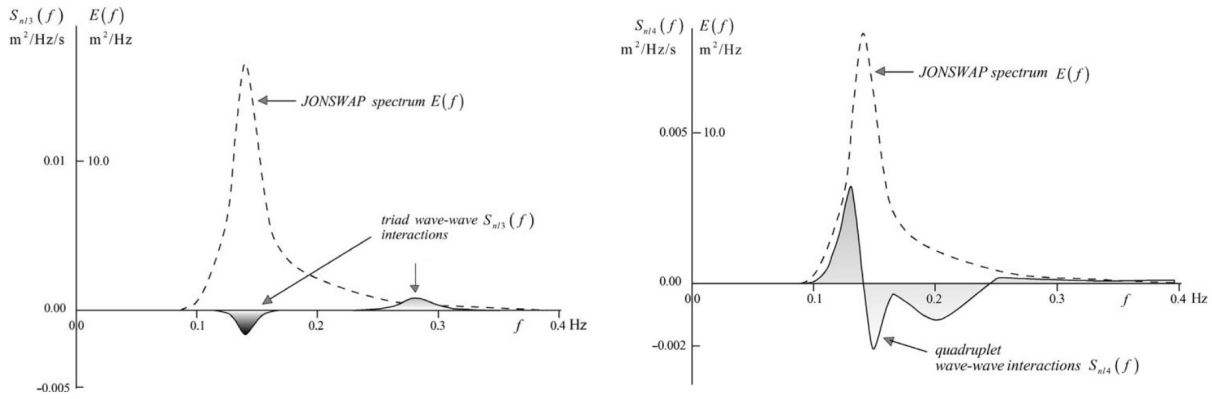

Figure 3.10: Plot of the source term for triad wave-wave interactions S_{nl3} and quadruplet wave-wave interactions S_{nl4} for a JONSWAP spectrum (Holthuijsen, 2007).

will be a functions of the wavenumbers of the interacting waves, as the waves interact through resonance. The expressions will not be presented here, as they are empirical and therefore do not indicate more about the physics than what is already discussed. For more information, see (*SWAN*, 2020, chapter 2.3.4).

Note that the calculation methods can be changed and/or calibrated: The coefficient coupling the energy spectrum and the triad wave-wave interaction can be tuned in SWAN. Moreover, the quadruplet wave-wave interaction can also be approximated by a method called WRT which is more computationally expensive, but is an alternative that might be relevant if quadruplet source term is large compared to other source terms. There is no mention of non-linear wave-wave interactions in NS9415 (2009), and the effects have not been tuned by industrial actors for the two locations considered in this thesis (Vaardal-Lunde et al. (2018), Borge and Nilsen (2021), and Hestnes and Torkildson (2021)). Consequently, tuning of wave-wave interactions are considered out of this thesis' scope, and only the standard methods are applied.

There are often large depth variations in relatively small geographical space in Norwegian coastal areas. Postdoctoral fellow at NTNU, Weizhi Wang (personal communication), therefore recommends that both triads and quadruplets are included. However, the DIA method for quadruplets is limited for unidirectional waves (swell) and it is recommended by the SWAN developers to turn off quadruplets when there is no wind in the simulation (*SWAN*, 2020, chapter 2.3).

3.5.3 Dissipation

The dissipation of energy in SWAN mainly consists of white-capping, bottom friction, and depth induced surf-breaking:

$$S_{diss} = S_{wc} + S_{bfr} + S_{surf}. \tag{3.18}$$

As seen by figure 3.5 there are also some additional source terms in the dissipation, (under

"various"), that will also be covered briefly.

3.5.3.1 White-capping

The wave breakers at sea (deep water) are called white-caps, and the process is referred to as white-capping and typically gives a white foam of air bubbles and water as seen by figure 3.11. From observations it is reasonable to assume that the waves have an upper limit of wave steepness, but whether or not an individual wave breaks seems independent on its steepness under this limit. White-capping is closely related to wind, as it is the driving force of the wave, and the strength and fetch of the wind field is therefore important.

Figure 3.11: Image of white-capping (*CoastalWiki*, 2020).

Wave-breaking is the least understood of all wave affecting processes. Hence, there is much uncertainty concerning the physical mechanisms and its afflicted source term, and van der Westhuysen et al. (2007) argues that the expressions available are mostly speculative. The interpretation in SWAN is that the white cap acts as a pressure pulse downwind (leeward) of the wave crest, as illustrated in figure 3.12.

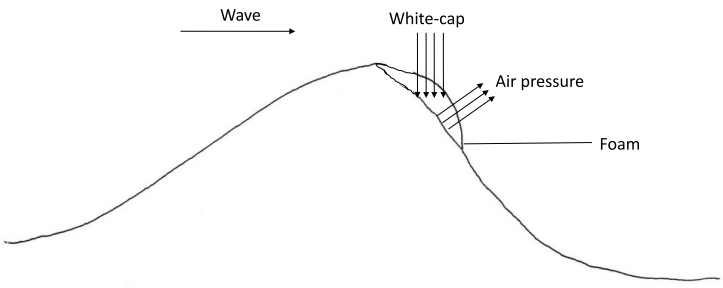

Figure 3.12: Sketch of white-cap pulse pushing down a sea surface which is rising due to air pressure difference. Based on (Holthuijsen, 2007, figure 6.25).

On the leeward side of the crest the air pressure will be low and therefore pulling the surface

upwards. The white-cap counteracts the movement of the rising sea surface, thus reducing the energy in the propagating wave. The application of this theory gives a source term on the form

$$S_{wc} = -\mu k E(\sigma, \theta), \tag{3.19}$$

where k is the wavenumber and μ is a coefficient that represents statistical properties of the waves.

In SWAN μ is approximated through statistical properties deduced from the energy spectrum $E(\sigma, \theta)$, the average spectrum steepness, and the average wave number. Coupling between these can be tuned through different parameters. Christakos, Björkqvist, Tuomi, Furevik and Breivik (2020) found that this approach, which is used in the KOMEN method (default in SWAN) performs best in terms of significant wave height computation in sheltered areas, i.e. almost no exposure to swell. On the other hand, it is not suitable to use in mixed swell-wind sea conditions, which is relevant for exposed areas such as Alpha and Beta. The main problem is that KOMEN depends on average steepness of the spectrum and wave number, which, in turn, is problematic in mixed conditions.

The WESTH method has showed more accurate results for mixed swell-wind sea states than the standard KOMEN method (Christakos, Björkqvist, Tuomi, Furevik and Breivik, 2020). Moreover, WESTH has also showed better accuracy than JANSSEN, the last of the three methods available in SWAN (Stefanakos et al., 2020). WESTH is based on empirical expressions of relationship between non-linear hydrodynamics within wave-groups. Contrary to KOMEN, WESTH does not include quantities distributed over the spectrum such as average spectrum steepness and wave number, but rather depend on the local quantities. It also shows some dependence on the magnitude of the wind forcing and wave growth (wave age), as the dissipation because of white-capping is more intense for strong wind-drag conditions. As mentioned earlier, the WESTH method also uses an alternative expression by Yan (1987) for the wind-generated source term that estimates strong wind drag conditions more accurately. The other source terms are unaltered. For more information on the WESTH method, see van der Westhuysen et al. (2007).

A sketch of the white-capping source term is given in figure 3.13.

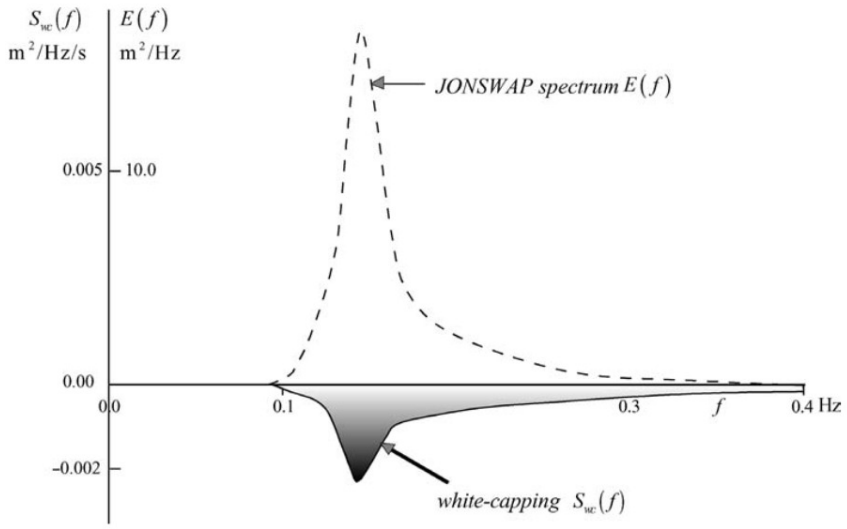

Figure 3.13: Plot of the white-capping dissipation source term for a given JONSWAP spectrum (Holthuijsen, 2007).

3.5.3.2 Surf-breaking

When waves propagates toward shore, shoaling leads to increasing wave height. Shoaling is discussed further in chapter 3.6. A consequence of shoaling is that the wave height will exceed a certain limit (see under) and then the waves will break, thus dissipating the energy rapidly. This breaking process differs from the white-capping as it is induced by reduction in depth, and therefore referred to as surf-breakers. For aquaculture sites in shallow waters, surf-breaking will be the dominating dissipation process and therefore important to model correctly.

As for white-capping, surf-breaking is also a poorly understood physical process. However, it is found that the total energy dissipation due to surf-breaking is well modelled with the analogy of a bore and the source term is

$$S_{surf} = \frac{1}{m_0} D_{surf} E(\sigma, \theta). \tag{3.20}$$

m_0 is the zeroth-order moment of the wave spectrum as according to the definition of n'th moment in (3.8), and the average dissipation ratio (per unit time and unit bottom area) is

$$D_{surf} = -\frac{1}{4} \alpha_{BJ} Q_b \frac{m_1}{m_0} H_{surf}^2,$$

where α_{BJ} is a tunable coefficient, m_1 is the first-order moment of energy spectrum, H_{surf} is the maximum wave height before the wave breaks. Q_b is the fraction of breakers which is dependent on the set H_{surf} and m_0. For more information on the analogy and derivation, see Battjes and Janssen (1978).

The SWAN team suggest to make changes in surf-breaking source term by tuning the maximum

wave height, which given as a function of the depth including the wave-induced setup

$$H_{surf} = \gamma_B d_{setup}, \tag{3.21}$$

where γ_B is the breaker index and is proposed to be between 0.6 and 0.83. d_{setup} is the increase in mean water level due to breaking waves and is approximated in SWAN, but will not be included in the computations in this thesis. See (*SWAN*, 2020, chapter 5) for further information.

Babanin et al. (2001) showed that γ_B will vary with the bottom slope. It will therefore be challenging and require a lot of testing to set a suitable value for specific cases. As a consequence, the standard value ($\gamma_B = 0.73$) will be used.

In very shallow waters, surf-breakers becomes more dominant than white-capping. At Alpha and Beta there are large depth variations in small geographical space. As a result, both surf-breakers and white-capping could be of importance, and should be included in analyses.

A sketch of the surf-breaking dissipation source term is given in figure 3.14. It follows a similar form as the white-capping source term.

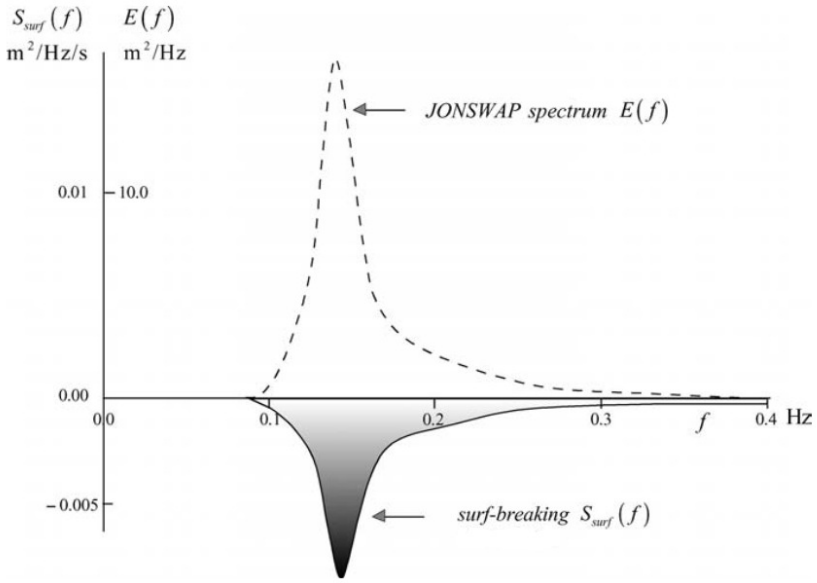

Figure 3.14: Plot of the surf-breaking dissipation source term for a given JONSWAP spectrum (Holthuijsen, 2007).

3.5.3.3 Bottom-friction

Bottom friction covers all the mechanisms in the turbulent layer close to the bottom. This layer is assumed to be very thin compared to the depth so that the conditions of linear wave theory holds. The conditions of linear wave theory are presented in Appendix A.

The energy is transferred from the water particles above the turbulent layer to the water particles in the turbulent layer. How much energy is transferred will vary with the characteristics of the

bottom and the wave field above. In addition, the wave field may also change the bottom characteristics by moving particles, but this effect is omitted in SWAN.

The source term is approximated as

$$S_{bfr} = -K_{bfr} \left[\frac{\sigma}{gsinh(kd)} \right]^2 E(\sigma, \theta), \tag{3.22}$$

where d is the water depth, k is the wave number, g is the gravitation constant. K_{bfr} is defined as the bottom friction coefficient and generally depends on the orbital motion of the water particles close to the bottom. There are four options for modelling the bottom friction in SWAN, which in practice will just be different expressions for the bottom friction coefficient K_{bfr}.

Bottom-friction is found to be the dominant mechanism for bottom dissipation on *sandy seabeds*. The bottom roughness is critical to estimate the bottom-friction correctly, and there will therefore be uncertainty on other seabeds with e.g. clay, which is the case at location Alpha. Less sand should reduce the amount of sediment transport, which would have challenged the assumption of stationarity (since SWAN, as mentioned, will be run in stationary mode).

There is no field data evidence that suggests a preferred friction model, because of the large variations in bottom conditions (*SWAN*, 2020, chapter 2.3). Hence, the default JONSWAP method (*SWAN: User manual*, 2016, p. 58) will be used for the simulations, which applies a constant value for the bottom friction coefficient ($K_{bfr} = 0.038\ m^2 s^{-3}$) for the whole computational domain.

The scale of the domains considered in aquaculture, such as for Alpha and Beta, are not large enough for the bottom-friction to have a significant impact on the results, and wave-breaking is expected to dominate dissipation. Another choice of method, or even turning off bottom-friction, should therefore not give notable change in results.

A sketch of the bottom friction source term is given in figure 3.15. It follows the same form as the white-capping and surf-breaking source terms.

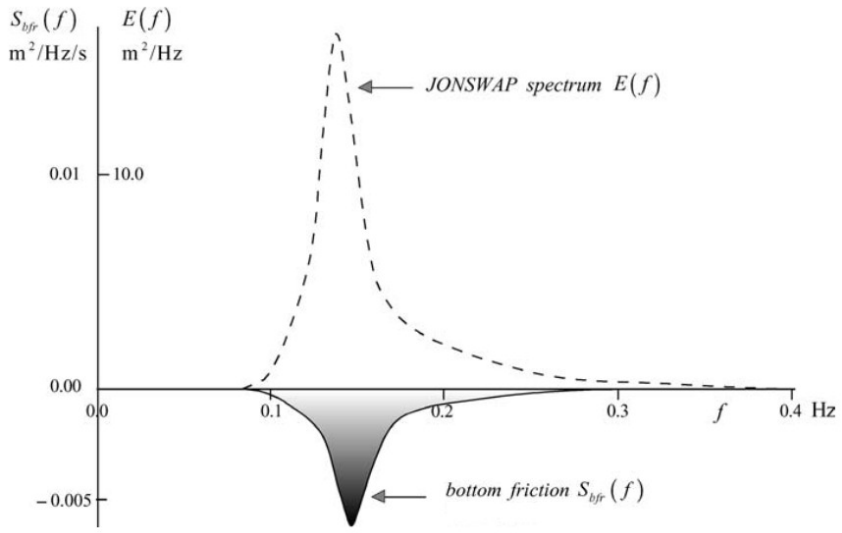

Figure 3.15: Plot of the bottom-friction dissipation source term for a given JONSWAP spectrum (Holthuijsen, 2007).

3.5.3.4 Vegetation, mud, sea ice, and turbulence

Four more dissipation source terms are implemented in SWAN. These are not mentioned by Holthuijsen (2007), and only sea ice and vegetation by *SWAN* (2020). Some numerical approximations have been developed recently, and these have only been a part of SWAN versions developed in the last 3-5 years. Note that there are four separate source terms, and these are calculated differently, even though they are presented together for simplicity in figure 3.5.

For surface gravity waves, the turbulence is usually irrelevant, which is the reason potential flow models such as REEF3D (2020) are developed. There is also little vegetation and no sea ice in the areas. There is some clay (mud) at location Alpha (Vaardal-Lunde et al., 2018), but not so much that it should cause dissipation that is notable compared to wave breaking. Source terms from vegetation, mud, sea ice and turbulence are therefore assumed negligible in this case, and will therefore not be activated. For more information, see *SWAN: User manual* (2016).

3.6 Wave transformation in coastal waters

Wave transformations cause change in direction, speed and frequency of a wave, and therefore also its energy, as it propagates in geographical space. This is accounted for in the governing equation (3.13) as changing ratios per time, c. The ratios are computed for every cell in the computational area and the grid resolution is therefore important for the accuracy of the wave transformations. Understanding the characteristics of each wave transformation, and what input data the ratios are affected by, is a prerequisite for analyzing SWAN results.

The different ratios and which type of transformation they are influenced by are presented in figure 3.16. c_θ is the turning ratio, c_σ is the frequency ratio, and c_x and c_y is the velocity in x- and y-direction, respectively.

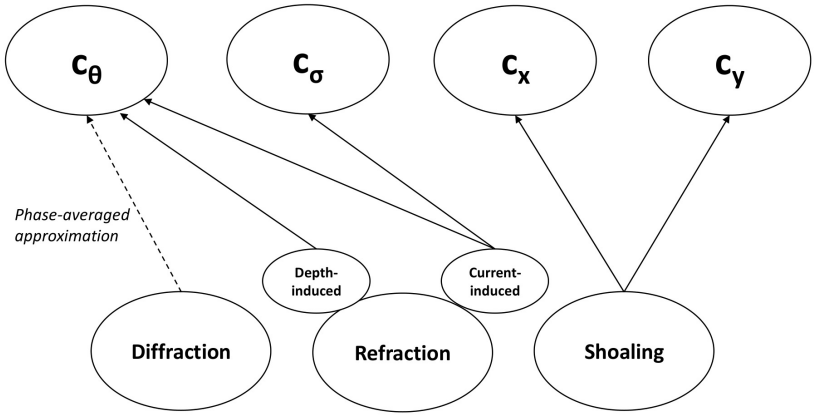

Figure 3.16: Wave transformations and resulting changing ratios, denoted by c.

In addition to the above mentioned transformations, reflection and transmission could also be of importance when there are obstacles such as steep cliffs, breakwaters etc. apparent. This must be given manually as input to SWAN with a set reflection coefficient. Reflection and transmission will not be included in simulations at location Alpha and Beta, however. For more information about reflection and transmission in SWAN, see Appendix B.

3.6.1 Shoaling

When waves propagate towards the beach orthogonal to depth contours and it is assumed a fixed seabed topography and gentle slopes, the wave frequency ω is constant. Since the dispersion relationship given by (3.2) is still valid, the wave number $k = 2\pi/\lambda$ must first increase, then decrease towards zero. As a result, the wave amplitude will first decrease, then increase towards infinity. This has consequences for the applicability of linear wave theory, as it assumes small

wave amplitudes as mentioned in chapter 3.1. It will be a problem at very shallow waters, where the waves become too steep for linear wave theory and the amount of wave breakers may form discontinuity. Use of SWAN at very shallow waters should therefore be avoided. This should not be a problem on intermediate depth however, since the waves break as the wave amplitude increases significantly. Moreover, refraction and diffraction will also cause a different wave evolution. Alpha and Beta are located in deep waters (more in chapter 4) and this is not considered a problem for the studies in this thesis.

The group speed with the shoaling effect c_g is described by (3.4) in the Eulerian approach. Note that c_g is gruop velocity in the wave direction, whereas it in the action balance is decomposed in x- and y-direction as c_x and c_y respectively. Over a flat sloping bottom, with no other effects of propagation, generation or dissipation, the group velocity will first increase slightly, then decrease towards zero.

3.6.2 Refraction

Depth-induced refraction

When the wave approaches the coast at an angle, it will (slowly) change its direction such that it is orthogonal to the depth contours. This follows from the previously defined velocity of the wave crest in (3.3). When the depth decreases, the phase velocity is reduced. Consequently, waves will always turn towards shallower water.

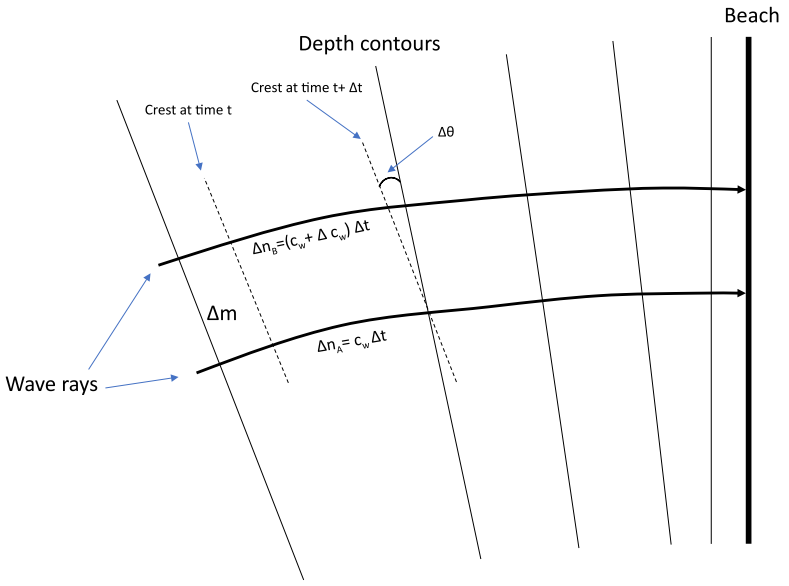

Figure 3.17: Sketch of depth-induced refraction, as described by (Holthuijsen, 2007, Appendix D).

As seen from figure 3.17 (which illustrates the descriptions of Holthuijsen (2007)) the turning

rate $\Delta\theta$ per unit forward distance in the waves direction Δn is

$$\frac{\Delta\theta}{\Delta n} = \frac{-(\Delta n_B - \Delta n_A)}{\Delta m \Delta n} = -\frac{\Delta c_w}{c_w \Delta m},$$

which for infinite small differences becomes

$$\left(\frac{d\theta}{dn}\right)_{dep} = -\frac{1}{c_w}\frac{\delta c}{\delta m} = \frac{1}{k}\frac{\partial k}{\partial m}, \tag{3.23}$$

where the last equal sign comes by assuming a constant frequency ω and then substituting for c_w.

However, as mentioned in the introduction of chapter 3, the wave model in SWAN use an Eulerian approach, and the refraction must be expressed as a turning ratio per time and not unit distance. The wave energy travels with velocity c_g as per (3.4), thus the energy travels a distance $\Delta n = c_g \Delta t$ with a turning rate $\Delta\theta = d\theta/dn \cdot \Delta n$. Substituting in (3.23) gives the turning rate per time $c_\theta = d\theta/dt$ in a frame of reference moving with the wave energy

$$c_{\theta,\,dep} = -\frac{c_g}{c_w}\frac{\delta c}{\delta m}. \tag{3.24}$$

Depth-induced refraction is an important wave propagation dynamic when modelling waves on the Norwegian coast. Contrary to Holland (where SWAN is created) the depth will not be evenly decreasing against the beach, but rather have fast variations between deep and shallow waters. For exposed sites, or sites in fjords open to incoming swell (unidirectional waves), the typical wave pattern may be chaotic as seen from figure 3.18. It is therefore important that the bathymetry data and corresponding computational grid has a high enough resolution to solve the chaotic wave patterns sufficiently. There is no obligation to provide documentation that the resolution is sufficient in NS9415 (2009), however, and this could be an aspect that cause variations between industry actors' analyses with SWAN.

As was seen in chapter 2, location Alpha is highly exposed to swell in all western directions, whereas Beta is exposed to swell from north-west. However, because of refraction, the wave direction on-site may differ from the offshore waves since large depth variations can lead to chaotic wave patterns as the offshore waves propagates towards the shore.

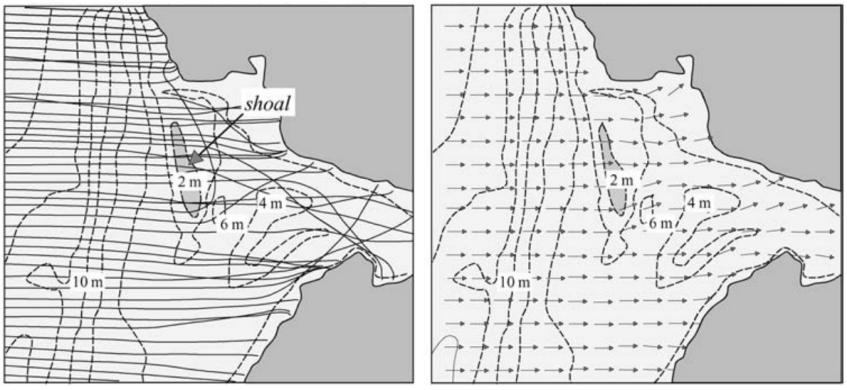

Figure 3.18: Depth-induced refraction on a largely varying bathymetry when input is JONSWAP spectrum which is unidirectional (left) and two-dimensional (right) (Holthuijsen, 2007).

Current-induced refraction

The amplitude, frequency and direction of the waves may also change when they propagate with ambient current, i.e. tidal-, ocean-, local wind generated-, river- and/or wave generated current. If the harmonic wave propagates in an area with ambient current the linear wave theory is still valid since the frame of reference can be moved with the current. The wave then has a frequency σ, relative to the new frame of reference. The dispersion relation given from (3.2) is still valid for the new frame of reference

$$\sigma^2 = kg \tanh(kd) \tag{3.25}$$

The relation between relative and absolute frequency, i.e. the frequency relative to the bottom, is

$$\omega = \sigma + kV_n, \tag{3.26}$$

where V_n denotes component of the current velocity V in the wave direction.

It can be derived (see Holthuijsen, Appendix D) that the rate of change of relative frequency in a frame of reference moving with the wave energy along the wave ray is

$$c_\sigma = \frac{\partial \sigma}{\partial d}\left(\frac{\partial d}{\partial t} + V\frac{\partial d}{\partial s}\right) - c_g k \frac{\partial V_n}{\partial n}. \tag{3.27}$$

The terms in the brackets are related to respectively depth variation over time, and the effect the current moving the wave across a horizontally varying *bottom*. The last term is effect of the wave with group velocity c_g and wavenumber k moving over horizontally varying *current*. s is the direction of wave energy transport with the current (i.e. along the streamline), and n is the wave direction relative to the current.

If the ambient current is not uniform it will move the water particles towards its streamline, leading to a turn of the wave crest. The wave direction will be changed in the same manner as

for varying water depth, ref figure 3.17, and the total ratio of direction change is therefore

$$c_{\theta,ref} = \underbrace{-\frac{c_g}{c_w}\frac{\partial c_w}{\partial m}}_{c_{\theta,dep}} \underbrace{-\frac{\partial V_n}{\partial m}}_{c_{\theta,cur}}. \tag{3.28}$$

It might be a challenge to obtain measurements of the current over a sufficient amount of time: There are few measuring buoys on the Norwegian coast, and most of them are installed in the last few years (Norwegian Meteorological Institute, 2021). Vaardal-Lunde et al. (2018), Borge and Nilsen (2021), and Hestnes and Torkildson (2021) have not included current in the computations for location Alpha and Beta, and it will not be a part of the computations for the cases in this thesis. That is, $\sigma = \omega$. However, aquaculture sites are often placed in areas with high current velocities for the replacement of water in the cages, and it is therefore a potentially significant inaccuracy to neglect it.

3.6.3 Diffraction

When a harmonic long-crested wave propagates over a constant depth around a headland or breakwater, the waves will travel into the shadow zone of the obstacle (diffract). The reason is a large variation of wave energy - and therefore transfer of energy - *along* the wave crest in addition to along the wave rays. This is illustrated in ParaView (2021) for regular waves with height and period of 4 meters and 6 seconds, propagating against a breakwater in figure 3.19. How much energy travels into the shadow zone depends on the incoming wave: The shorter the wavelength (higher frequency), the more it will be diffracted.

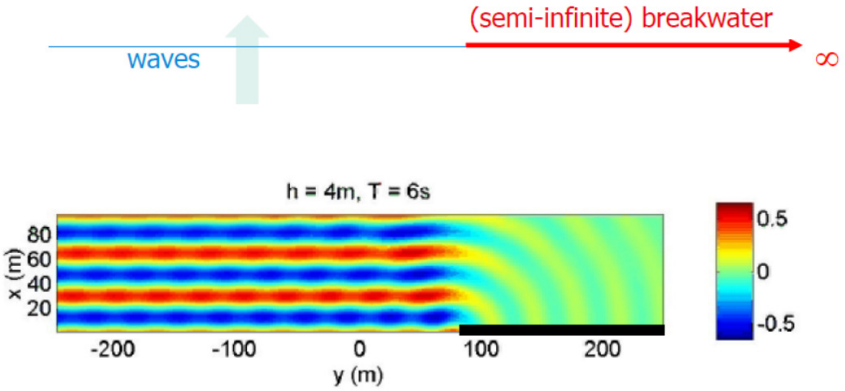

Figure 3.19: Diffraction around a breakwater illustrated with ParaView (2021) from REEF3D simulations.

Contrary to what was considered for refraction and shoaling, the wave amplitude and the phase shift varies rapidly in both horizontal space and time after the obstacle. That is, the surface elevation, earlier given by (3.1), is now

$$\zeta(x,y,t) = \zeta_A(x,y,t)\sin(\omega t - kx + \alpha(x,y)). \tag{3.29}$$

The spatial derivative of the amplitude must therefore be accounted for when the conditions of linear wave theory are derived. The challenge is then that diffraction is phase-dependent whereas SWAN uses the spectrum and thus does not resolve the phase, as discussed in the introduction of chapter 3. In Appendix A.1 the obtained results are presented. Note that the results are for a horizontal bottom.

The diffraction in SWAN is calculated by an approximation based on numerical experiments where the depth-induced refraction is included, i.e. a non-horizontal bottom. When combining the effects of varying amplitude with varying water depth given by (3.23), the result is

$$\left(\frac{d\theta}{dn}\right)_{dep+dif} = \frac{1}{k}\frac{\partial k}{\partial m} + \frac{1}{2(1+\delta_A)}\frac{\partial \delta_A}{\partial m}, \tag{3.30}$$

where the diffraction parameter is given as

$$\delta_A = \frac{\nabla c_w c_g \nabla \zeta_A}{k^2 c_w c_g \zeta_A} \qquad \text{with} \quad \nabla c_w c_g \nabla \zeta_A = \frac{\partial}{\partial x}\left(c_w c_g \frac{\partial \zeta_A}{\partial x}\right) + \frac{\partial}{\partial y}\left(c_w c_g \frac{\partial \zeta_A}{\partial y}\right). \tag{3.31}$$

Note that c_w, c_g are the velocities disregarding diffraction and varying depth. The velocities with varying amplitude and depth are obtained with the same analogy as before (see (3.3) and (3.4)) and are given as

$$C_w = c_w \left(1+\delta_A\right)^{-\frac{1}{2}}, \tag{3.32}$$

$$C_g = c_g \left(1+\delta_A\right)^{\frac{1}{2}}. \tag{3.33}$$

The total turning rate per time is

$$c_{\theta,dep} + c_{\theta,dif} = C_g\left(\frac{1}{k}\frac{\partial k}{\partial m} + \frac{1}{2(1+\delta_A)}\frac{\partial \delta_A}{\partial m}\right), \tag{3.34}$$

where the turning rate for diffraction is

$$c_{\theta,dif} = \frac{C_g}{2(1+\delta_A)}\frac{\partial \delta_A}{\partial m}, \tag{3.35}$$

which would be natural to use in the action balance equation. However, there is a problem in the solving of this equation; it requires previously discussed varying wave amplitudes, which in turn requires the turning rate. An alternative approach must be used.

The energy of a wave is proportional to the square of the amplitude (see (3.6)). Numerical experiments with ζ_A substituted with the square root of the energy density spectre $\sqrt{E(\omega)}$ for the diffraction parameter described by (3.31) has been carried out, and results obtained are the basis of the analysis in SWAN.

By substituting the amplitudes with the energy spectrum the wave phases are ignored, which is an important aspect to be aware of when computing waves with SWAN. Diffraction may turn waves in different directions in different areas, and in areas where such waves meet, this would give cross sea. Because the wave now consists of a sum of harmonic waves in different directions, information about the phase between waves are required. There are multiple areas where this can be a challenge, e.g. in the occurrence of reflecting obstacles like breakwaters or steep cliffs, and a high enough resolution is critical for the accuracy of the diffraction approximation.

Nevertheless, SWAN is not be suitable in some cases, and phase-resolved models such as REEF3D (2020) are necessary. An example is at a planned aquaculture site at Flatøya. As seen from figure 3.20 a complicated diffraction pattern is formed because of the archipelago. Wang (2020) compared the wave heights computed with SWAN and a phase-resolving model (REEF3D) at the wave buoys (red dots). Even for a resolution so high that the result converge (i.e. higher resolution does not affect results) SWAN still underestimated wave heights with 20-50% compared to the phase-resolved model.

An evaluation of diffraction and its importance to the results of a site is therefore necessary. In figure 2.1 and figure 2.2 the skerries in proximity of location Alpha and Beta were highlighted, and these could be a source of error to the SWAN results at the two locations.

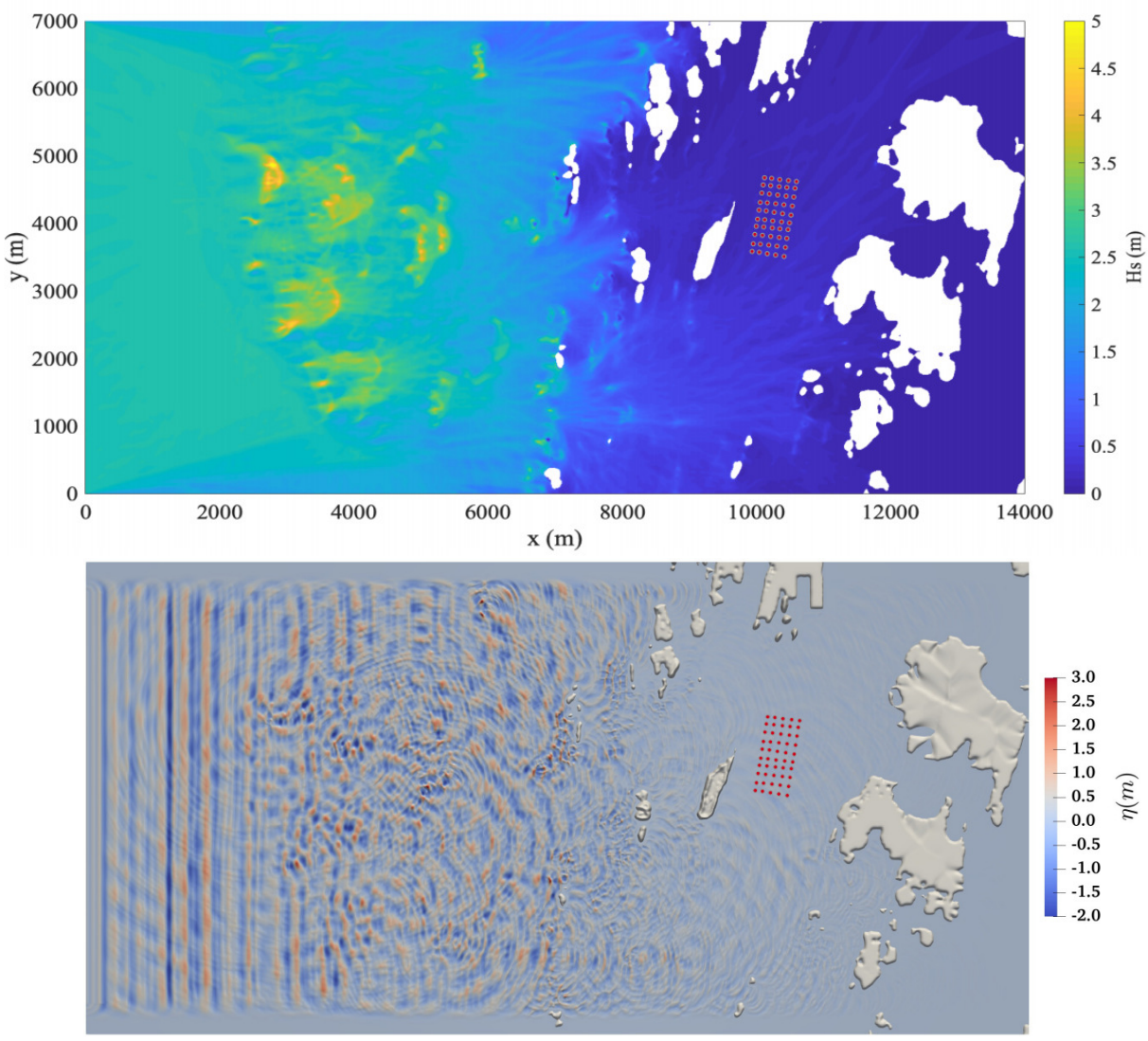

Figure 3.20: Significant wave height at Flatøya computed with SWAN and surface elevation computed with the phase-resolving model REEF3D (Wang, 2020)

Chapter 4

Sensitivity study

The impact from three different parameters are chosen for a sensitivity study. In chapter 3, it was established how many choices of SWAN input is left to the industry actor, as they are not covered by the industrial standard NS9415 (2009). This lead to an assumption that parameters and choices of input are varying between actors. The parameters chosen for the sensitivity study are based on this assumption, so that the sensitivity of SWAN in its practical use in the industry can be investigated.

The three parameters chosen are grid resolution, size of computational domain, and wind fetch, and will be treated in three separated studies. The goal of each study is specified more in-detail such their influence can be investigated, which is part of secondary objective 3 of this thesis. The three studies are summarized as follows:

- Resolution of the computational grid:
  The governing equation is solved for each cell in the computational grid. The grid must have a high enough resolution such that all spatial details of wind, current, and bathymetry are properly resolved. To ensure that the resolution is satisfying, it should be checked that an increase in resolution does not affect the result, i.e. that the results *converge*. There are no obligations regarding resolution from NS9415 (2009), and it is up to each industry actor to ensure satisfying resolution. **The resolution study shall investigate the importance of resolution, and should ensure that a satisfying resolution is used for the two other studies.**

- Size of the computational domain:
  The position of the boundary condition (incoming offshore waves) is decided by how large the domain is. The boundary condition is known at a datapoint with a said coordinate, and it is therefore important the boundary of the computational domain is in-line with this datapoint. This is not standardized in the industry, however, even though this is expected to have impact on results. The hypothesis is therefore that some actors may use a too

small computational domain, such that there is a mismatch between the datapoint with known data and the set boundary condition, and the situation illustrated by figure 3.4 is attained. **The grid domain study shall investigate the influence of having a mismatch between boundary conditions and the datapoint by varying the size of the computational domain.**

- Implementation of local wind:
  The literature study showed the importance of wind forcing in wave modelling in Norwegian coastal areas. Implementation of wind in the SWAN model is therefore expected to be of great significance to on-site wave exposure, especially at location Beta which is more sheltered from swell than location Alpha. A common approach for the industry is to set wind with a standardized speed and direction in the whole computational grid, and then use a paramterization of hindcast data from a generation scale model on the boundary. The potential problem with this is that if the hindcast data also contains wind sea, wind energy will be added twice close to the boundary. An alternative is to set the wind in a limited area of the grid, which, in turn, reduces fetch. **The wind study therefore investigate the importance of fetch when implementing wind in the SWAN model.**

The parameters will be investigated through simulations on location Alpha and Beta (see chapter 2). Bathymetry, wind, and boundary conditions for the two locations must therefore be acquired (current will not be implemented in the model). In addition, there are different source terms in the SWAN model, and it must be chosen which of these will be activated in simulations. Furthermore, approximation methods for activated source terms must be chosen. This constitutes the numerical setup for the two locations, and is presented in chapter 4.1.

4.1 Numerical setup for Alpha and Beta

Choices of mode (stationary/non-stationary) and calculation methods of SWAN must be chosen for the numerical setup of the SWAN model for the two locations. Moreover, input data must be provided to solve the source terms and wave transformation described in chapter 3. In this study, the data given as input will be the bathymetry, incoming offshore waves (boundary conditions), and a wind field. In addition, choice of method for approximating the source terms must be given.

All simulations will be run in stationary mode in version number 41.31 of SWAN. The use of a stationary run requires a stationary sea state, which will give some implications to the implementation of a wind field in the simulation model. More in chapter 4.1.5.

A spherical convention is used for the coordinates, which implies that x- and y-coordinates are given in degrees for longitude and latitude respectively. A central conformal Mercator projection is used (*SWAN: User manual*, 2016, page 28). The x- and y-coordinates are normalized in all

figures, which means that $(x, y) = (0, 0)$ is the origin of each area instead of the usual convention where $x = 0$ is at the Greenwich meridian, and $y = 0$ is at the equator. Moreover, the unit of the coordinate system is converted to kilometers, by using a constant scaling factor for each location. The scaling factors (in kilometer per degree) are 111.5 in x-direction and 41.8 in y-direction for location Alpha, and 111.5 in x-direction and 40.0 in y-direction for location Beta. Note that the used scaling factors are only valid in the origin of each location, but the error is negligible for the small computational domains used here.

For the directions of wind and waves, a nautical convention is used where 0 degrees is North, as given by figure 4.1. All direction angles are for the direction the wind/wave goes *towards*.

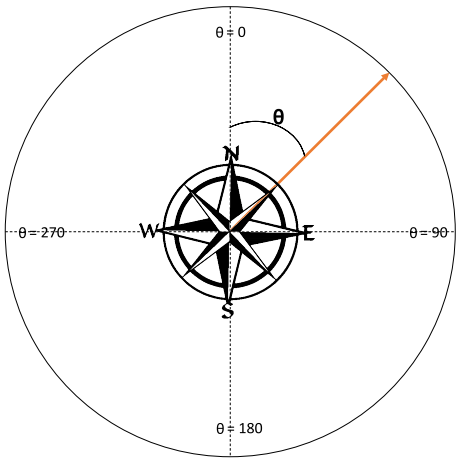

Figure 4.1: Direction convention.

The model will resemble the ones used by industry actors to assess wave exposure at aquaculture sites. Model setup from industry actors are provided by Vaardal-Lunde et al. (2018) for location Alpha, and Borge and Nilsen (2021) and Hestnes and Torkildson (2021) for location Beta. Even though this study will focus only on certain parameters for a sensitivity study, it is important that the rest of the numerical setup is customized for this area with regards to NS9415 (2009), and resembles models used by the industry. As a result, the sensitivity of the industry models can be analyzed with the numerical setup used in this study. Note that the results will not be directly compared with the industry models since they are a part of internal reports.

The bathymetry of the two locations chosen for this case study is showed in figure 4.2 and figure 4.3. The method for processing bathymetry data will be discussed in chapter 4.1.2. The location of WAM datapoints, which are used to set the boundary conditions, will be discussed further in chapter 4.1.4. The aquaculture site is placed at approximately 130 m depth at location Alpha. Location Beta is placed on a continental shelf, and the depth varies between 130 and 230 m. Close to the shore, there are also regions of deep water in both areas. The mix of deep water and shallow water will potentially cause chaotic wave patterns due to depth-induced refraction. The skerries north-west of the aquaculture site at location Beta might cause some diffraction

and cross sea and thus a potential source of error. However, they are scarcely located, thus the diffraction is not expected to have a large impact on the wave-field such as experienced at Flatøya by Wang (2020) (see figure 3.20). There are also some small skerries North-West of the aquaculture site at location Alpha. However, as will be presented in table 4.2, the incoming offshore waves comes from the west, and the diffracted waves should therefore propagate straight into the land in the shadow zone (east of the skerries). Diffraction should therefore not be a dominant part of the wave-field in location Alpha either. Consequently, phase-resolved models should not be required for the two areas, and SWAN is expected to be suitable for an analysis of wave exposure for the two aquaculture sites.

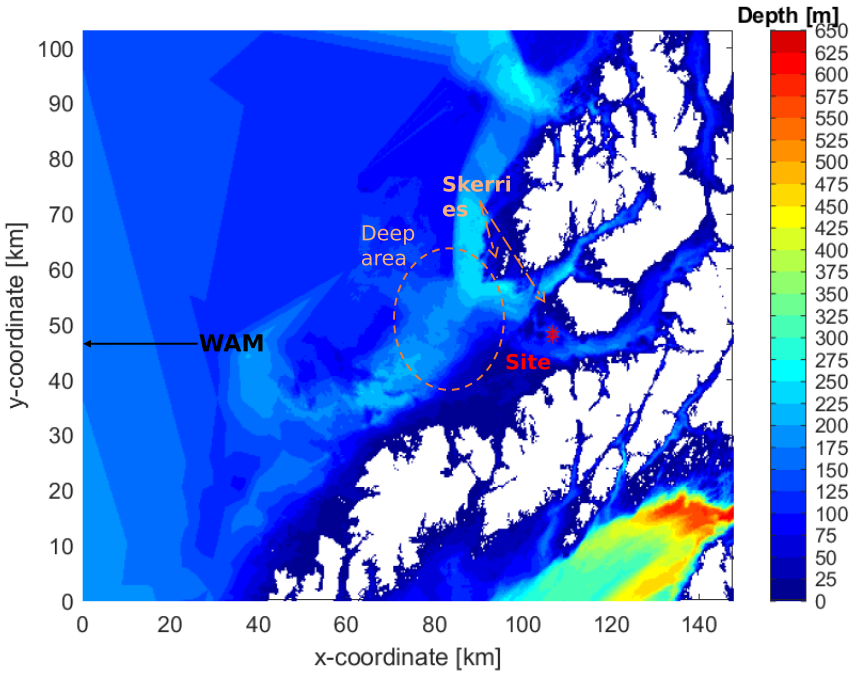

Figure 4.2: Bathymetry of location Alpha.

Complex areas with regards to shoreline and bathymetry such as Alpha and Beta, require higher resolution than e.g. at a typical beach shore. The wave transformations will cause chaotic and complex wave fields, which, in turn, require more equations in geographical space to solve. That is, we need more grid cells (meshes), such as illustrated in figure 3.1, and increase in resolution should therefore influence results.

Both locations have large open areas, which will increase the importance of incoming waves from offshore areas (swell). The boundary conditions are therefore expected to be an important influence on the wave exposure at the location. The computational domain study should be suitable to run at the two locations.

Local wind is not necessarily as important in exposed areas as it is in more sheltered areas, as swell may be the dominant cause of wave exposure. On the other hand, open areas also imply

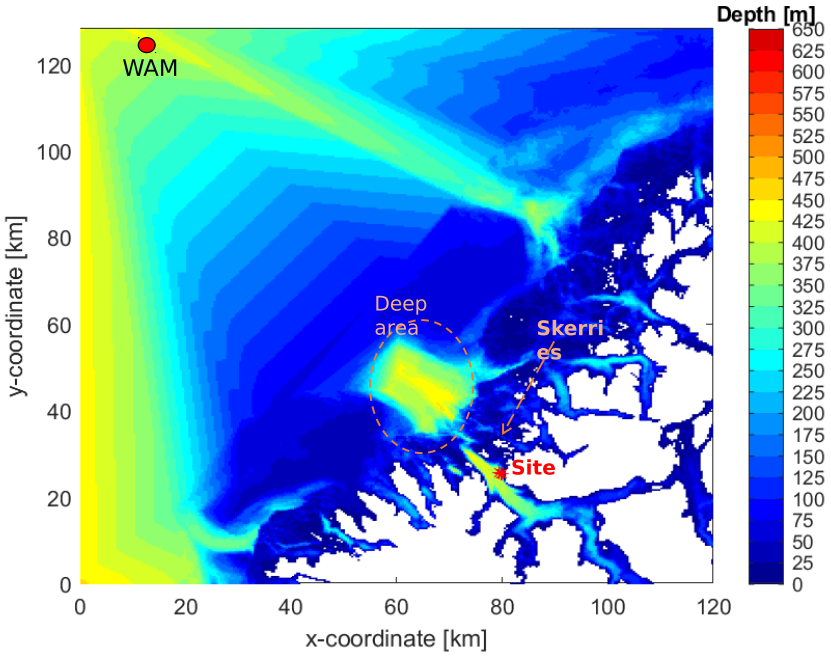

Figure 4.3: Bathymetry of location Beta.

longer fetch, resulting in a high wind speed, and wind is therefore important for of the wave environment. The two locations should therefore be suitable for the wind study.

NS9415 (2009) requires waves with both a 10 year and 50 year return period. In this thesis it is chosen to analyze waves with a 50 year return period only.

4.1.1 Nesting of computational grid

The analysis will be performed with nested grids. Nesting is a function in SWAN where the input from a coarse computation grid is used as input to the subsequent nested grid. That is, a set of output locations along the boundary of the subsequent nested grid is defined and the resulting energy spectra at these output location are used as boundary condition.

With nested grids, the SWAN model is run with a coarse computational grid at large-scale areas with deep water that does not require a high resolution. In nearshore areas however, the complexity of the bathymetry and topography increase, which, in turn, requires a higher resolution to solve properly, and small-scale nested grids with higher resolution are used. Compared to having the same resolution in the full area grid (i.e. whole computational domain), nested grids may reduce the simulation time without affecting the accuracy of the result.

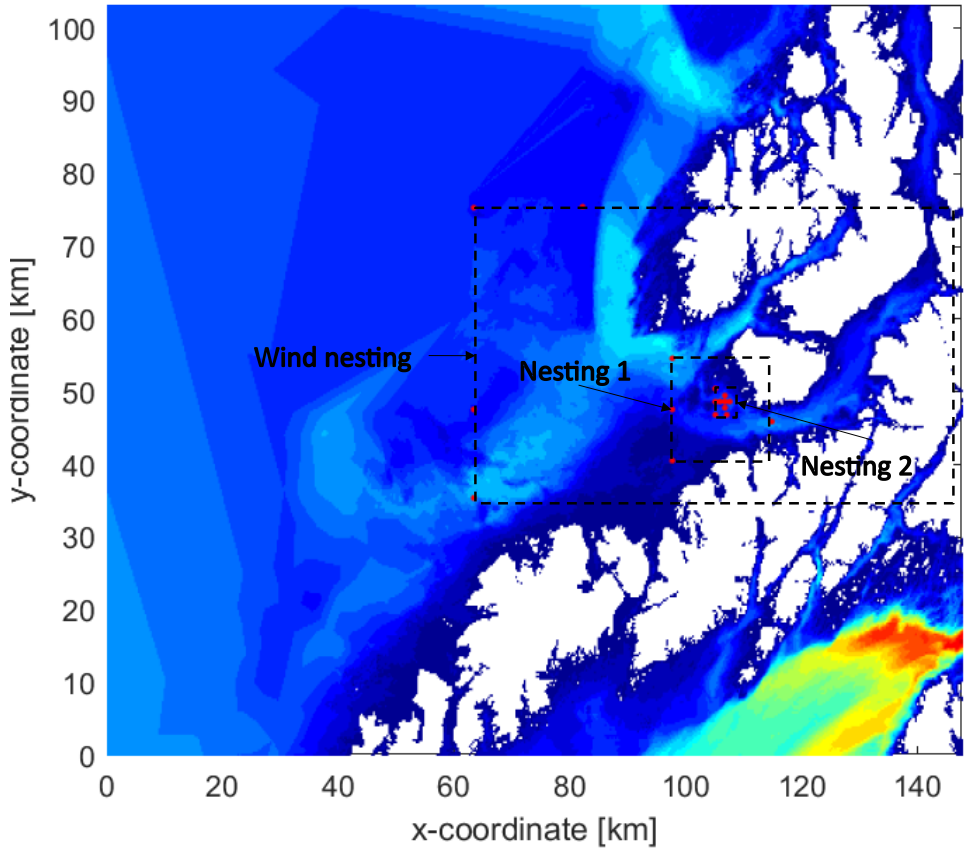

Figure 4.4: Nesting grids of location Alpha.

Location Alpha is nested with 3 grids. The first is the wind nesting grid, which has its boundary approximately 30 km from the site. It is included to implement wind in a limited area of the grid, but it has approximately the same resolution as the full area grid, and will therefore not give increased accuracy. In addition, two more nesting steps with increasing resolution are included closer to the fish farm. All nested grids in location Alpha are given in figure 4.4.

Location Beta is nested with 2 grids. The first nesting grid gives a fetch length of approximately 25 km, comparable to the wind nesting grid of location Alpha. It also has a higher resolution compared to the full grid. The last nesting increases the resolution even further. The nested grids of location Beta are given in figure 4.5.

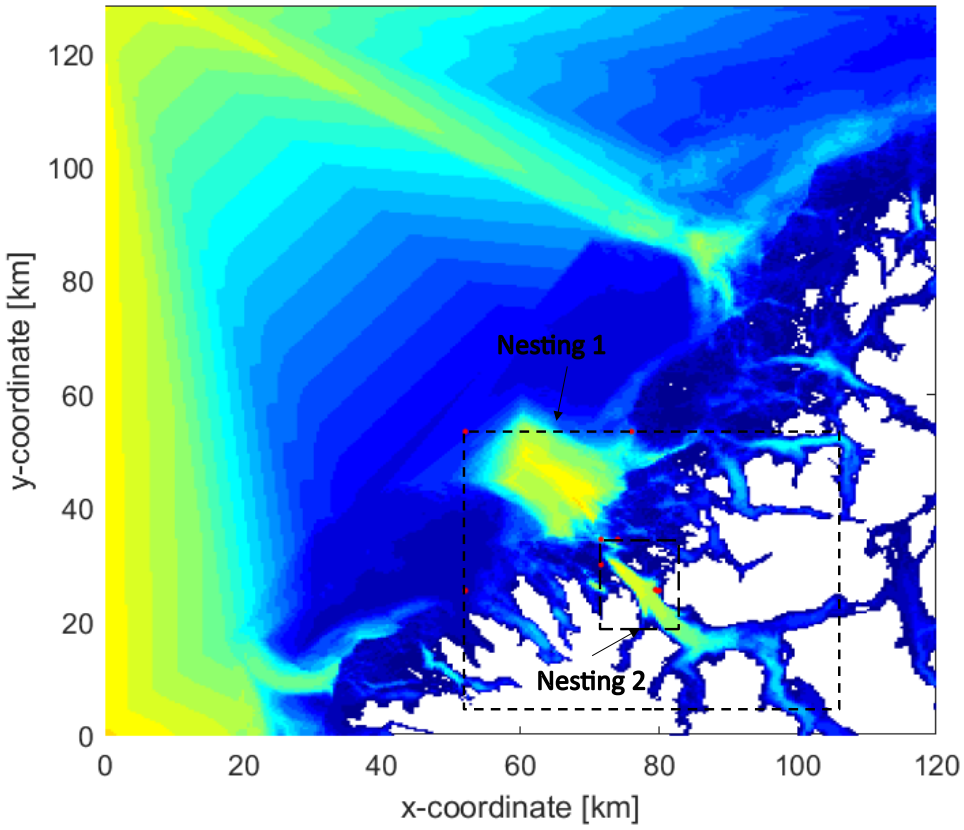

Figure 4.5: Nesting grids of location Beta.

A set of individual measuring points are defined at both locations. In these measuring points, resulting properties from the SWAN model can be computed. The points are set just outside the boundary of each nesting grid to control the input to each nesting. Some additional points are distributed in proximity of the fish farm location, inside the innermost nested grid. At location Alpha, 17 points are placed (figure 4.6): four outside the wind nesting grid, four outside nesting 1, four outside nesting 2, and five inside nesting 2. At location Beta 9 points are placed (figure 4.7): three outside nesting 1, three outside nesting 2, and three inside nesting 2. The exact coordinates of the measuring points are given in Appendix C.

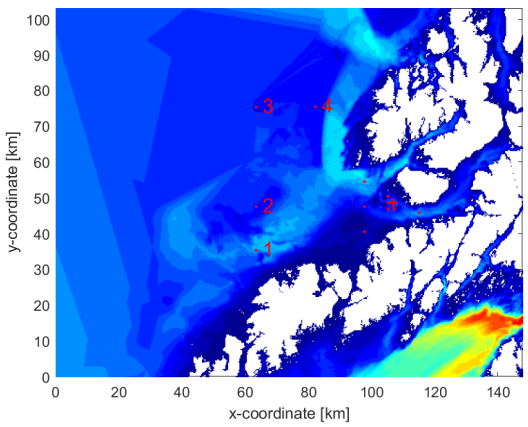

(a) Full area.

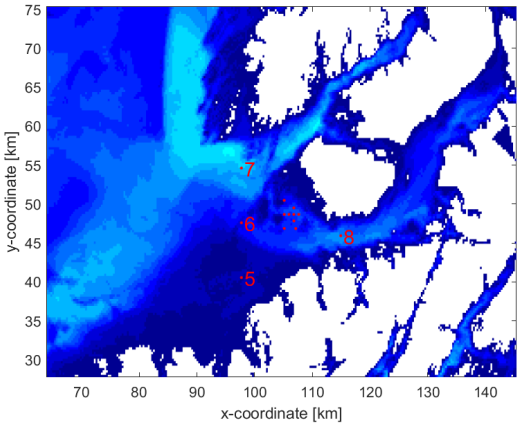

(b) Wind nesting.

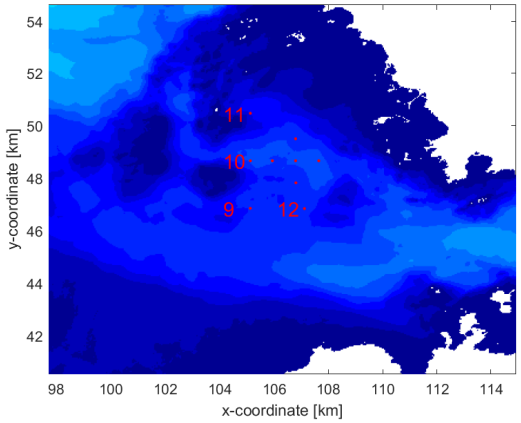

(c) Nesting number 1.

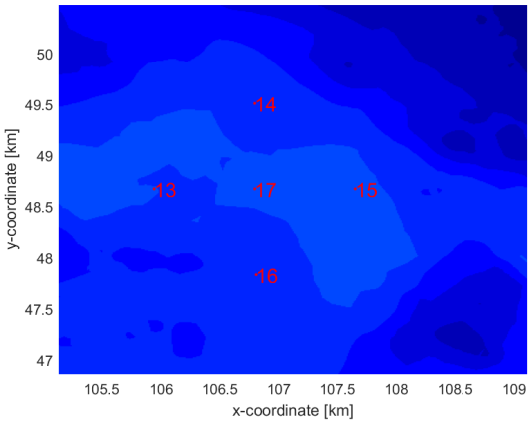

(d) Nesting number 2.

Figure 4.6: Nesting grids and measuring points of location Alpha.

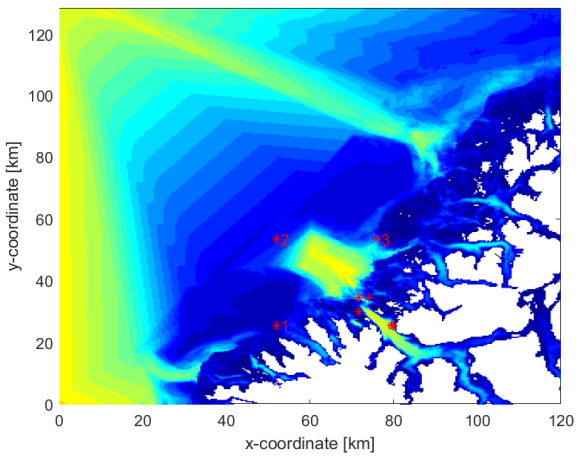

(a) Full area.

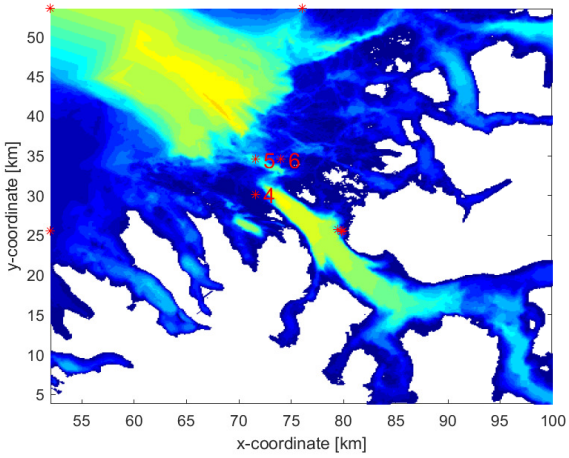

(b) Nesting number 1.

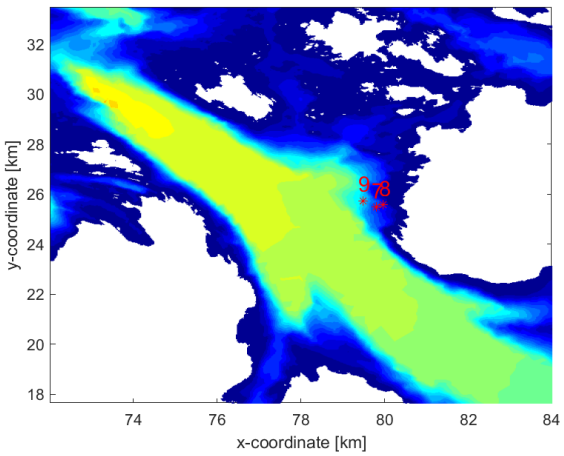

(c) Nesting number 2.

Figure 4.7: Nesting grids and measuring points of location Beta.

4.1.2 Bathymetry

The bathymetry for both locations are from Kartverket (2021), and are provided by Juliane Borge at Multiconsult, with different resolution for the different nested grids. The bathymetry resolution is presented in figure 4.8. For more detailed metadata on the bathymetry, see Appendix D. Plot of bathymetry maps are given in chapter 4.1.1.

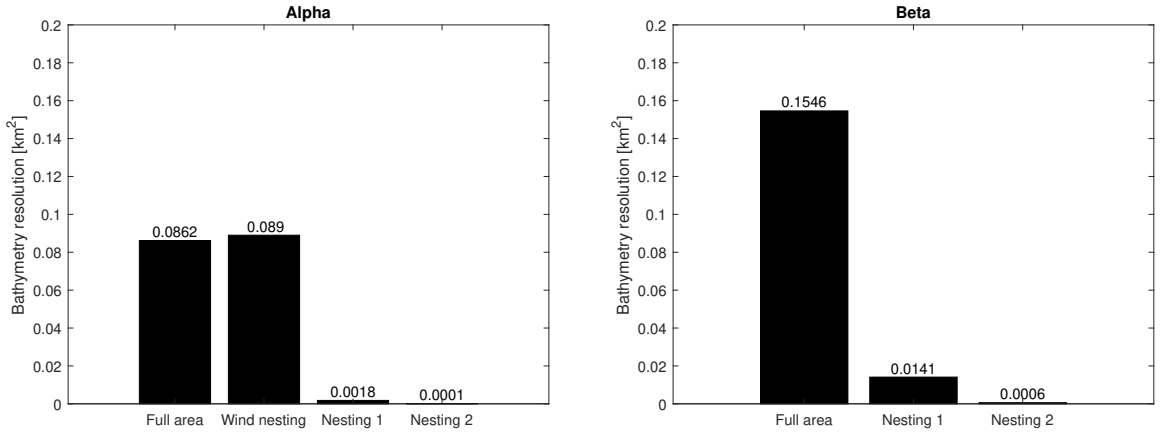

(a) Location Alpha.

(b) Location Beta.

Figure 4.8: Resolution of the bathymetry data for the nesting grids at location Alpha and Beta.

An alternative approach for processing the bathymetry, via the REEF3D (2020) mesh generation software DIVEMesh, is given in Appendix D. With this approach, data from Kartverket (Kartverket, 2021) are downloaded in a SOSI format, and is thereby processed to correct size and format with the Matlab scripts given in Appendix D. The resulting format is used as input in DIVEMesh, which, in turn, converts it to a bathymetry file that can be used in SWAN. The input commands in DIVEMesh used to process the data is also provided in Appendix D, where the commands are described by *DIVEMesh user guide* (2020). Processing the bathymetry with different mesh and grid size is a time consuming procedure however, and for practical reasons the bathymetry given by Multiconsult is used for all simulations.

SWAN can not run with a lower resolution on the computational grid than the input bathymetry, and bathymetry resolution presented in figure 4.8 will therefore be the lowest resolution used in the simulations.

4.1.3 Source terms

In chapter 3.5, the different source terms in SWAN, and choices for each of them related to the case studies were discussed. The choices are given in table 4.1. Default in the table is the option SWAN makes use of when the method is not specified. Christakos, Björkqvist, Tuomi, Furevik and Breivik (2020) found that white-capping is approximated more accurate with the WESTH method of SWAN in mixed swell/wind sea states, which is the case for location Alpha and Beta. It is therefore preferred to the default KOMEN method. The WESTH method makes use of an expression proposed by Yan (1987) for the wave generation by wind source term, and the method can not be applied without wind. Quadruplets are turned off when there are only waves from offshore areas (boundary condition) included, i.e. no wind, as the implemented calculation method for the quadruplet source term in SWAN (DIA) is limited for unidirectional waves.

Table 4.1: An overview over which source terms are activated, and which approximation methods are chosen to model them given for the simulations with only incoming offshore waves and for simulations with both offshore waves and local wind. Default is the option SWAN makes use of when the method is not specified.

Source term	Symbol	Without local wind	With local wind
Wave generation by wind	S_{in}	Deactivated	Yan
Quadruplet wave-wave interaction	S_{nl4}	Deactivated	Default (DIA[1])
Triad wave-wave interactions	S_{nl3}	Default (LTA[2])	Default (LTA)
White-capping	S_{wc}	Default (KOMEN)	WESTH
Surf-breaking	S_{surf}	Default (Bore analogy[3])	Default
Bottom friction	S_{bfr}	Default (JONSWAP[4])	Default
Vegetation	S_{veg}	Deactivated	Deactivated
Mud	S_{mud}	Deactivated	Deactivated
Sea ice	S_{ice}	Deactivated	Deactivated
Turbulence	S_{turb}	Deactivated	Deactivated

4.1.4 Boundary condition

The boundary condition comes from an extreme value analysis of hindcast data from model WAM10 and WAM75 for location Alpha and Beta respectively. The hindcast datapoints are approximately 30 kilometers west of the mid-west border of the Alpha computational gird, and for Beta it is placed on the north-west border of the grid. See figure 4.2 and figure 4.3. For more information about the WAM models, see Reistad et al. (2011). A joint distribution of significant wave height, H_s, and peak period, T_p, is modelled with the Conditional Modelling Approach (CMA) described by Mathisen and Bitner-Gregersen (1990) and DNV-RP-C205 (2017), assum-

[1]Discrete-interaction approximation, see chapter 3.5.2.

[2]Lumped-triad approximation, see chapter 3.5.2.

[3]See chapter 3.5.3.2.

[4]Constant bottom friction coefficient, see chapter 3.5.3.3.

ing H_s follows a Weibull distribution, and T_p follows a conditional log-normal distribution. Further, a contour of significant wave height and peak period is obtained with the constant probability density approach of CMA.

It is assumed that the spectra at the WAM datapoints are swell only. However. the parameterization of H_s and T_p is based on a combined sea state, as there are also winds blowing in proximity of the datapoint. The assumption is therefore a simplification.

For the sensitivity study it is decided to only look at directions that are anticipated to result in the largest swell on-site. More directions should be simulated for a full assessment of wave exposure at the two sites, however. The largest swell waves on-site is expected to come from open areas, namely from West and North-West for Alpha and Beta, respectively, and will be used for all simulations in this thesis. The corresponding H_s and T_p for a 50 year return period for these directions are obtained from Vaardal-Lunde et al. (2018) and Borge and Nilsen (2021), with the method described above and are presented in table 4.2. The boundary conditions will be set at a full boundaries of the computational grids. The boundary sides are chosen with respect to the position of the WAM models in figure 4.2 and figure 4.3.

Table 4.2: Significant wave height, H_s, peak wave period, T_p, and peak wave direction, θ_{peak}, for the boundary conditions of offshore waves with 50 year return period at location Alpha and Beta.

Location	Boundary side	H_s	T_p	θ_{peak}
Alpha	West	14.6	17.3	90°
Beta	North and West	11.9	16.9	130°

A JONSWAP spectrum will be set at the boundary, as it is found to be a good fit for wind-generated sea both from hurricanes and storms in deep water (Holthuijsen, 2007, chapter 6.3). Waves are typically more narrow in frequency, i.e. higher peak enhancement factor γ, and have a larger directional spreading coefficient, dd, with increasing peak period, according to Smith et al. (2001). dd and γ are explained in chapter 3.3. They propose a peak enhancement factor and directional spreading coefficient as given in table 4.3, which will be used in this study. According to NS9415 (2009), swell shall be set with $\gamma = 6.0$ for on-site measurements, but is does not propose any values for a wave modeling analysis, and the used γ and dd should therefore be within regulation.

Table 4.3: Peak enhancement factor, γ, and directional spreading coefficient, dd, for the JONSWAP spectrum (Smith et al., 2001), which is used for the boundary conditions at Alpha and Beta.

T_p [s]	≤ 10	11	12	13	14	15	16	17	18	19	20
γ [-]	3.3	4	4	5	5	6	6	7	7	8	8
dd [-]	4	8	10	12	16	18	20	22	26	28	30

The spectra used as boundary conditions for Alpha and Beta is presented in figure 4.9, with H_s and T_p from table 4.2, and dd and γ from table 4.3.

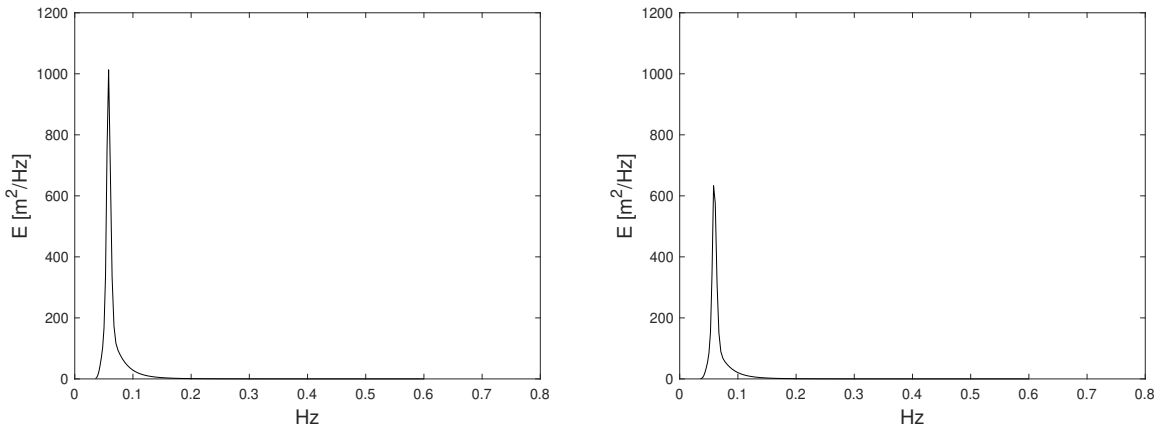

(a) Alpha. (b) Beta.

Figure 4.9: The spectra used as boundary condition in the simulations at location Alpha and Beta.

4.1.5 Local wind

A local wind set in the computational grid is what generates waves in the area, and adds energy to the incoming waves from offshore areas (boundary condition). The extreme speed and direction with a return period of 50 years is calculated from reference values of the Norwegian wind standard NS-EN 1991-1-4:2005+NA:2009 (2009), as the wind measurements in the two areas only cover limited time spans of under 20 years. Use of the wind standard is within requirements from NS9415 (2009). The wind standard gives a 10-minute average wind velocity (speed and direction), 10 meters over the water surface. SWAN is run in stationary mode, and the wind velocity is therefore modified to the mean wind velocity until the sea state become stationary, hereafter called fetch wind. This is done by calculating the shortest time period until the sea state becomes stationary from Leenknecht et al. (1992). Further, the fetch wind in this period is calculated according to NORSOK N-003:2017 (2017), a standard for the Norwegian petroleum industry. For wind directions with shorter fetch, the mean wind velocity will be averaged over a shorter time period than for directions with a longer fetch.

The fetch wind with a 50 year return period at location Alpha is provided by Vaardal-Lunde et al. (2018). The results for the two directions that will be used in simulations are given in table 4.4. A wind direction of $\theta_{wind} = 90°$ comes directly from west, and is considered an open fetch, as there are no obstacles/land between site and the boundary of the grid, see figure 4.2. $\theta_{wind} = 150°$ is also considered an open fetch, but there are some skerries and land with flat terrain that reduces the wind speed. This is corrected for with tabulated data from NS-EN 1991-1-4:2005+NA:2009 (2009).

Table 4.4: Input of extreme wind at location Alpha for a return period of 50 years.

Direction, θ_{wind}	90°	150°
U_{10} [m/s]	32	27

The fetch wind at location Beta is provided by Borge and Nilsen (2021) and is given in table 4.5. Both wind directions are considered as an open fetch, see figure 4.3.

Table 4.5: Input of extreme wind at location Beta for a return period of 50 years.

Direction, θ_{wind}	135°	180°
U_{10} [m/s]	27	29

4.2 Design of numerical simulations

A numerical setup which resembles the practical use of SWAN in the industry is now established, and simulations with the model can now be designed to investigate the sensitivity of the model with regards to the three parameters chosen in the start of this chapter: grid resolution, size of computational domain, and wind fetch.

All simulations in the sensitivity study will be compared to a benchmark simulation for each site. The benchmark simulation has the following setup:

- Boundary conditions as given by table 4.2.
- Includes all nested grids described in chapter 4.1.1, where each nested grid has the same resolution as the bathymetry resolution presented in chapter 4.1.2.
- Size of computational domains are showed by figure 4.2 and figure 4.3.
- No wind is implemented in the computational grid.

Input files for the full area grid of each location is provided in Appendix E for the benchmark simulation.

In each study, changes from the benchmark simulation will be done one parameter at a time, and the rest will be kept equal to the benchmark. The studies will be performed as follows:

1. Grid resolution study.
   Consists of two independent parts:
   (a) Number of nested grids will be varied. As explained in chapter 4.1.1, the nesting grids improve the resolution in a specific areas of the grid. A simulation without nesting will first be run, before the nesting grids are included one at a time, starting with nesting 1, then nesting 2 etc.
   (b) The resolution of the computational grid in each nested grid is increased, one at a time. Note that the bathymetry resolution preferably should be increased if higher resolution data is available. After the results of part (b) of the resolution study were obtained for location Alpha, it was decided not to run this study for location Beta.

The resolution of each computational grid is given by the parameter R, and will be explained below.

2. Computational domain study.
   The size of the computational domain will be decreased. This corresponds to reducing the dimensions of the full area grid at the two locations. As a consequence, the boundary condition is set further away from the WAM model and the effects of the situation described in chapter 3.3, where the input WAM hindcast data is used at a potentially incompatible boundary in the SWAN model, can be analyzed. For Alpha, only the size of the domain in x-direction is decreased, as the offshore waves comes directly from the west. For Beta both x- and y-dimension of the grid are decreased, since the offshore waves comes from North-West. Note that the number of meshes (grid cells) in x- and y-direction is reduced correspondingly such that the resolution of the computational grid is the same as the benchmark simulation. The size of the computational domain in each direction is described by the parameters, K_x and K_y, which will be explained below.

3. Wind study.
   Wind implemented in the full area, then in one nested grid at a time will be simulated at both locations. In addition, the angle of the wind direction will be altered in each case. The corresponding wind speed for each direction will be set as given in table 4.4 and table 4.5. An example for one of the simulations in location Alpha is given in figure 4.10. Here, the wind is blowing in a 90° direction and is implemented in the wind nesting grid.

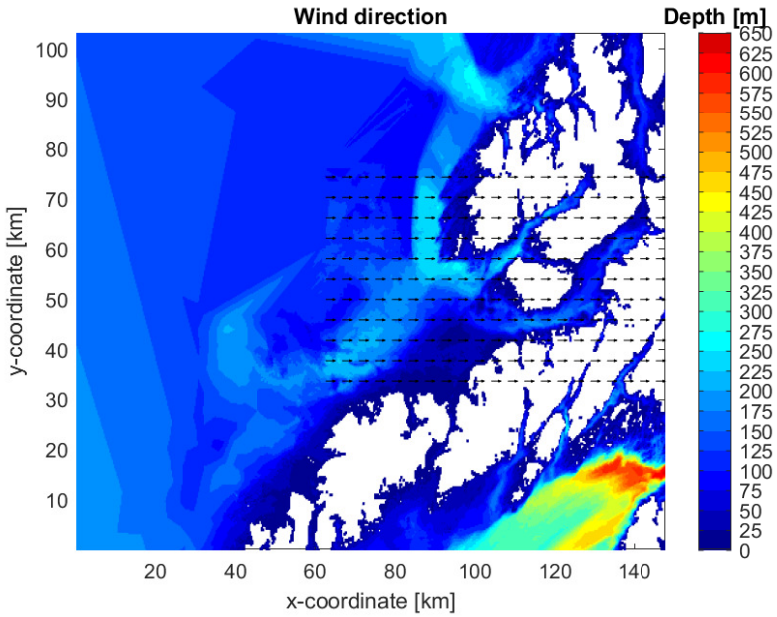

Figure 4.10: Wind inserted only in the wind nesting grid at location Alpha.

The area of a mesh is $dA = dx \cdot dy$, where dx and dy is the mesh size in each direction. R is the

increase in resolution from benchmark study, i.e.

$$R = \frac{dA_1}{dA_0}, \tag{4.1}$$

where $dA_1 = dx_1 \cdot dy_1$ is the mesh area with increased resolution, and $dA_0 = dy_0 \cdot dx_0$ is the mesh area in the benchmark simulation, see figure 4.11. In the resolution (b) study R was set to first set to 1.2 and then 1.5, i.e. a 20% and 50% increase in resolution, for one nested grid at a time. In the Resolution (a) study the resolution is kept constant in each grid, but only introducing one nesting between each simulation, as described above.

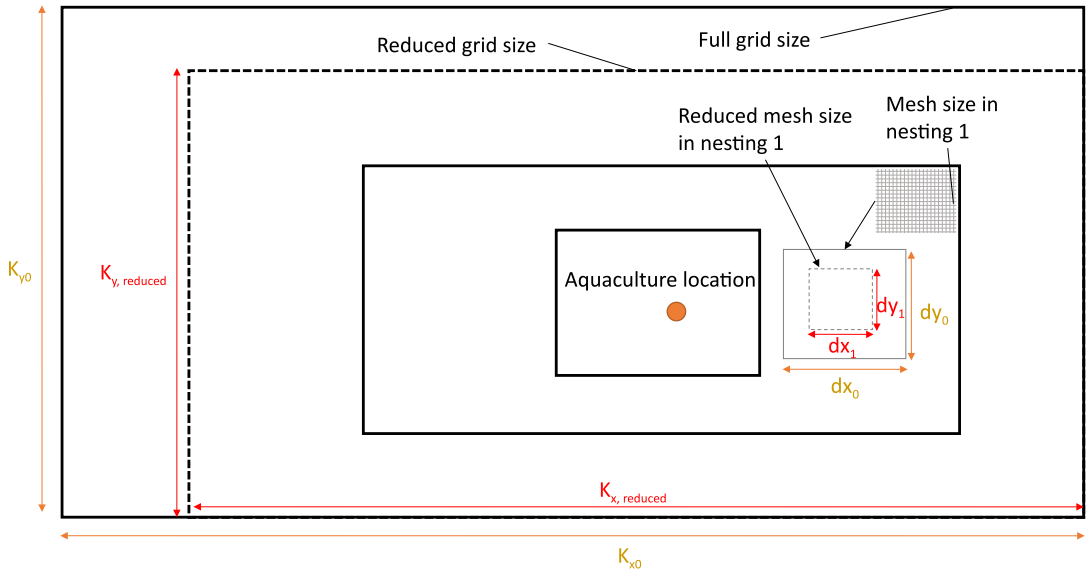

Figure 4.11: Conceptual sketch. In the resolution (b) study, the resoltuion of each nesting grid is increased from the benchmark simulation, such that a mesh with dimensions dx_0, dy_0 is reduced to dimensions dx_1, dy_1. In the computational domain study, the benchmark simulation with dimensions K_{x0} and K_{y0} on the largest grid is reduced to $K_{x,reduced}$ and $K_{y,reduced}$.

K_x and K_y is the measure of dimension in x- and y-direction of the full area grid and are defined as

$$K_x = \frac{K_{x,reduced}}{K_{x0}}, \tag{4.2}$$

$$K_y = \frac{K_{y,reduced}}{K_{y0}}, \tag{4.3}$$

where K_{x0} and K_{y0} are the dimensions in x- and y-direction in the benchmark simulation, and $K_{x,reduced}$ and $K_{y,reduced}$ are the dimensions of the reduced grid in the computational domain study. See figure 4.11. The different values of K_x and K_y in the computational domain study is given in table 4.6.

Table 4.6: Values of K_x, K_y (as defined in the text above) in the computational domain study for each location.

Alpha		Beta	
K_x	K_y	K_x	K_y
0.93	1	0.92	0.87
0.86	1	0.83	0.74
0.79	1	0.75	0.61
0.71	1	0.68	0.48
0.58	1	0.23	0.52

4.3 Choice of output properties

As can be seen from (*SWAN: User manual*, 2016, Appendix A) there are many properties that can be derived from the energy spectra of the SWAN model. In this study three properties are chosen:

- The significant wave height, H_s.
- The peak wave period, T_p.
- The peak wave direction, θ_{peak}.

H_s and T_p are the most important properties for determining wave exposure at aquaculture sites according to NS9415 (2009), and is therefore a suitable choice of parameters to plot. Moreover, the peak wave direction gives an overview of the propagation in the computational area and visualizes the evolution of the wave field throughout the computational domain.

As all properties are derived from the energy spectrum, the evolution of the energy spectrum from the boundary condition to the site locations will be given for the benchmark simulation at both locations. Moreover, the plot of on-site energy spectra will be given for all studies with comparison to the benchmark simulation. NS9415 (2009) also states that providing the on-site energy spectrum may be necessary. All plots of energy spectra are computed for all spectral directions (360°) with a directional resolution of 7.2°.

The properties on-site is represented by the results at point 17 for location Alpha, and point 7 for location Beta.

The MATLAB scripts used to read output files from SWAN and plot results are given and explained in Appendix F.

Chapter 5

Results

The results from the numerical simulations planned in chapter 4.2 are given in this chapter. For each location, the resulting conditions of the benchmark simulations will be given, before the results of each study is given and compared to the benchmark simulation.

The goal of each study is described in the start of chapter 4.

The properties chosen for representation of results are described in chapter 4.3.

5.1 Location Alpha

The resulting peak wave direction and significant wave height for the benchmark simulation, i.e. offshore waves with $\theta_{peak} = 90°$, are given in figure 5.1. The waves are unidirectional and show only small reduction in H_s for approximately 50 kilometers before they gradually turn towards the shore, and H_s is reduced more rapidly.

The energy spectra for point 2, 6, 10, and 17 are given in figure 5.2 for the benchmark simulation. The measuring points are placed at approximately the same y-coordinate, and the plot therefore shows the evolution of the energy spectrum as the wave field moves from the western boundary towards the fish farm location. The first peak has the same frequency as the input offshore waves. The swell peak is reduced as the wave field approach the aquaculture site, and a second peak (in the figure noted triads, more on that in chapter 6.1) with higher frequency appears.

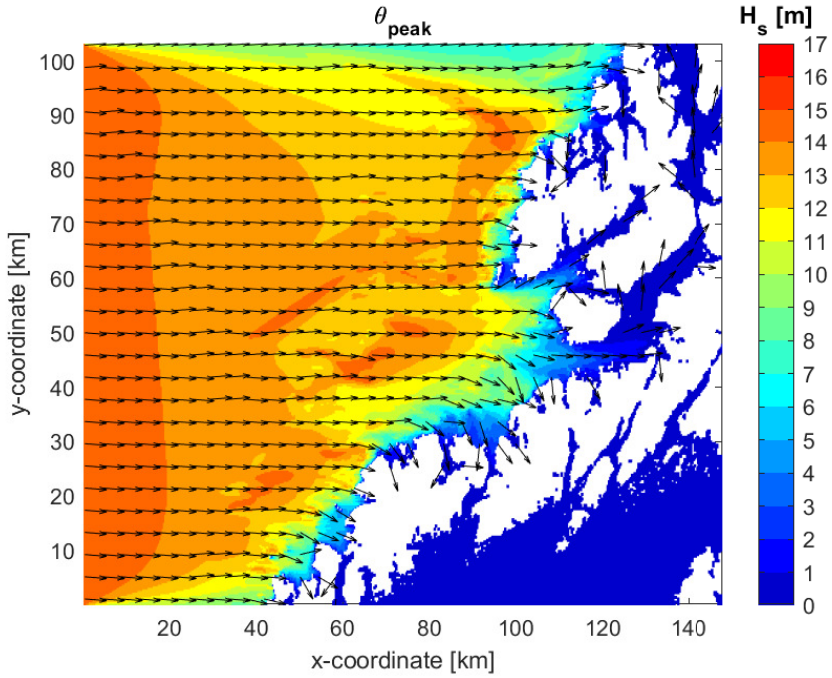

Figure 5.1: Peak wave direction, θ_{peak}, and significant wave height, H_s, for the benchmark simulation at location Alpha.

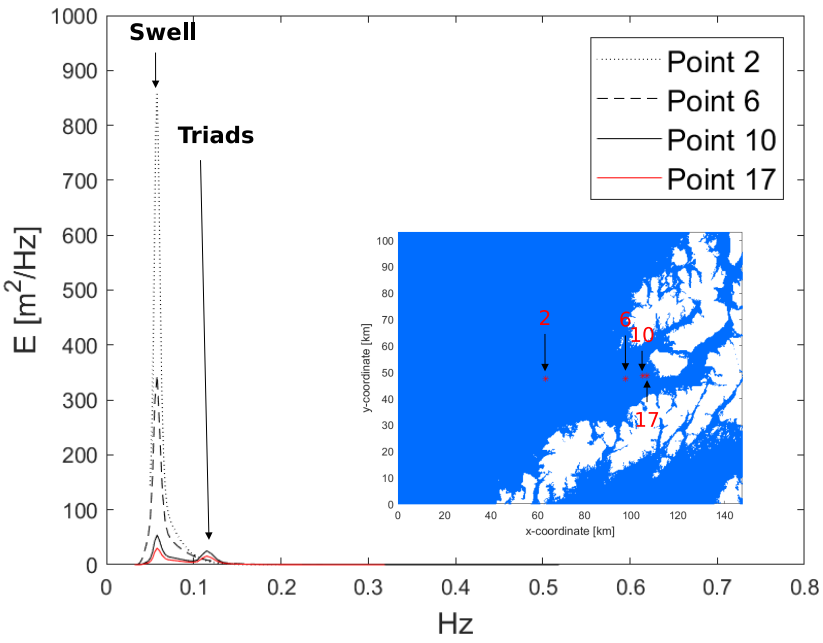

Figure 5.2: The energy spectrum, E for various measuring points in location Alpha, showing how the energy spectrum evolves through the computational domain.

5.1.1 Grid resolution study

5.1.1.1 Part (a)

In the first part of the grid resolution study, the nesting grids were included one at a time, starting from the outer grid. That is, first with the full area grid only, then with full area and wind nesting grid etc. When introducing more nesting grids, the resolution in proximity of the site is increased. The results for point 17, placed on-site, are given in table 5.1.

Table 5.1: On-site results (point 17) for grid resolution study (a) at location Alpha. Italic font for the benchmark simulation.

Grid(s) included	H_s [m]	T_p [s]	θ_{peak} [°]
Full area	5.27	17.16	100.80
Full area, wind nesting	5.28	17.17	100.80
Full area, wind nesting, nesting 1	3.91	17.13	100.80
Full area, wind nesting, nesting 1, nesting 2	*3.91*	*17.11*	*100.80*

The significant wave height as the waves travel from the western boundary ($x = 0$ km) to the site location is given in figure 5.3.

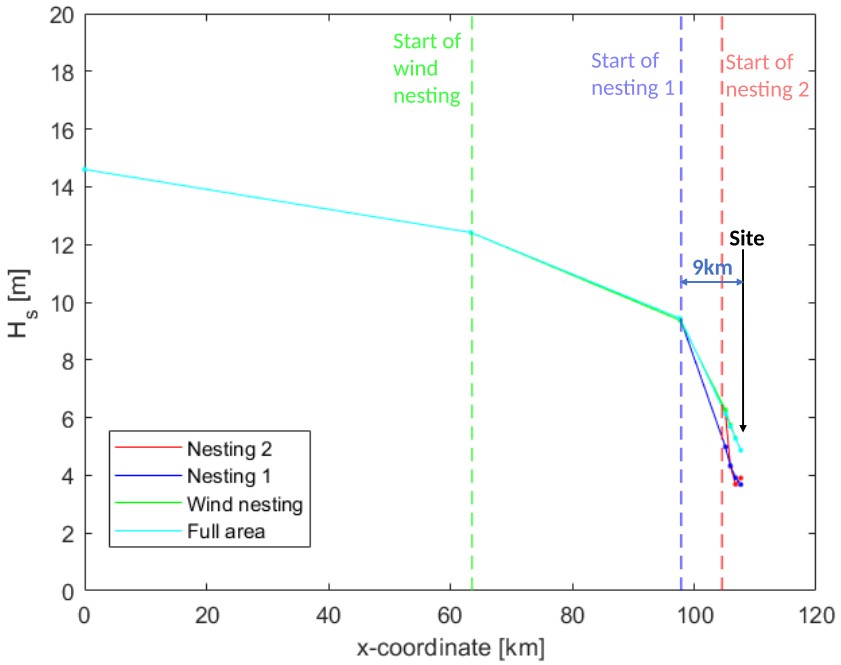

Figure 5.3: H_s as a function of x-coordinate in the grid resolution study (a) at location Alpha.

A reduction in wave height as the resolution increases is observed from figure 5.4. dA is the mesh area of the grid with highest resolution in the simulation. Note that the wind nesting has a slightly lower resolution than the full area grid, due to the bathymetry files used. See chapter 4.1.2. The largest difference came when nesting 1 is introduced, whereas there is only a small difference when nesting 2 is added.

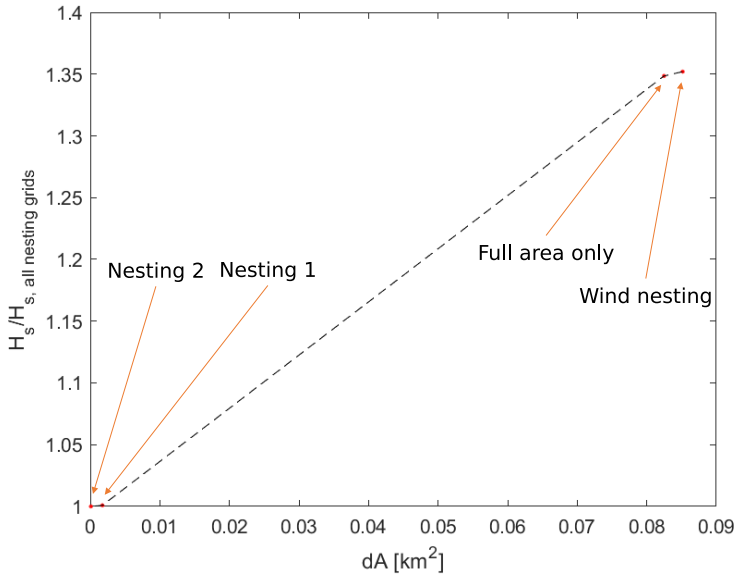

Figure 5.4: Change in significant wave height, H_s, from the significant wave height in the benchmark simulation (i.e. with all nested grids), $H_{\text{s, all nested grids}}$. dA is the mesh area of the grid with the highest resolution included in each simulation.

The energy spectra at measuring point 17 for each simulation is given in Appendix G.1. All spectra have the same form as in figure 5.2, but is reduced for each nesting introduced.

In the following studies at location Alpha, simulations will include all four nesting grids.

5.1.1.2 Part (b)

In **part (b)** of the resolution study, each nesting grid was increased with 20% and 50%. The bathymetry resolution was kept constant. Even though the computation time increased significantly, the results at all measuring points showed only negligible changes from the benchmark simulation to any of the output properties. This is clearly showed by the resulting H_s at the 5 measuring points in figure 5.5, where the resolution of the wind nesting grid was increased. The results are ultimately the same as for the benchmark simulation, and therefore not presented again.

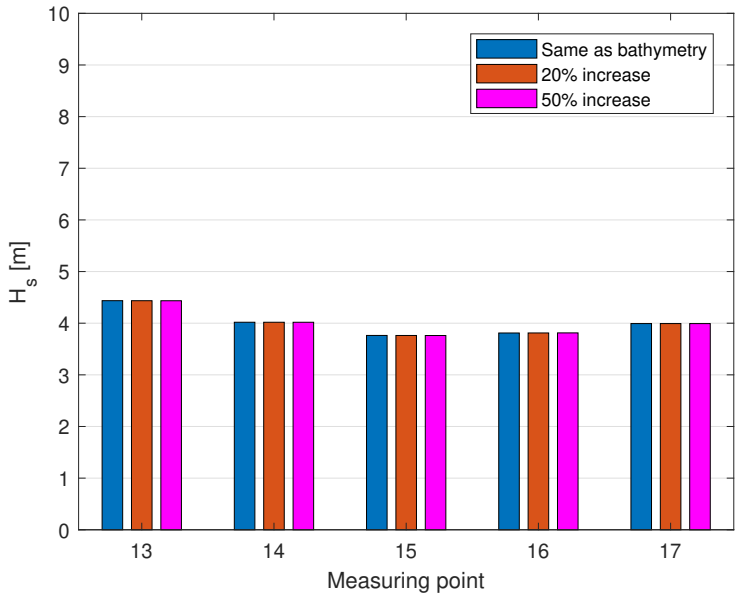

Figure 5.5: Significant wave height at the measuring points closest to the aquaculture site for different resolutions of the wind nesting grid (but with the same resolution of bathymetry) at location Alpha.

5.1.2 Computational domain study

The results at point 17 (on-site) from the computational domain study are given in table 5.2. When the domain is reduced from the benchmark simulation, there will be a mismatch between the location with known data from the WAM model and the western boundary (where the boundary condition is set).

Table 5.2: On-site (point 17) results of computational domain study at location Alpha. Italic font for the benchmark simulation.

K_x [-]	H_s [m]	T_p [s]	θ_{peak} [°]
1	*3.91*	*17.11*	*100.80*
0.93	3.94	17.11	100.80
0.86	3.97	17.11	100.80
0.78	3.99	17.10	100.80
0.72	4.05	17.07	100.80
0.58	4.11	17.11	100.80

The resulting significant wave height and peak wave direction of simulations with the smallest reduction of the computational domain, $K_x = 0.93$, and the largest reduction of the computational domain, $K_x = 0.58$, is given in figure 5.6. This corresponds to a reduction of approximately 10 kilometers and 60 kilometers, respectively.

The significant wave height as a function of distance from the western boundary is given in figure 5.7.

In figure 5.8, the change in significant wave height from the benchmark simulation ($K_x = 1$) on-

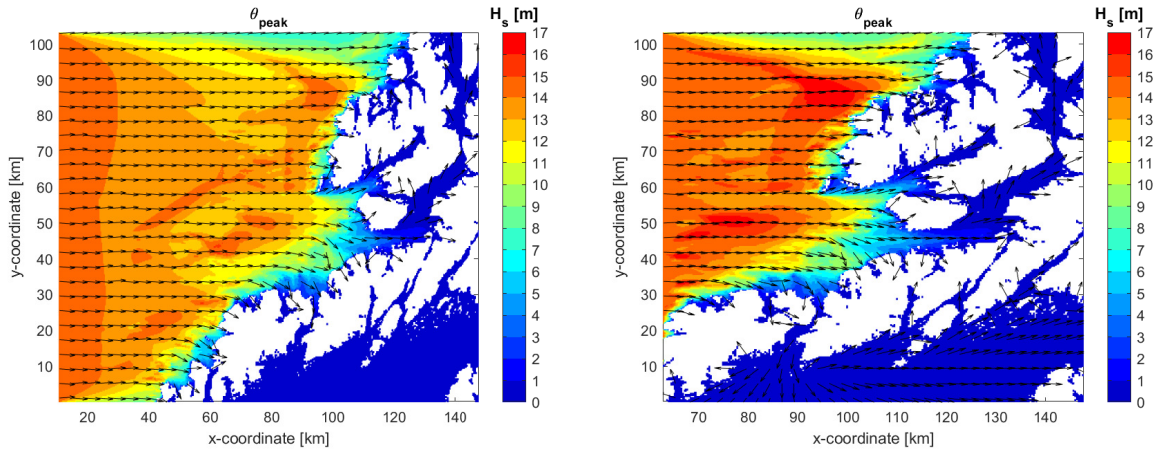

(a) $K_x = 0.93$ (b) $K_x = 0.58$.

Figure 5.6: The resulting peak wave direction and significant wave height from the simulation where the domain of the full area grid is reduced with 10 ($K_x = 0.93$) and 60 ($K_x = 0.58$) kilometers in x-direction.

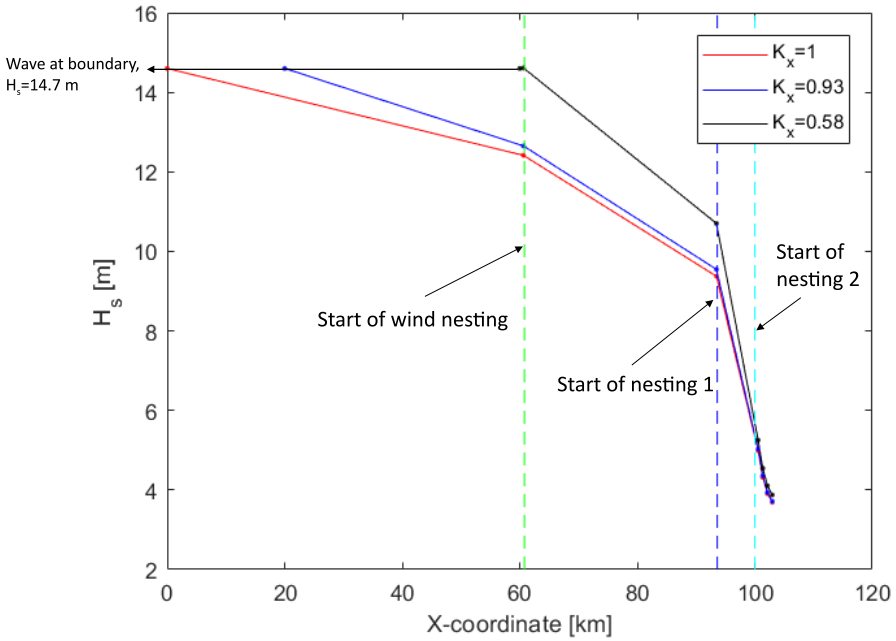

Figure 5.7: H_s as a function of the x-coordinate in the computational domain study at location Alpha.

site (measuring point 17) is given as a function of *the percentage reduction of the computational domain in x-direction*, namely $1 - K_x$. In the most extreme case, H_s has increased with 7.5% at the site location.

The energy spectra at point 17 for two most extreme scenarios, $K_x = 0.93$ and $K_x = 0.58$, is plotted with the spectrum from the benchmark simulation in Appendix G.1. All spectra have the same form, but the energy is increased for reduced size of the computational domain.

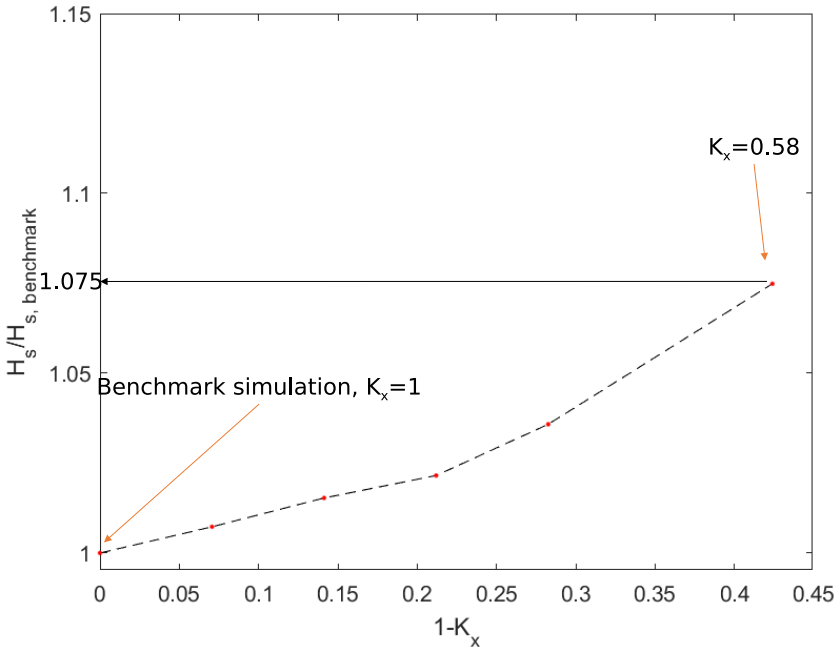

Figure 5.8: Increase in H_s from benchmark simulation at measuring point 17 as a function of percentage reduction of full area grid, $1 - K_x$, at location Alpha.

5.1.3 Wind study

The results from the wind study for point 17 (on-site) are given in table 5.3.

Table 5.3: On site (point 17) results of wind study at location Alpha. Italic font for the benchmark simulation (no wind).

Wind direction	Grid with wind	H_s [m]	T_p [s]	θ_{peak} [°]
No wind	*N/A*	*3.91*	*17.11*	*100.80*
$\theta_{wind} = 150°$	Full area	4.59	17.23	100.80
	Wind nesting	4.59	17.14	100.80
	Nesting 1	4.40	17.10	100.80
	Nesting 2	4.27	17.11	100.80
$\theta_{wind} = 90°$	Full area	5.60	17.15	100.80
	Wind nesting	5.56	17.07	100.80
	Nesting 1	5.14	17.08	100.80
	Nesting 2	4.29	17.11	100.80

The two simulations with wind with direction $\theta_{wind} = 150°$ (blowing towards South-East) and $\theta_{wind} = 90°$ (blowing towards East, i.e. in the same direction as the swell) in the full computational grid, are given in figure 5.9. The (peak) wave direction at the boundary, and the wind set in the whole full area grid is indicated at the top of each figure.

The significant wave height as a function of the x-coordinate is given in figure 5.10 for the wind

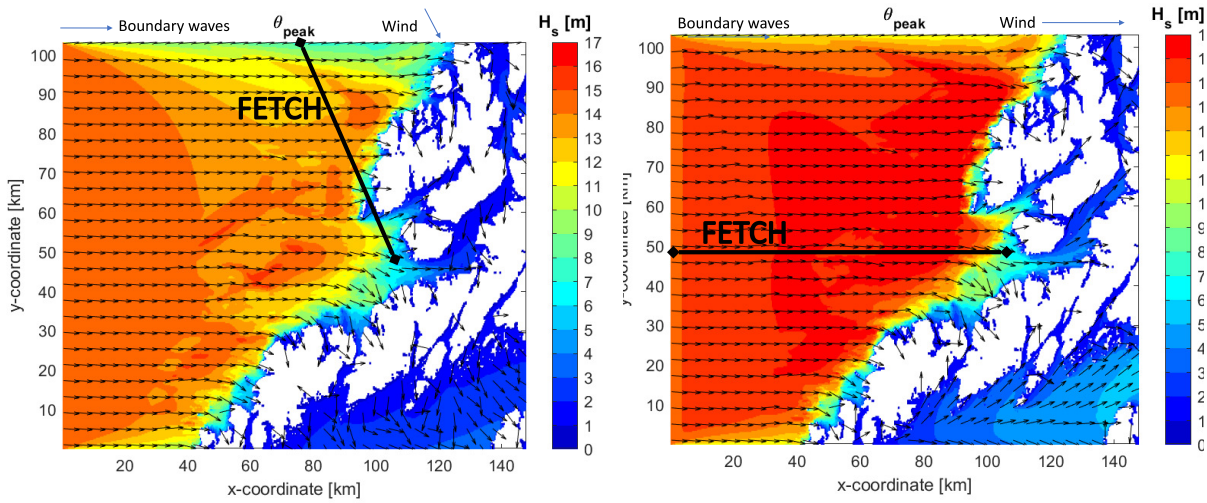

(a) $\theta_{wind} = 150°$. (b) $\theta_{wind} = 90°$

Figure 5.9: Resulting H_s and θ_{peak} for two simulations of different wind directions with wind implemented in the full area grid at location Alpha. Fetches for the two wind directions are indicated.

direction that increased the significant wave height the most, $\theta_{wind} = 90°$.

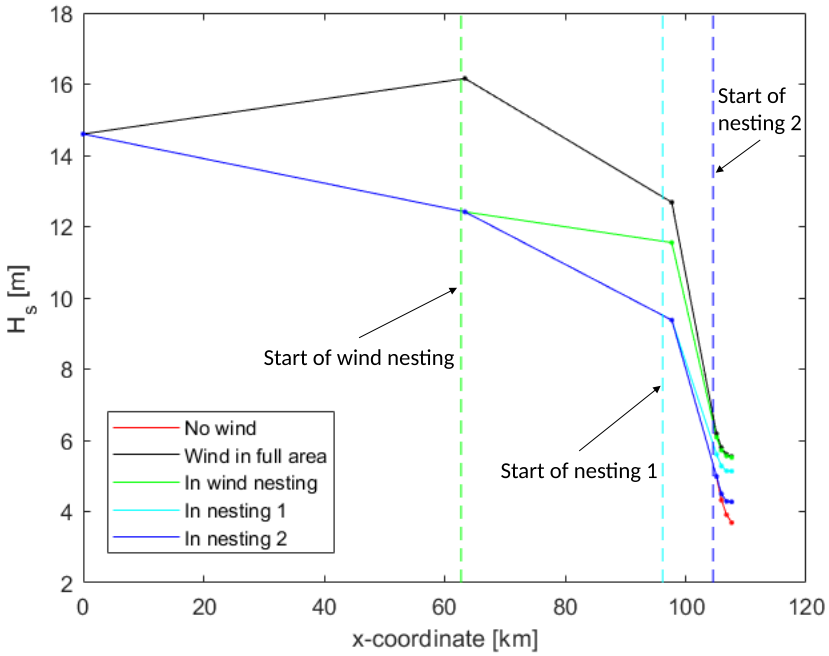

Figure 5.10: H_s vs x-coordinate for different wind implementation scenarios of $\theta_{wind} = 90°$ at location Alpha.

The percentage increase in significant wave height from the benchmark simulation (i.e. without wind, $H_{s,benchmark} = 3.91$ m) as a function of the fetch length is given in figure 5.11. The fetch is defined as the length from aquaculture site to the boundary of where the wind is coming from as illustrated in figure 5.9. When the fetch reaches a certain fetch limit, H_s on-site is not increased

any further.

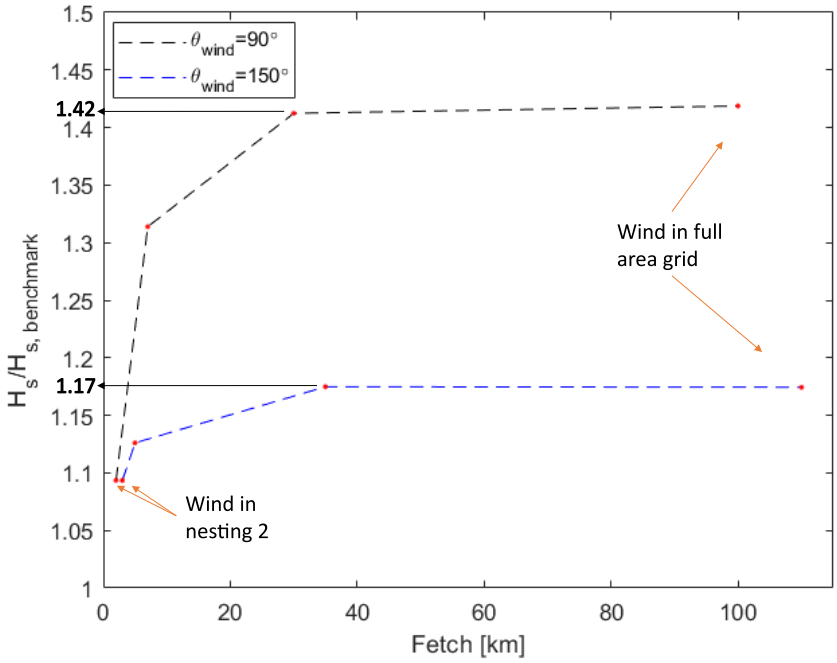

Figure 5.11: H_s on-site (measuring point 17) as a function of fetch at location Alpha.

The on-site energy spectra (measuring point 17) for wind implemented in the full area grid and wind nesting grid are given in figure 5.12. The wind increases the energy at higher frequencies than the swell peak. The energy is reduced at the swell peak frequency, however. The simulations with $\theta_{wind} = 90°$ has an increased energy at all frequencies compared to the simulations with $\theta_{wind} = 150°$. The energy spectra follow approximately the same form for both directions, however.

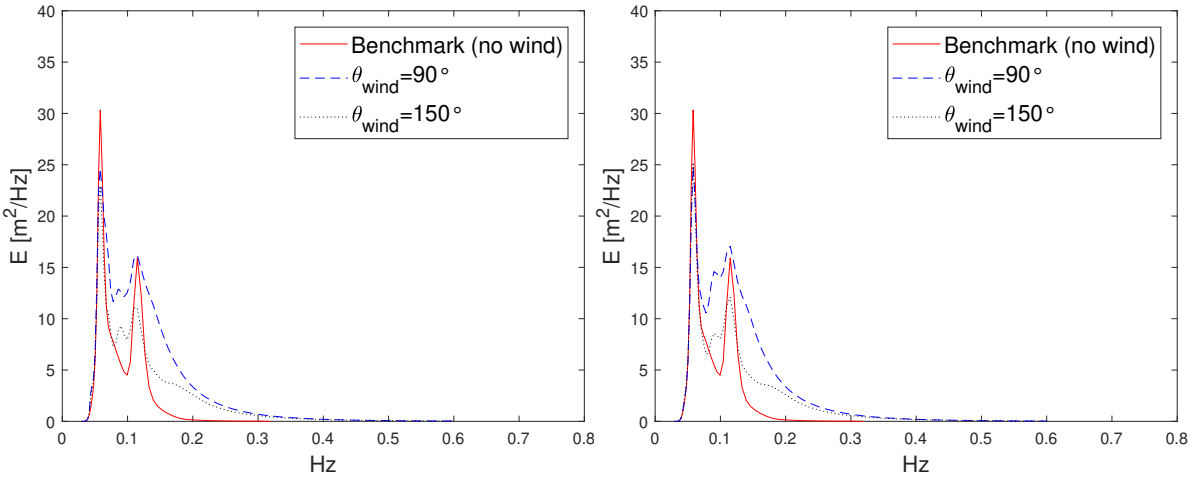

(a) Wind in full area grid.

(b) Wind in wind nesting grid.

Figure 5.12: Energy spectra, $E(f)$, on-site (point 17) for wind in different grids at location Alpha.

5.2 Location Beta

The resulting peak wave direction and significant wave height for the benchmark simulation, which is with incoming offshore waves with $\theta_{peak} = 130°$, i.e. waves going towards south-east, is given in figure 5.13. As for location Alpha, the waves are unidirectional for a distance (around 90 km) from the northwestern boundary, and show only small reduction of H_s, before they gradually turn and H_s is reduced more rapidly.

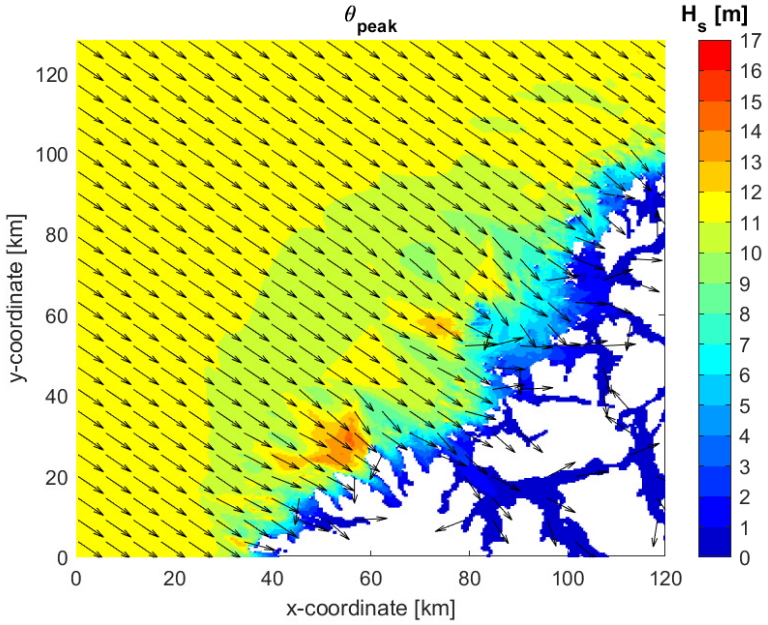

Figure 5.13: Peak wave direction, θ_{peak}, and significant wave height, H_s, for benchmark simulation at location Beta.

The evolution of the energy spectrum from the northwestern boundary to on-site measuring point 7 is given in figure 5.14. The points are marked in the figure. Due to long distances between points, the second peak (marked as triads) is not apparent before the on-site point, contrary to location Alpha where it was visible farther from the site. A scaling of the energy spectrum at point 7 is also provided in the figure, as it is much smaller than the other spectra.

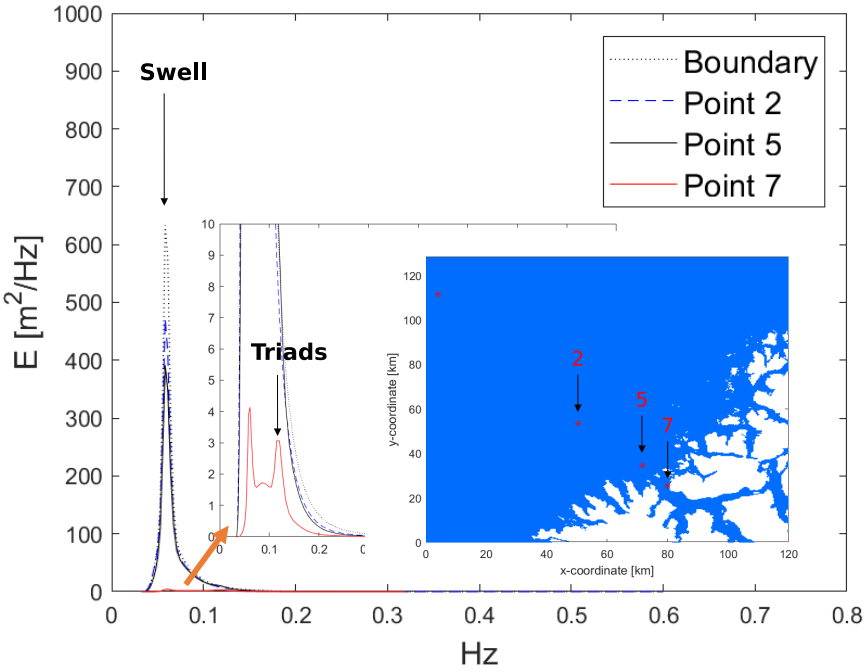

Figure 5.14: The energy spectrum, E, for various measuring points in location Beta, showing how the energy spectrum evolves through the computational domain.

5.2.1 Grid resolution study

5.2.1.1 Part (a)

The nesting grids were included one at a time, starting from the outer grid. That is, first the full area grid only, then with full area and nesting 1, and then with all the three nesting grids. The results at point 7 (on-site) for each simulation is given in table 5.4.

Table 5.4: On-site results (point 7) for grid resolution study (a) at location Beta. Italic font for the benchmark simulation.

Grid(s) included	H_s [m]	T_p [s]	θ_{peak} [°]
Full area	1.83	16.69	129.60
Full area, nesting 1	1.92	16.64	129.60
Full area, nesting 1, nesting 2	*2.08*	*16.68*	*129.60*

H_s as a function of distance the waves travel *from northwestern corner of the full area grid* is given in figure 5.15. The length traveled is defined as $-y/\sin\theta_{peak}$ where y is distance in y-direction, and θ_{peak} is the peak wave direction at the boundary. This is of course a simplification since θ_{peak} changes inside the grid, but as seen from figure 5.13, this effect is small.

Percentage change in significant wave height from the benchmark simulation (with every nested grid included) is given in figure 5.16. dA is the mesh area of the grid with highest resolution in the simulation. Both nesting 1 and nesting 2 increase H_s significantly, and seems to be necessary

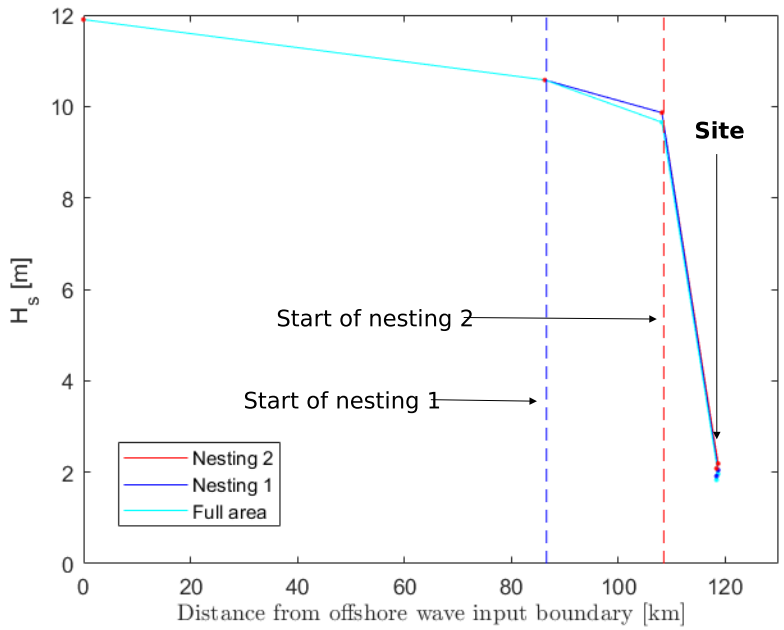

Figure 5.15: H_s as a function of the distance the waves have traveled from the northwestern corner of the full area grid, defined as $-y/\sin\theta_{peak}$ where y is the y-coordinate direction, and θ_{peak} is the peak wave direction at the boundary, in the grid resolution study (a) at location Beta.

to include in computations.

The on-site energy spectra at point 7 for the different simulations are given in Appendix G.2. The energy spectra have a similar form as in the benchmark simulation (figure 5.14), but the energy increases for higher resolutions.

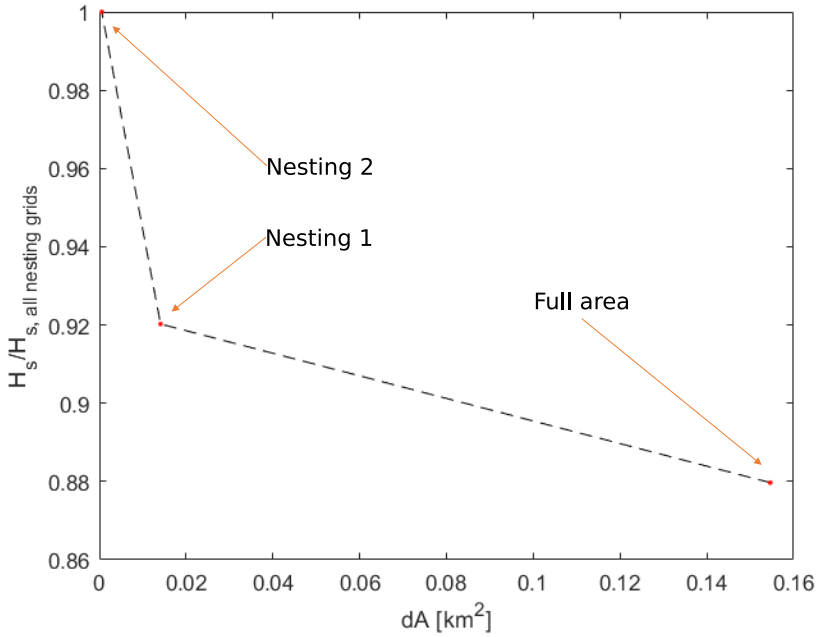

Figure 5.16: Change in significant wave height, H_s, from the significant wave height in the benchmark simulation (i.e. with all nested grids), $H_{\text{s, all nested grids}}$ at location Beta. dA is the mesh area of the grid with the highest resolution included in each simulation.

5.2.2 Computational domain study

The on-site (point 7) results from the computational domain study are given in table 5.5. When the grid is reduced from the benchmark simulation, there will be a mismatch between the location with known data from the WAM model and the northwestern boundary (where the boundary condition is set).

Table 5.5: On-site (point 7) results of the computational domain study at location Beta. Benchmark simulation in italic font.

K_x [-]	K_y [-]	H_s [m]	T_p [s]	θ_{peak} [°]
1	*1*	*2.08*	*16.68*	*129.60*
0.92	0.87	2.10	16.67	129.60
0.83	0.74	2.12	16.66	129.60
0.75	0.61	2.15	16.66	129.60
0.68	0.48	2.22	16.64	129.60
0.23	0.52	2.27	16.63	129.60

The results of the simulations with the smallest reduction of the computational domain, and the simulation with largest reduction of the computational domain are given in figure 5.17.

The significant wave height as a function of distance from the northwestern boundary, defined as $y/\sin 150°$, where y is the distance y-direction, is given in figure 5.18 for the minimum and

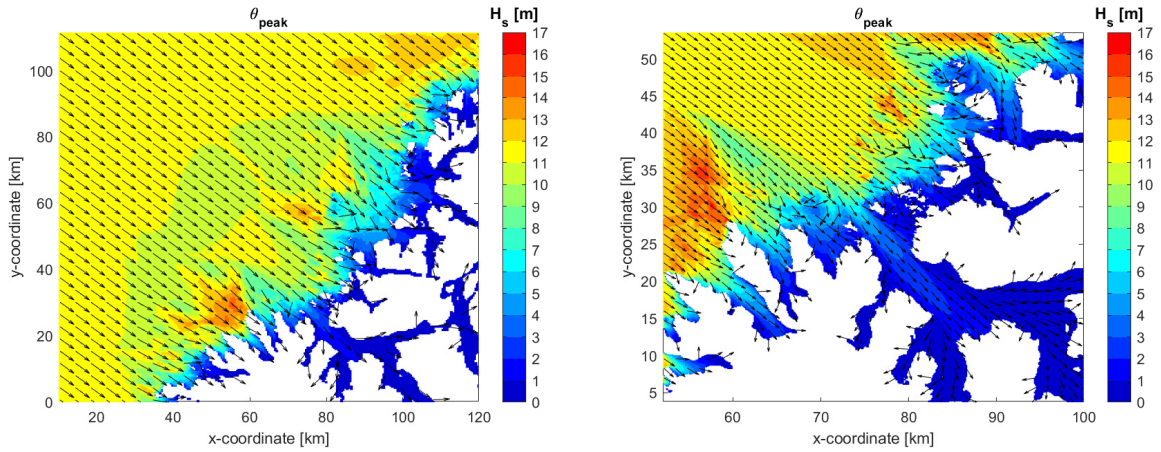

(a) Minimum reduction.

(b) Maximum reduction.

Figure 5.17: The resulting peak wave direction and significant wave height from the simulations where the full area grid is reduced with 9 km in x-direction any 5 km in y-direction ($K_x = 0.92$, $K_y = 0.87$) and 86 km in x-direction and 19 km i y-direction ($K_x = 0.23$, $K_y = 52$) at location Beta.

maximum reduction of the computational domain, in addition to the benchmark simulation.

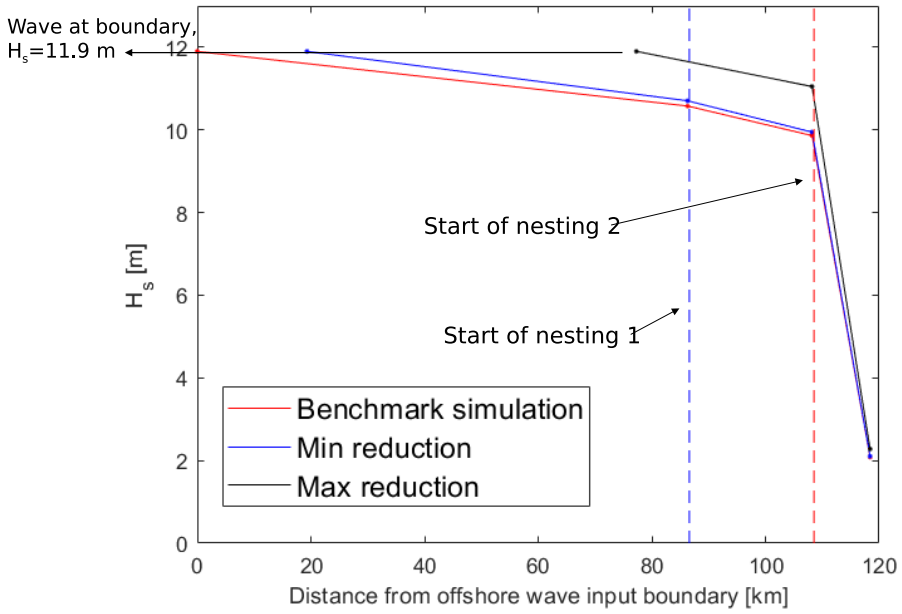

Figure 5.18: H_s as a function of the length the waves travel from the North-West boundary of the computational domain, defined as $-y/\sin\theta_{peak}$ where y is the length in y-direction from the boundary to the site, and θ_{peak} is the peak wave direction at the boundary, in the computational domain study at location Beta.

The percentage change in H_s from benchmark simulation, namely $H_s/H_{s,benchmark}$ is given in figure 5.19. *Reduction of grid dimension* (x-axis in plot) is the mean value of $1-K_x$ and $1-K_y$. It shows a steady increase in H_s for reduced dimensions of the full area grid, and the maximum

reduction resulted in a 8.5% increase in H_s on-site compared to benchmark simulation.

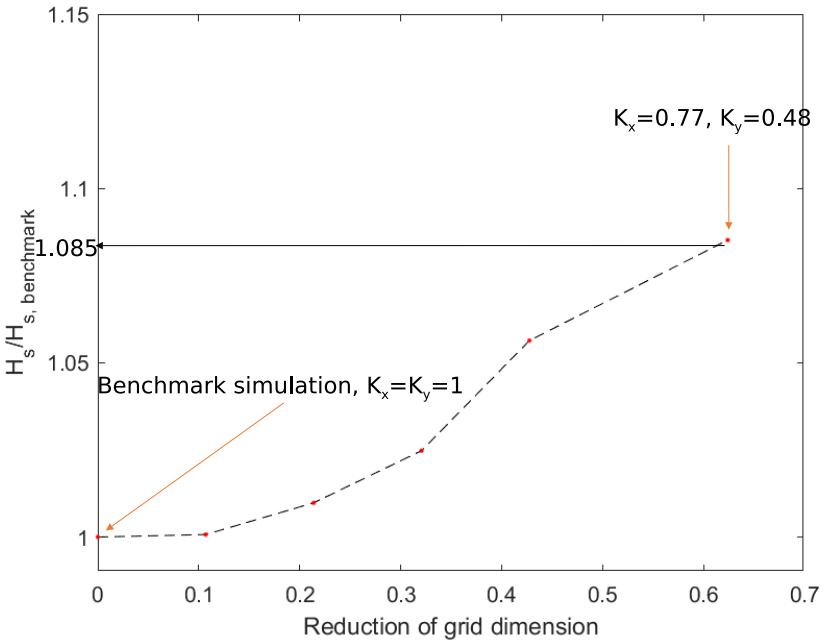

Figure 5.19: Increase in H_s from benchmark simulation at measuring point 7 (on-site) as a function of the mean reduction of full area grid in each direction, namely $1 - (K_x + K_y)/2$ at location Beta.

The energy spectra at measuring point 7 (on-site) for the minimum and maximum reduction of full area grid dimension is given in Appendix G.2. All energy spectra have the same form, but magnitude varies in correspondence with the earlier presented H_s results, as it did for location Alpha.

5.2.3 Wind study

The results for point 7 (on-site) for the wind study simulations are given in table 5.6.

Table 5.6: On-site (point 7) results of wind study at location Beta.

Wind direction	Grid with wind	H_s [m]	T_p [s]	θ_{peak} [°]
No wind	*N/A*	*2.08*	*16.68*	*129.60*
$\theta_{wind} = 180°$	Full area	3.21	16.73	129.60
	Nesting 1	3.27	16.67	129.60
	Nesting 2	3.16	16.68	129.60
$\theta_{wind} = 135°$	Full area	3.76	16.65	129.60
	Nesting 1	3.75	16.63	129.60
	Nesting 2	3.18	16.67	129.60

Resulting H_s and θ_{peak} when the is wind set in the full area grid (i.e. longest fetch) are given for both directions in figure 5.20. The wind and boundary wave directions are indicated on top of the figure.

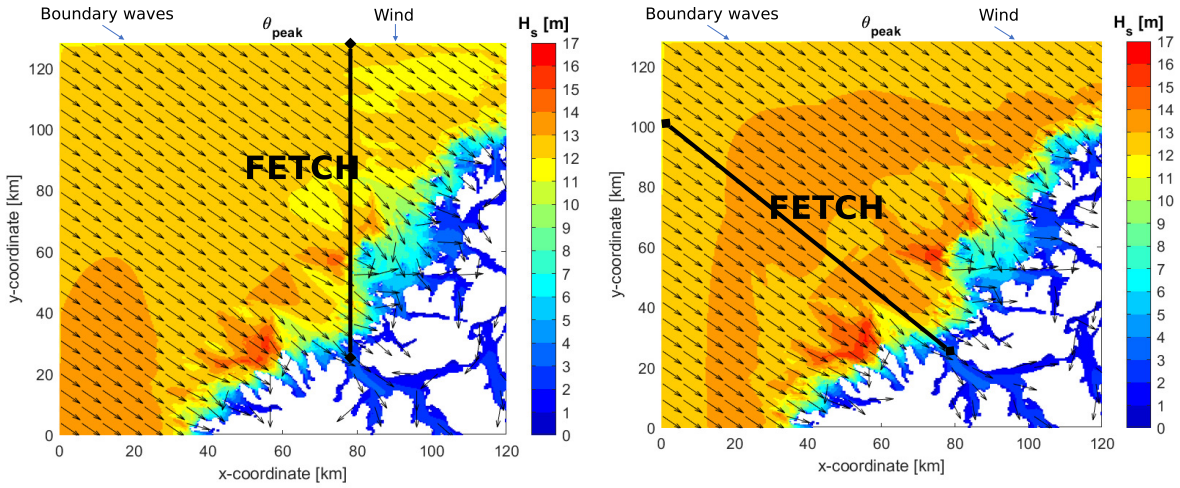

(a) $\theta_{wind} = 180°$.

(b) $\theta_{wind} = 135°$

Figure 5.20: Resulting H_s and θ_{peak} for two simulations with wind implemented in the full area grid of location Beta.

The significant wave height as a function of the length the waves have traveled is given in figure 5.21 for the wind direction that increased H_s the most, $\theta_{wind} = 135°$.

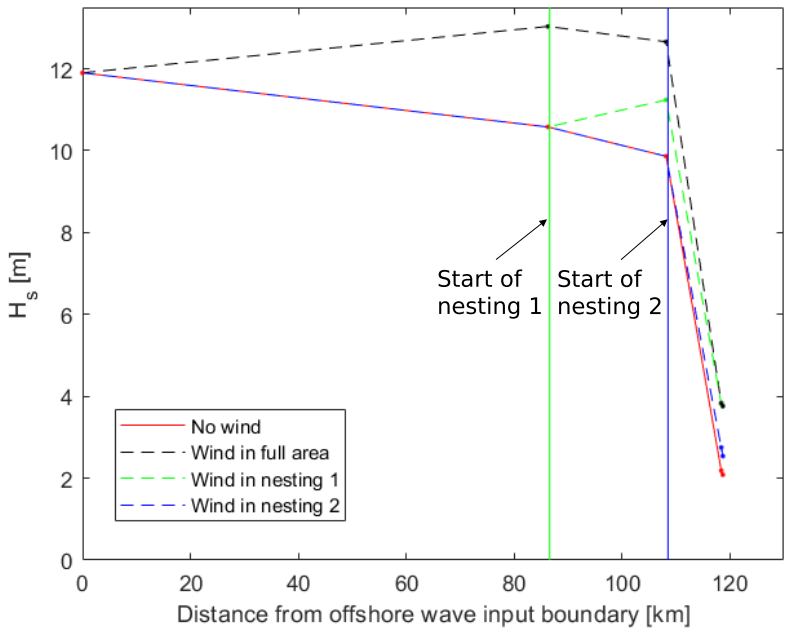

Figure 5.21: H_s as a function of the distance from offshore wave input boundary, defined as $-y/\sin\theta_{peak}$ where y is the length in y-direction from the boundary to the site, and θ_{peak} is the peak wave direction at the boundary, for different wind implementation scenarios of $\theta_{wind} = 135°$ at location Beta.

Change in H_s from benchmark simulation for different fetch lengths is given by figure 5.22, where fetch length is defined as the length from the site location to the boundary of the wind

field, as seen in figure 5.20. For $\theta_{wind} = 135°$ the same pattern as in location Alpha is visible: There is no change in H_s on-site between wind in full area and in nesting 1 (which gives a 30-40 km fetch). For $\theta_{wind} = 180°$, H_s is slightly reduced beyond this fetch limit, however.

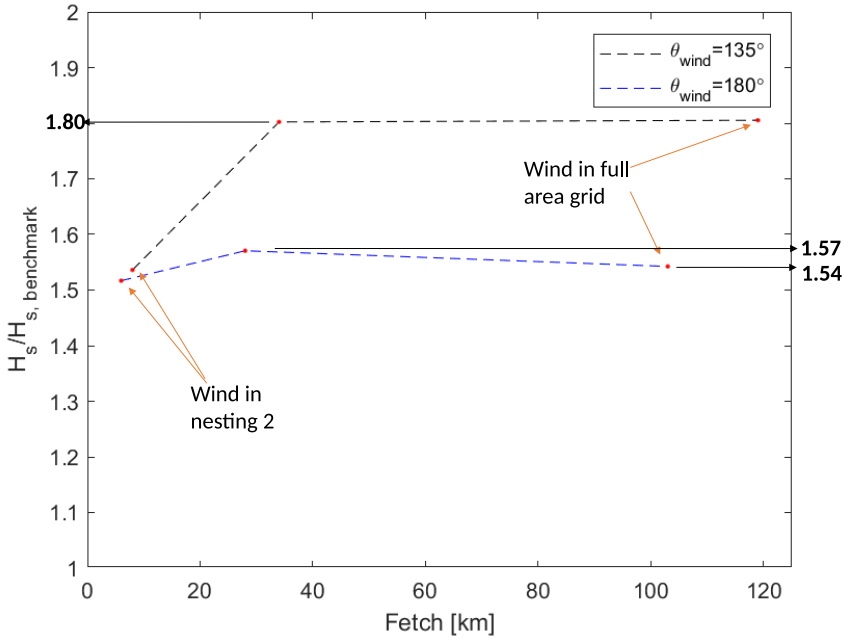

Figure 5.22: Correlation between H_s and fetch for different wind implementation scenarios of $\theta_{wind} = 135°$ at location Beta.

Energy spectrum with wind implemented in both directions in the full area is given in figure 5.23.

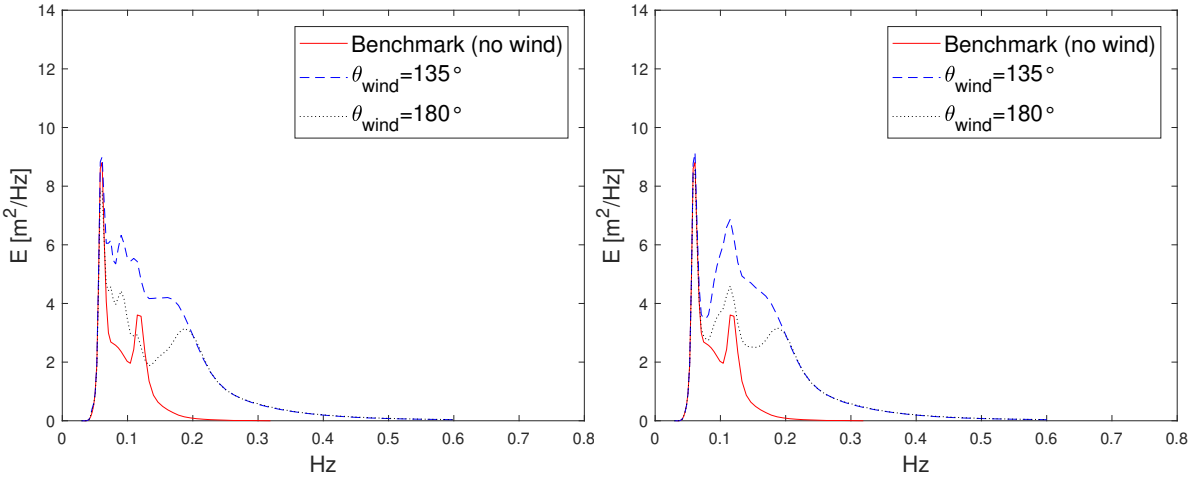

(a) Wind in full area grid.

(b) Wind in wind nesting grid.

Figure 5.23: $E(f)$ for wind in different grids at point 7 (on site) at location Beta.

Chapter 6

Discussion, conclusion, and further work

6.1 Discussion

The results in the previous chapter must be assessed with the numerical setup, design of experiments, and literature study in mind. That is, to understand if the main objective of this thesis has been met through the results, one must also consider the methodology used to obtain them. This will be covered in this chapter, along with an assessment of potential sources of error imposed by the work in this thesis.

The benchmark simulation results of peak wave direction, θ_{peak}, and significant wave height, H_s, are given in figure 5.1 and figure 5.13 for location Alpha and Beta respectively, and are suitable for a first assessment of the locations. It is not until the waves are in proximity of the shore that change in direction is noticeable. At location Alpha there are few obstacles close to the site, and thus little diffraction. In location Beta, the waves diffract around the skerries north-west of the site, but it does not seem to have a large impact on H_s. This indicates that SWAN is suitable for simulations on both locations, and that secondary objective 1 is met. It should be noted that this is a qualitative assessment of each site, and that validation can only be obtained with comparison to measurements. Moreover, waves from other directions may cause more diffraction patterns, e.g. waves from west at location Beta may diffract around the headland west of the site.

The on-site peak wave direction θ_{peak} and peak wave period, T_p, show only small changes between all simulations in the sensitivity study. However, this is only the peak parameters, and the full picture of the wave field energy distributed over period and direction is better seen from the energy spectra. Only the one-dimensional spectrum is provided in this thesis however, and it does not provide the directional distribution. This could be a limitation in the wind implementation study in particular, where one would expect the energy spectrum to have a

larger directional spreading.

From figure 5.2 (Alpha) and figure 5.14 (Beta) the evolution of the energy spectra are provided. At both locations the initial spectrum, which is narrow and has low-frequent swell peak, develops an additional peak at higher frequency than the input offshore waves at the on-site point. This comes from triads (see figure 3.10), and highlights the importance of including the triad source term in simulations. In fact, the triad peak is of the same magnitude as the swell peak on-site, and also shows the limitations of only considering peak wave period to classify aquaculture sites in NS9415 (2009) as it will not consider both peaks.

In part (a) of the resolution study, the influence of nested grids with increased resolution is found. For Alpha, figure 5.4 shows that introducing nesting 2 gave almost no impact on H_s on-site, indicating that the results have already converged in proximity of the site, and that nesting 2 is redundant. For Beta, figure 5.16 shows that introducing nesting 2 to the simulation changed the results, meaning that a higher resolution could be necessary. Nevertheless, it is not possible to conclude if the resolution is sufficient in all nesting grids from part (a) of the study, because the dimension of each nesting also impacts the results. As an example, the distance from nesting 2 of Alpha to site location is showed in figure 5.3. It is therefore not possible to say if the resolution is sufficient at the two locations from resolution study (a) only.

The methodology for part (b) of the resolution study is a better way to validate that the results converge, as the dimension of each nesting is kept constant. However, as figure 5.5 shows, increase in grid resolution without also increasing the bathymetry resolution gave no effect. This could also be because the results have already converged for the lowest resolution. Nevertheless, it is not possible to say definitely that a satisfying resolution is used for the bathymetry. If the resolution of bathymetry can be varied, it should be included in the study. A suggestion is to vary it together with the computational grid resolution (i.e. keep them equal). As resolution studies are not part of any standard, models developed by industry actors may potentially have a coarse computational grid and bathymetry which does not solve wave transformations sufficiently.

Reducing the computational grid gives a steady increase in significant wave height at both sites. The simulations are visualized by plots of H_s as a function of the distance the waves travel from boundary. It shows that setting the boundary condition closer to the site gives a consequential error throughout the computational grid. The most extreme reductions results in an increase of 7.5% and 8.5%, seen from figure 5.8 and figure 5.19, for location Alpha and Beta respectively. The results are in-line with what is expected, and shows the importance of setting the correct computational domain such that they are compatible with the measured datapoint, in this case a generation scale model (WAM). Two of the simulations for each site are illustrated by figure 5.6 (Alpha) and figure 5.17 (Beta).

Implementation of wind induced on-site H_s to increase with 42% and 80% for the two locations,

with wind blowing in the same direction as the incoming offshore waves. Moreover, the observed on-site H_s varies with fetch. On-site H_s as a function of fetch is given in figure 5.11 (Alpha) and figure 5.22 (Beta), and it shows that increased fetch actually has almost no effect past a certain limit. This indicates that a certain fetch gives a fully developed sea state (i.e. that dissipation is in balance with the wave generation and wave heights stops to increase). The limit is approximately 30 km for both sites, but due to few datapoints it is difficult to say if this fetch limit could be less for both locations. The simulations are only for two wind directions at each site, and one boundary wave direction.

Simulations with wind also lead to a wave field with more energy at higher frequencies, as seen in figure 5.12 (Alpha) and figure 5.23 (Beta). For structures where the natural frequency could be of importance, closed/semi-closed cages, feeding fleet etc., this is an important aspect to consider, which further highlights the importance of considering the on-site energy spectra and not only the peak period when assessing aquaculture sites.

It is arguable whether the variations in each study are realistic with regards to the variation between models set up by industry actors (secondary objective 3). There are infinite ways to nest the grid area, and infinite resolutions to use inside each grid. Moreover, it is not verified whether industry actors actually reduce the size of their computational domain such that there is a mismatch between set boundary conditions and hindcast data. As a result, the chosen intervals of K_x and K_y are also highly subjective. There is also no study available as to how the different industry actors implement wind. The extreme values of the three studies (no nested grids, smallest computational domain, wind only in a small area) should therefore be handled with care, as they do not necessarily provide realistic resemblance of choices in the industry.

There are some simplifications and assumptions with regards to the numerical setup (secondary objective 3(a)) that may affect results. First of all, the setup largely follows procedures and recommendations from only one industry actor, Multiconsult, and could therefore deviate from other actors. As mentioned above, a prominent source of error is the constant bathymetry resolution. The resolution study was not able to verify that the bathymetry captures the spatial complexities in each nested grid, as the resolution could not be increased to check if the results converge. Moreover, the magnitude of each source term is never assessed, and some are turned off on the assumption that they are insignificant, but without verification. For the boundary condition, the WAM hindcast data consists of a combined sea state, i.e. due to both local wind and swell. To simplify the shape of the energy spectrum at the boundary to a one-peaked swell characteristic shape is of course a potential source of error, even if the long distance from the boundary to the site might cause the waves to disperse anyway. The use of only one WAM hindcast point to set the full boundary conditions is also a source of error that potentially give inaccurate results. Moreover at location Alpha, the hindcast point is already outside the domain, and the mismatch between boundary conditions and hindcast point occurs for even the largest domain. The set wind speed and direction from NS-EN 1991-1-4:2005+NA:2009 (2009) should

be fairly consistent across industry actors, as it is the mandatory method when the local wind measurements does not cover a long enough time span (NS9415, 2009). It should however be noted that using both a local wind and offshore waves with return period of 50 years gives a conservative estimate of wave exposure, even though this is also mandatory by NS9415 (2009).

One must also take into account potential errors from misinterpretations in the literature study (secondary objective 2). The literature study forms knowledge-based decisions for the numerical setup, what parameters to conduct a sensitivity study on, and design of experiments. Spectral wave modelling is a complex topic, and the method of SWAN is developed by a team with high competence on the topic, over a large time span. The extent of this thesis is therefore only able to capture parts of this. The literature with regards to use of SWAN in Norwegian coastal areas also covers complex problems and, in turn, results, and misinterpretations could occur.

The methodology to set up the model is adaptable, and studies at other locations would therefore be possible with the same approach. The developed method to obtain bathymetry (with DIVEMesh) should be possible to use for sites along the whole Norwegian coast, as long as Kartverket (2021) has the data. Moreover, the boundary conditions from WAM models, and wind from NS-EN 1991-1-4:2005+NA:2009 (2009) should also be available for majority of site locations, but it is important to be aware of their limitations. The source term setup should be suitable for most sites, but it is advised to use the KOMEN method of SWAN instead of WESTH if the site is more sheltered than the two locations analyzed in this thesis. A standardized methodology for all industry actors, which in turn is tuned for local variations, could be a future solution to minimize errors with SWAN applied in aquaculture industry.

6.2 Conclusion

The main objective of this thesis is **to perform a sensitivity study on the most important parameters of the SWAN wave model applied to site assessment in Norwegian aquaculture industry.**

A sensitivity study is conducted for grid resolution, size of computational domain, and implementation of wind for the two locations Alpha and Beta. The grid resolution study shows the importance of resolution, but fails to determine whether the resolution was sufficient for the two locations, due to lack of higher resolved bathymetry data. The computational domain study highlights the importance of having a large enough domain so that the boundary conditions are placed at the same location as the hindcast datapoint (used to parameterize the boundary condition), and a too small grid may result in an overapproximation of H_s. The wind study shows that the fetch of the implemented wind will affect how large H_s is on-site, but when the fetch exceeds approximately 30 km, H_s does not change notably, which indicates that a 30 km fetch gives a fully developed sea state at the two locations.

It is not verified whether the sensitivity study fully succeeded in resembling the use of SWAN in Norwegian aquaculture industry. The numerical setup is largely based on setup from one industry actor, and may therefore not be representative for the whole industry. Furthermore, it is never verified how much the three parameters in the sensitivity study actually differ between actors, and the chosen intervals are therefore highly subjective. On the other hand, this thesis highlights the sensitivity of the model, and a standardized method for all industry actors could be required to minimize errors associated with use of SWAN in Norwegian aquaculture.

6.3 Suggestions for further work

There are two suggestions for further work, based on the work of this thesis:

- Investigate what input different industry actors use in SWAN. By mapping the different approaches, choices and simplifications, an overview of the deviations between actors is achieved, which, in turn, will improve a sensitivity study.
- Compare the SWAN analysis with a phase-resolved model and/or measurements. This is a different approach to the one taken in this thesis. This is a project Weizhi Wang (post-doctoral fellow), Hans Bihs (Associate Professor), Pål Lader (Professor) from NTNU, and the present author will investigate with the phase-resolved model REEF3D::FNPF (Bihs et al., 2020).

It should be emphasized that since SWAN allows different variations of numerical setups and output properties, it also enables numerous ways to study this subject further.

Bibliography

Babanin, A., Young, I. and Banner, M. (2001), 'Breaking probabilities for dominant surface waves on water of finite constant depth', *Journal of Geophysical Research-Oceans* **106**.

Battjes, J. and Janssen, H. (1978), 'Energy loss and set-up due to breaking random waves', *Proceedings of the 16th International Conference on Coastal Engineering* **1**.

Bihs, H., Wang, W., Pakozdi, C. and Kamath, A. (2020), 'REEF3D::FNPF—A Flexible Fully Nonlinear Potential Flow Solver', *Journal of Offshore Mechanics and Arctic Engineering* **142**(4).

Borge, J. and Nilsen, Ø. (2021), Metocean report. Internal report from analysis on location BETA.

Christakos, K., Björkqvist, J.-V., Tuomi, L., Furevik, B. and Breivik, Ø. (2020), 'Modelling wave growth in narrow fetch geometries: The white-capping and wind input formulations', *Ocean Modelling* .

Christakos, K., Furevik, B. R., Aarnes, O. J., Breivik, Ø., Tuomi, L. and Byrkjedal, Ø. (2020), 'The importance of wind forcing in fjord wave modelling', *Ocean Dynamics* **70**(1), 57–75.

CoastalWiki (2020), http://www.coastalwiki.org/wiki/White_capping. Image. Last checked 20.04.2021.

DIVEMesh user guide (2020). By the SWAN team (Cycle III version 41.31A).

DNV-RP-C205 (2017), Recommended practice DNV-RP-C205: environmental conditions and environmental loads, Technical report, Det Norske Veritas (DNV).

Faltinsen, O. M. and Shen, Y. (2018), 'Wave and current effects on floating fish farms', *Journal of Marine Science and Application* **17**(3), 284–296.

FAO (2020), 'The State of World Fisheries and Aquaculture 2020. Sustainability in action'.

Fauske, M. (2020), 'Atlantic salmon, rainbow trout and trout - grow out production', https://www.fiskeridir.no/Akvakultur/Tall-og-analyse/Akvakulturstatistikk-tidsserier/Laks-regnbueoerret-og-oerret/Matfiskproduksjon. Updated 29.10.2020.

Fergestad, D., Økland, O. D., Stefanakos, C., Stansberg, C. T., Croonenborghs, E., Eliassen, L. and Eidnes, G. (2018), 'LFCS Review report-Environmental conditions Wind, wave and current in coastal areas'.

Foley, J. A., DeFries, R., Asner, G. P., Barford, C., Bonan, G., Carpenter, S. R., Chapin, F. S., Coe, M. T., Daily, G. C., Gibbs, H. K. et al. (2005), 'Global consequences of land use'.

Hasselmann, K. F., Barnett, T. P., Bouws, E., Carlson, H., Cartwright, D. E., Eake, K., Euring, J., Gicnapp, A., Hasselmann, D., Kruseman, P. et al. (1973), 'Measurements of wind-wave growth and swell decay during the Joint North Sea Wave Project (JONSWAP).', *Ergaenzungsheft zur Deutschen Hydrographischen Zeitschrift, Reihe A* .

Hestnes, I. and Torkildson, K. (2021), Metocean report. Internal report from analysis on location BETA.

Holthuijsen, L. H. (2007), *Waves in Oceanic and Coastal Waters*, 1. edn, Cambridge University Press.

Kartverket (2021), https://www.geonorge.no/. Map catalog from Kartverket.

Kraugerud, R. L. (2021), 'Ulike typer oppdrettsanlegg', https://nofima.no/verdt-a-vite/ulike-typer-oppdrettsanlegg/#:~:text=Eksponerte%20lokaliteter%20gir%20mer%20stabile,for%C3%A5rsaket%20av%20lakselus%20og%20r%C3%B8mminger. Updated 31.03.2021.

Lader, P., Kristiansen, D., Alver, M., Bjelland, H. V. and Myrhaug, D. (2017), Classification of aquaculture locations in Norway with respect to wind wave exposure, *in* 'ASME 2017 36th International Conference on Ocean, Offshore and Arctic Engineering', American Society of Mechanical Engineers Digital Collection.

Leenknecht, D. A., Szuwalski, A. and Sherlock, A. R. (1992), Automated coastal engineering system: Technical reference. Ch.1: Windspeed adjustment and wave height, Technical report, Coastal Engineering Research Center, Department of the Army Waterways Experiment Station, Corps of Engineers.

Mathisen, J. and Bitner-Gregersen, E. (1990), 'Joint distributions for significant wave height and wave zero-up-crossing period', *Applied Ocean Research* **12**(2), 93–103.

Newland, D. E. (2012), *An introduction to random vibrations, spectral & wavelet analysis*, Courier Corporation.

NORSOK N-003:2017 (2017), Actions and action effects, Technical report, Standard Norge.

Norwegian Meteorological Institute (2021), eklima.met.no. Last checked 20.03.2021.

NS-EN 1991-1-4:2005+NA:2009 (2009), Eurocode 1: Actions on structures - part 1-4: General actions - wind actions, Technical report, Standard Norge.

NS9415 (2009), Marine fish farms - requirements for site survey, risk analysis, design, dimensioning, production, installation and operation, Technical report, Standard Norge.

ParaView (2021), https://www.paraview.org/. Last checked 24.04.2021.

REEF3D (2020), https://reef3d.wordpress.com/. Last checked 21.04.2021.

Reistad, M., Breivik, Ø., Haakenstad, H., Aarnes, O. J., Furevik, B. R. and Bidlot, J.-R. (2011), 'A high-resolution hindcast of wind and waves for the North Sea, the Norwegian Sea, and the Barents Sea', *Journal of Geophysical Research: Oceans* **116**(C5).

Sjømat Norge (2018), 'Sjømat 2030: Et blått taktskifte'.

Smith, J. M., Sherlock, A. R. and Resio, D. T. (2001), STWAVE: Steady-state spectral wave model user's manual for STWAVE, version 3.0, Technical report, Engineer Research and Development Center.

Stefanakos, C. N. and Eidnes, G. (2014), Transferring wave conditions from offshore to nearshore: The case of nordfold, *in* 'ASME 2014 33rd International Conference on Ocean, Offshore and Arctic Engineering', American Society of Mechanical Engineers Digital Collection.

Stefanakos, C. N., Furevik, B. R., Knutsen, Ø. and Christakos, K. (2020), Nearshore wave modelling in a Norwegian fjord, *in* 'International Conference on Offshore Mechanics and Arctic Engineering', Vol. 84386, American Society of Mechanical Engineers.

Stemsrud, S. R. (2018), Site surveys at Norwegian aquaculture sites, Master's thesis, NTNU.

SWAN (2020). Scientific and technical documentation by the SWAN team (Cycle III version 41.31A).

SWAN: User manual (2016). By the SWAN team.

The World Bank (2013), 'Fish to 2030: prospects for fisheries and aquaculture', http://documents.worldbank.org/curated/en/458631468152376668/Fish-to-2030-prospects-for-fisheries-and-aquaculture. Report number 83177.

Tolman, H. L. et al. (2009), 'User manual and system documentation of wavewatch iii tm version 3.14', *Technical note, MMAB Contribution* **276**, 220.

Vaardal-Lunde, J., Forsström, S., Giske, F.-I. G., Arntsen, M. and Borge, J. (2018), Metocean report. Internal report from analysis on location ALPHA.

van der Westhuysen, A., Zijlema, M. and Battjes, J. (2007), 'Nonlinear saturation-based whitecapping dissipation in SWAN for deep and shallow water', *Coastal Engineering* **54**(2), 151–170.

Wamdi Group (1988), 'The WAM model—A third generation ocean wave prediction model', *Journal of Physical Oceanography* **18**(12), 1775–1810.

Wang, W. (2020), Large-Scale Phase-Resolved Wave Modelling for the Norwegian Coast, PhD thesis, NTNU.

Yan, L. (1987), *An improved wind input source term for third generation ocean wave modelling*, KNMI De Bilt, The Netherlands.

Young, I. R. (1999), *Wind generated ocean waves*, Elsevier.

Appendix

A Basic linear wave theory

The theory in this chapter is based on the work of (Holthuijsen, 2007, chapter 5).

In linear wave theory the water is assumed to be an ideal fluid, i.e. that it is incompressible, have constant density, no viscosity, and the water has a continuous body. In addition, it is assumed that the forces on the water particles are induced only by the gravitation.

The forces from gravitation are fairly small, and the assumptions of incompressibility should therefore hold.

Sea water density and viscocity have variations with salinity and temperature. However, this is on a much larger horizontal scale than the application linear wave theory and the assumption of constant density should therefore hold. This is also the case for vertical variations, but this assumption might be challenged in some special cases, e.g. for river outlets where fresh and salt water are mixed in layers.

Even though sea water can not be said to have no viscosity, the assumption implicates that there are no internal forces induced by the viscosity, and these are usually negligible for the wave lengths considered in linear wave theory.

In order to use the velocity potential, ϕ, the water particles must be irrotational. Vorticity can only be generated by turbulence at the bottom, and penetrates short into the water body. Thus, the assumption of irrotational fluid should hold.

The assumption of continuity might be challenged if there are a lot of air bubbles in the water (typically when waves break). This may form discontinuity, and linear wave theory can not be applied.

It can be derived that the mass balance equation (Laplace equation) is

$$\frac{\delta^2\phi}{\delta x^2} + \frac{\delta^2\phi}{\delta y^2} + \frac{\delta^2\phi}{\delta z^2} = 0, \tag{A.1}$$

where ϕ is the velocity potential function which is defined such that $u = \partial\phi/\partial x$, $v = \partial\phi/\partial y$,

$w = \partial\phi/\partial z$ are the velocities i x-, y-, and z-direction respectively. The potential function is given as

$$\phi = \frac{\omega\zeta_A}{k}\frac{\cosh(k(d+z))}{\sinh(kd)}. \tag{A.2}$$

In linear theory, small amplitude waves are considered, namely that $\zeta_A \ll \lambda = 2\pi/k, \zeta_A \ll d$.

The momentum balance is expressed as

$$\frac{\delta\phi}{\delta t} + \frac{p}{\rho_s} + gz = 0, \tag{A.3}$$

which is the linearized Bernoulli equation for unsteady flow. t is time, p is pressure, ρ_s is the density of sea water, g is the gravitational acceleration. In addition we have the kinematic conditions which states that the water particle can not leave the water surface, or penetrate the bottom. The velocities, thus the potential function, will be respectively

$$|\frac{\delta\phi}{\delta z}|_{z=0} = \frac{\delta\zeta}{\delta t}, \tag{A.4}$$

$$|\frac{\delta\phi}{\delta z}|_{z=-d} = 0, \tag{A.5}$$

where d is the water depth and ζ is the surface elevation. Lastly, (A.3) used at two points at the linearized surface gives the dynamic surface boundary condition:

$$|\frac{\delta\phi}{\delta t}|_{z=0} + g\zeta = 0 \tag{A.6}$$

A.1 Linear wave theory with variation of amplitude and phase

For a wave with a varying amplitude as it moves over the surface (3.1) is rewritten as

$$\zeta(x,y,t) = \zeta_A(x,y,t)sin(\omega t + \phi(x,y)), \tag{A.7}$$

where $\zeta_A(x,y,t)$ and is the amplitude varying horizontally and in time, and $\phi(x,y)$ is the phase amplitude varying horizontally.

The potential function is now

$$\phi(x,y,z,t) = \frac{\omega\zeta_A(x,y,t)}{k}\frac{cosh[k(d+z)]}{sinh(kd)}cos(\omega t + \phi(x,y)). \tag{A.8}$$

Laplace, momentum balance, and the dynamic and kinematic conditions are still valid, but solution must be found numerically.

The diffraction parameter is part of the solution, and is defined as

$$\delta_A = \frac{\nabla^2\zeta_A}{k^2\zeta_A} \qquad \text{with} \quad \nabla^2\zeta_A = \frac{\partial^2\zeta_A}{\partial x^2} + \frac{\partial^2\zeta_A}{\partial y^2},$$

where k is the wavenumber, and $\nabla^2\zeta_A$ is the second order spatial derivative of the wave amplitude.

C_w and C_g are the obtained phase- and group velocity with the effect of diffraction, and are derived in the same way as the velocities given by (3.3) and (3.4). These are now

$$C_w = c_w\left(1+\delta_A\right)^{-\frac{1}{2}}, \tag{A.9}$$

$$C_g = c_g\left(1+\delta_A\right)^{\frac{1}{2}}, \tag{A.10}$$

where c_w, c_g are phase- and group velocity without the effect of diffraction. With the same analogy which lead to (3.23) for refraction propagation, the turning rate along the wave rays because of diffraction is

$$\left(\frac{d\theta}{dn}\right)_{dif} = -\frac{1}{C_w}\frac{\partial C_W}{\partial m} = \frac{1}{2(1+\delta_A)}\frac{\partial\delta_A}{\partial m}. \tag{A.11}$$

B Obstacles: Reflection, transmission and absorption of energy

For some sites it might be relevant to include the reflection of waves from obstacles that are smaller than the grid size, for example if there are breakwaters, small islands, cliffs etc. close to the site location. SWAN can reflect wave energy or transmit wave energy over (or through) such structures as illustrated by the figure under, and the difference between transmitted and reflected wave will be the energy absorbed by the obstacle.

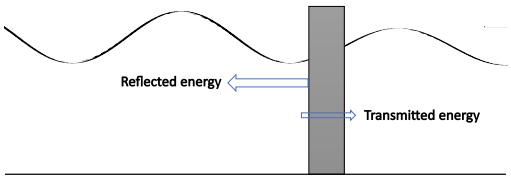

Reflection and transmission of energy off an obstacle.

How much energy is transmitted and reflected is controlled by a coefficient for transmission and reflection respectively. These could e.g. be function of the freeboard over the obstacle as illustrated by the figure under.

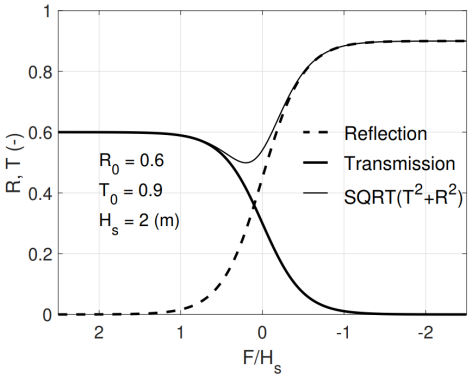

Transmission and reflection coefficient as a function of freeboard, F (*SWAN*, 2020).

SWAN assumes specular reflection, i.e. angle of incoming wave is equal to the reflected wave, and that the wave frequencies remain unchanged. That is, the scale of the spectrum might change, but the shape of it is not affected. Obstacles will also cause diffraction of the waves.

C Coordinates of measuring points

Point	x-coordinate	y-coordinate
Point 1	1.5156°	0.3178°
Point 2	1.5156°	0.4268°
Point 3	1.5156°	0.6754°
Point 4	1.9656°	0.6765°
Point 5	2.3363°	0.3637°
Point 6	2.3363°	0.4267°
Point 7	2.3363°	0.4898°
Point 8	2.7481°	0.4118°
Point 9	2.5138°	0.4202°
Point 10	2.5138°	0.4364°
Point 11	2.5138°	0.4526°
Point 12	2.5615°	0.4201°
Point 13	2.5333°	0.4364°
Point 14	2.5537°	0.4439°
Point 15	2.5740°	0.4364°
Point 16	2.5540°	0.4289°
Point 17	2.5537°	0.4364°

Coordinates of measuring points placed at location Alpha in longitude/latitude. The scaling factors (in kilometer per degree) are 111.5 in x-direction and 41.8 in y-direction.

Point	x-coordinate	y-coordinate
Point 1	1.2950°	0.2290°
Point 2	1.2950°	0.4800°
Point 3	1.9000°	0.4800°
Point 4	1.7900°	0.2700°
Point 5	1.7900°	0.3100°
Point 6	1.8500°	0.3100°
Point 7	1.9943°	0.2284°
Point 8	1.9985°	0.2293°
Point 9	1.9863°	0.2307°

Coordinates of measuring points placed at location Beta in longitude/latitude. The scaling factors (in kilometer per degree) are 111.5 in x-direction and 40.0 in y-direction.

D Bathymetry

		Full area	Nest 1	Nest 2	Nest 3
Alpha	dx	0.007089746°	0.007205432°	0.001031537°	0.0002383459°
	dy	0.002606526°	0.00264824°	0.0003796687°	8.752252e-05°
Beta	dx	0.010033°	0.0030075°	0.0006012°	N/A
	dy	0.0034535°	0.001051°	0.00021006°	N/A

Resolution of bathymetry in location Alpha and Beta in longitude/latitude. The scaling factors (in kilometer per degree) are 111.5 in x-direction and 41.8 in y-direction for location Alpha, and 111.5 in x-direction and 40.0 in y-direction for location Beta.

D.1 bathymetryPlot.m - Plot contour map of bathymetry

```
% Plots the bathymetry (.bty/.bot file) used as input in SWAN
close all
clear all
clc

% Select working and saving directory
workdir = '@jungle';
savedir = '@jungle';
% Bathymetry file
botfile = sprintf('%sbetabathy1.bty',workdir);      % File name
bot_data = load(botfile);                            % Loads file to matrix
% Load measurment points
pointfile = sprintf('%spoints_beta.loc',workdir);
point_data = load(pointfile);

%% Input
% Convert nautical coordinates to cartesian. Not necassary
% when DiveMESH is used
deg2km_y_a=111.535; deg2km_x_a=41.821;  % For ALPHA
deg2km_y=111.549; deg2km_x=40.010;      % For BETA

% Mesh size (SET)
dx=0.010033*deg2km_x;          %  BETA 0.010033 ALPHA 0.007089746
dy=0.0034535*deg2km_y;         %  BETA 0.0034535 ALPHA 0.002606526

% Normalizing the coordinates (SET)
normx=0;
normy=0;

Xstart=0;       % x-coordinate of origion in bty file (SET)
```

```
Ystart=0;       % y-coordinate of origin bty file      (SET)

% Exception value represents land in .bty file
% For DiveMESH, use zero point adjustment code instead
excep_value = -99;
%% Make axis
Xstart_norm=(Xstart-normx)*deg2km_x;    % Normalized start coordinates
Ystart_norm=(Ystart-normy)*deg2km_y;
Nx = size(bot_data,1);                  % number of coordinates in x-direction
Ny = size(bot_data,2);                  % number of coordinates in y-direction
Xend=Xstart_norm+Nx*dx;                 % end x-coordinate
Yend=Ystart_norm+Ny*dy;                 % end y-coordinate
X = Xstart_norm:dx:(Xend-dx);
Y = Ystart_norm:dy:(Yend-dy);
point_data(:,1)=(point_data(:,1)-normx).*deg2km_x;
point_data(:,2)=(point_data(:,2)-normy).*deg2km_y;

%% adjusting zero point from bottom to water level and remove land
% This method shall be used when DiveMESH produce the .bot file

% Xknown=;                      % coordinates where water level is =0
% Yknown=;                      % which can be found from Kartverket
% [~, index_x] = min(abs(X-Xknown));
% [~, index_y] = min(abs(Y-Yknown));
% Zknown = bot_data(index_x, index_y);
% set_level = (Zknown-0);
% bot_data=bot_data-(water_level);
%
%% remove land data
% for i=1:size(bot_data, 1)
%     for j=1:size(bot_data,2)
%         if bot_data(i,j)<set_level
%             bot_data(i,j)=NaN;
%         end
%     end
% end

%% remove exception value
for i=1:size(bot_data, 1)
    for j=1:size(bot_data,2)
        if bot_data(i,j)== excep_value
            bot_data(i,j)=NaN;

        else
            bot_data(i,j)=150;
```

```
        end
    end
end

%%  Plotting
figure()
pcolor(X,Y,bot_data');
hold on
for k=1:length(point_data)
    pointtext=sprintf('%d', k);
    plot(point_data(k,1),point_data(k,2), 'r*'); % plot points from .loc file
      if k>=0 & k<=17 % Set the interval of point that should be enumerated
      text(point_data(k,1)+0.5,point_data(k,2)+0,...
          pointtext, 'color', 'r', 'FontSize', 14);
      end
end
hold off
contourcmap('jet', [0:25:650], 'Colorbar', 'on',...
    'TitleString', 'Depth [m]', 'FontSize', 9)
xlabel('x-coordinate [km]')
ylabel('y-coordinate [km]')
shading flat
saveas(gcf,fullfile(savedir, 'bata'),'epsc');
```

D.2 SOSI_to_XYZ.m - Convert .sosi format to (x,y,z) format

```
% Converts SOSI format depth maps (from Geonorge.no) to a .dat file
% in X- Y-, Z-coord., which, in turn, is used as input to DiveMesh

% Credit to Arun Kamath & Weizhi Wang, NTNU (2017, authors)
% Updated by Benjamin Berntsen for master's thesis (2021)
clear all
clc
close all

% Excerpts
% ...KOORDSYS 23   % UTM sone 33 based on EUREF89/WGS84
% ...ORIGO-NE 0  0 % Coordinates are [N,E], i.e.[y,x]
% ...ENHET 0.01    % Unit and scale, i.e. values*0.01
% ...MIN-NE 7579658  702593
% ...MAX-NE 7634973  735378

Dir='C:\Users\X\Desktop\';
fid=fopen([Dir,'MAP.sos'],'r');
ORIGONE=[0 0];
ENHET=0.01;
mm=0;
nn=0;
DM=-1.99;                   % (m) Distance between sjokartnull
                            % and middel hoybann (HMV) (kystkonturnull)
while ~feof(fid)

    strl=fgets(fid);
    if strfind(strl,'DYBDE') > 0
        d_no=str2num(strl(strfind(strl,' ')+1:end));
        tline=fgetl(fid);
        while sum(strfind(tline,'.'))~=1
            while (sum(strfind(tline,'.')>1) &&...
                    sum(strfind(tline,'.')<=6)) ||...
                    sum(strfind(tline,':'))>0
                tline=fgetl(fid); % skip useless lines
            end

            input=tline;
            N_O=strsplit(input);   % We can't specify which columns
            % to read for coordinates, as the number of digits change,
            % so we separate the lines with space and read the first
            % two parts, which are coordinates
```

```
            mm=mm+1;
            x(mm)=str2num(N_O{2}); % [N,E], namely [y,x], switch them
            y(mm)=str2num(N_O{1});
            d(mm)=d_no;
            tline=fgetl(fid);
        end
    else
        if strfind(strl,'Kystkontur') > 0
            d_ky=DM;
            tline=fgetl(fid);
            while sum(strfind(tline,'.'))~=1
                while (sum(strfind(tline,'.')>1) &&...
                        sum(strfind(tline,'.')<=6)) ||...
                        sum(strfind(tline,':'))>0
                    tline=fgetl(fid); % skip useless lines
                end

                input=tline;
                N_O=strsplit(input);   % We can't specify which columns
                % to read for coordinates, as number of digits change,
                % so we separate the lines with space and read the
                % first two parts, which are coordinates
                mm=mm+1;
                x(mm)=str2num(N_O{2}); %[N,E], namely [y,x], switch
                y(mm)=str2num(N_O{1});
                d(mm)=d_ky;
                tline=fgetl(fid);
            end
        end
    end
end

NP=mm;
fclose(fid);
nxyd=zeros(NP,4); % [point number, north, east and depth coordinates]
for m=1:NP
    nxyd(m,1)=m;
    nxyd(m,2)=x(m)*ENHET+ORIGONE(2); % [N,E], namely [y,x], switch
    nxyd(m,3)=y(m)*ENHET+ORIGONE(1);
    nxyd(m,4)=d(m);
end

%% xyz
maxd=max(nxyd(:,4));
xyz_0=nxyd(:,2:4);
```

```
xyz=[nxyd(:,2) nxyd(:,3) (-nxyd(:,4)+maxd)]; % change the depth
                                             % value to neg.
                                             % and rise to 0

% dlmwrite([Dir,'geo_org.dat'],xyz,'delimiter',' ','precision','%.6f')

fid = fopen(fullfile(Dir,'geobeta1.dat'),'w');
fprintf(fid,'%.8f %.8f %.8f\n',xyz');
fclose(fid);

%% Visualization
tri = delaunay(xyz(:,1),xyz(:,2));
h = trisurf(tri, xyz(:,1),xyz(:,2),xyz(:,3));
%shading interp
view(0,90)
print([Dir,'tromsogfinnmark'],'-dpng')
```

D.3 XYZ_cropping.m - Crop the full map (x,y,z) to chosen dimensions

```
% Crops the XYZ-data from SOSI_to_XYZ.m to chosen dimensions
% Credit to Weizhi Wang, NTNU (2018, author)
% Updated by Benjamin Berntsen for master's thesis (2021)

clear all
clc
close all

% Cropping area
X_start = 387157.0;
X_end = 523996.0;
Y_start = 7545330.0;
Y_end = 7654479.0;

Dir=('C:\Users\X\Desktop\');
A=load([Dir,'MAP.dat']);

%% ROTATION
% ang=-40;
% axang = [0 0 1 ang/180*pi];
% rotm = axang2rotm(axang);
% B=A*rotm;
%
% B(:,1)=B(:,1)+1850;
% B(:,2)=B(:,2)-2500;
%
% figure (1)
% tri = delaunay(B(:,1),B(:,2));
% h2 = trisurf(tri, B(:,1),B(:,2),B(:,3));
% view(0,90)

B=A;

%% Extraction
n=1;
for i=1:length(B)
    if B(i,1)>=X_start && B(i,1)<X_end
        C(n,:)=B(i,:);
        n=n+1;
    end
end
```

```
m=1;
for j=1:length(C)
    if C(j,2)>Y_start && C(j,2)<Y_end
        E(m,:)=C(j,:);
        m=m+1;
    end
end

d=-max(-E(:,3));
E(:,3)=E(:,3)-d;

l=-max(-E(:,1));
L= max(E(:,1));
W= max(E(:,2));
w= -max(-E(:,2));
d=-max(-E(:,3));
D=max(E(:,3));

figure (2)
tri = delaunay(E(:,1),E(:,2));
h2 = trisurf(tri, E(:,1),E(:,2),E(:,3));
view(0,90)
print([Dir,'geo_3'],'-dpng')

%% geo
% dlmwrite([Dir,'geo_3.dat'],E,'delimiter',' ','precision','%.6f')

fid = fopen(fullfile('./','geo_3.dat'),'w');
fprintf(fid,'%.8f %.8f %.8f\n',E');
fclose(fid);
```

D.4 Divemesh control file

```
C 11 6
C 12 3
C 13 3
C 14 7
C 15 21
C 16 3

B 1 50.0
B 10 387157.0 523996.0 7545330.0 7654479.0 0.0 1.0

B 103 5
B 113 2.5
B 116 1.0

G 10 1
G 15 2
G 20 0
G 31 14
G 41 1

M 10 4
M 20 2
```

E Examples of input SWAN files

Example files for the full area grid at each location. Note that some values are replaced with 'XXXX' so the site locations remain anonymous. See the *SWAN: User manual* (2016) for description of all commands.

```
$***************START-UP*********************************************
PROJECT 'ALPHA'
SET level=1.99 NAUTICAL
MODE STATIONARY TWODIMENSIONAL
COORDINATES SPHERICAL CCM

CGRID REGULAR xpc=XXXX ypc=XXXX alpc=0 xlenc=XXXX ylenc=XXXX mxc=499 myc=355 &
CIRCLE mdc=50 flow=0.02 fhigh=0.6 msc=70
$
$*************MODEL DESCRIPTION*************************************
INPGRID BOTTOM REGULAR xpinp=XXXX ypinp=XXXX alpinp=0 mxinp=499 myinp=355 &
dxinp=0.007089746 dyinp=0.002606526 EXCEPTION excval=-99

READINP BOTTOM fac=1 'alphabathy1.bty' idla=5 nhedf=0 FREE
$WIND vel=32 dir=270
$
BOUND SHAPESPEC JONSWAP gamma=7 PEAK POWER
BOUNDSPEC SIDE W CCW CONSTANT PAR hs=14.6 per=17.3 dir=270. dd=22.
$
GEN3 WESTH
BREAKING
TRIADS
FRICTION
DIFFRACTION idiffr=1 smpar=1 smnum=200 cgmod=1
OFF QUADRUPL
$
NUMERIC STOPC STAT  mxitst=200 alfa=0.01
$
$*****************OUTPUT****************************************
POINTS 'alphapo' FILE 'points_alpha.loc'
NGRID 'alpha2' xpn=XXXX ypn=XXXX alpn=0 xlenn=XXXX ylenn=XXXX mxn=270 myn=161
$
BLOCK 'COMPGRID' FILE 'alpha1compgrid.MAT' XP YP DEP HS &
TM01 TM02 TMM10 DIR PDIR DSPR RTP TPS WIND WATLEV BOTLEV SETUP

TABLE 'alphapo' HEADER 'alpha1.tbl' XP YP DEP HS &
TM01 TM02 TMM10 DIR PDIR DSPR RTP TPS WIND WATLEV BOTLEV SETUP

SPECOUT 'alphapo' SPEC1D ABSOLUTE 'alpha1_1D.spc'
NESTOUT 'alpha2' 'alpha1_to_alpha2'
$
```

```
$***************LOCK-UP*****************************************
$
COMPUTE
STOP
```

```
$***************START-UP*****************************************
PROJECT 'BETA'
SET level=3.29 NAUTICAL
MODE STATIONARY TWODIMENSIONAL
COORDINATES SPHERICAL CCM

CGRID REGULAR xpc=XXXX ypc=XXXX alpc=0 xlenc=XXXX ylenc=XXXX mxc=299 myc=333 &
CIRCLE mdc=50 flow=0.02 fhigh=0.6 msc=70
$
$*************MODEL DESCRIPTION***************************************
INPGRID BOTTOM REGULAR xpinp=XXXX ypinp=XXXX alpinp=0 mxinp=299 myinp=333 &
dxinp=0.010033 dyinp=0.0034535 EXCEPTION excval=-99

READINP BOTTOM fac=1 'betabathy1.bty' idla=5 nhedf=0 FREE
$WIND vel=29 dir=0
$
BOUND SHAPESPEC JONSWAP gamma=7 PEAK POWER
BOUNDSPEC SIDE N CCW CONSTANT PAR hs=11.9 per=16.9 dir=310. dd=22.
BOUNDSPEC SIDE W CCW CONSTANT PAR hs=11.9 per=16.9 dir=310. dd=22.
$
GEN3 WESTH
BREAKING
FRICTION
TRIADS
DIFFRACTION idiffr=1 smpar=1 smnum=100 cgmod=1
OFF QUADRUPL
$
NUMERIC STOPC STAT  mxitst=100 alfa=0.01
$
$*****************OUTPUT****************************************
POINTS 'betapo' FILE 'points_beta.loc'
NGRID 'beta2' xpn=XXXX ypn=XXXX alpn=0 xlenn=XXXX ylenn=XXXX mxn=399 myn=425
$
BLOCK 'COMPGRID' FILE 'beta1compgrid.MAT' XP YP DEP HS &
TM01 TM02 TMM10 DIR PDIR DSPR RTP TPS WIND WATLEV BOTLEV SETUP

TABLE 'betapo' HEADER 'beta1.tbl' XP YP DEP HS &
TM01 TM02 TMM10 DIR PDIR DSPR RTP TPS WIND WATLEV BOTLEV SETUP

SPECOUT 'betapo' SPEC1D ABSOLUTE 'beta1_1D.spc'
NESTOUT 'beta2' 'beta1_to_beta2'
$
```

```
$***************LOCK-UP*****************************************
$
COMPUTE
STOP
```

F Scripts for plot of SWAN results

F.1 spcData.m - Read files from SPECOUT command in SWAN

```
function [CDIR_vec,DSPR_vec,VaDens_vec,X, num_of_freq, num_of_loc] = spcDATA(
    file)
% Reads the output from the .spc file into MATLAB
%% Read from file
fid = fopen(file, 'r');                    % Open file for reading
while ~feof(fid)                           % While not end of file
        line_vec = split(fgetl(fid));      % Reads file into cell arrays

        if line_vec{1} == LONLAT
            line_vec=split(fgetl(fid));
            num_of_loc = str2num(line_vec{2});      % Number of locations
        end

        if line_vec{1} == AFREQ
            line_vec=split(fgetl(fid));
            num_of_freq = str2num(line_vec{2});      % Number of freq.
            for i = 1:num_of_freq
                line_vec = split(fgetl(fid));
                rfreq_vec(i) = str2num(line_vec{2}); % Vector of freq.
            end
        end

        if line_vec{1} == m2/Hz                      % Exception values
            line_vec=split(fgetl(fid));
            excep(1) = str2num(line_vec{2});  % excep=[VaDens, CDIR, DSPR]
            for j=1:2
                for i=1:3
                    line_vec=split(fgetl(fid));
                end
                excep(j+1) = str2num(line_vec{2});
            end
        end

        if line_vec{1} == NODATA  % Do not read points without data
```

```
            num_of_loc=num_of_loc-1;
        end

        if line_vec{1} == LOCATION
            for j = 1:num_of_loc
                for i = 1:num_of_freq
                    line_vec = split(fgetl(fid));
                    VaDens_vec(i,j) = str2num(line_vec{2});
                    CDIR_vec(i,j) = str2num(line_vec{3});
                    DSPR_vec(i,j) = str2num(line_vec{4});
                end
                line_vec = fgetl(fid);                % Jump over line
            end
        end
end %while

%% Remove exception values from vectors
% Make separate x-axis
X(1,:)=rfreq_vec; X(2,:)=rfreq_vec; X(3,:)=rfreq_vec;

for j = 1:num_of_loc
    for i =1:num_of_freq
        if VaDens_vec(i,j) == excep(1)
            VaDens_vec(i,j) = NaN;
            X(1,i) = NaN;
        end
        if CDIR_vec(i,j) == excep(2)
            VaDens_vec(i,j) = NaN;
            X(2,i) = NaN;
        end
        if DSPR_vec(i,j) == excep(3)
            DSPR_vec(i,j) = NaN;
            X(3,i) = NaN;
        end
    end %for
end %for
end %function
```

F.2 spcPlot.m - Plot energy spectra at measuring points

```
% Plots output from SPECOUT command in SWAN
close all; clear all; clc;

savedir = @jungle;          % Save directory
workdir = @jungle;          % Working directory

filespc = sprintf('%sbeta1_1D.spc',workdir);          % File name
filespc2 = sprintf('%sbeta2_1D.spc',workdir);         % File name 2
filespc3 = sprintf('%sbeta3_1D.spc',workdir);         % File name 3

% Use spcDATA.m to collect information from .spc file
[CDIR_vec,DSPR_vec,VaDens_vec,X, num_of_freq, num_of_loc]...
    = spcDATA(filespc);
[CDIR_vec2,DSPR_vec2,VaDens_vec2,X2, num_of_freq2, num_of_loc2]...
    = spcDATA(filespc2);
[CDIR_vec3,DSPR_vec3,VaDens_vec3,X3, num_of_freq3, num_of_loc3]...
    = spcDATA(filespc3);

% Plot energy spectrum for all points of File 1
figure()
for j=1:num_of_loc
subplot(ceil(num_of_loc/3),3,j)
plot(X(1,:), VaDens_vec(:,j))
xlabel('Hz')
ylabel('E [m^2/Hz]')
end
% saveas(gcf,fullfile(savedir, 'VaDens'),'fig')

% Plot spectrum at some chosen points
figure()
plot(X(1,:), VaDens_vec(:,1),'k')
hold on
plot(X2(1,:), VaDens_vec2(:,3), '--b')
plot(X3(1,:), VaDens_vec3(:,3), ':k')
xlim([0 0.8])
ylim([0 1200])
xlabel('Hz', 'FontSize', 14)
ylabel('E [m^2/Hz]', 'FontSize', 14)
% saveas(gcf,fullfile(savedir, 'EboundaryBETA'),'epsc')
```

F.3 tabData.m - Read from TABLE command in SWAN

```
function [Xp, Yp, Depth, Hs, Tm01, Tm02, Tm_10, Dir, ...
    PkDir, Dspr, RTpeak, TPsmoo, Wind_x, Wind_y, ...
    Watlev, Botlev, Setup] = tabDATA(file)
% Read output from TABLE command in SWAN

% Scan data from TBL file into MATLAB handles
fid=fopen(file,'r');                              % Open file

% Load data into a matrix
% %f for each column
% #headerlines = #comment lines in top of table file
datain=cell2mat(textscan...
    (fid,'%f %f %f %f %f %f %f %f %f %f %f %f %f %f %f %f %f',...
    'HeaderLines',7,'delimiter','\t'));

% Allocation of data
Xp = datain(:,1); Yp = datain(:,2); Depth = datain(:,3);
Hs = datain(:,4); Tm01 = datain(:,5); Tm02 = datain(:,6);
Tm_10 = datain(:,7); Dir = datain(:,8); PkDir = datain(:,9);
Dspr = datain(:,10); RTpeak = datain(:,11); TPsmoo = datain(:,12);
Wind_x = datain(:,13); Wind_y = datain(:,14); Watlev = datain(:,15);
Botlev = datain(:,16); Setup = datain(:,17);
end
```

F.4 tablePlot.m - Plot properties at measuring points

```
% Plot outputs from the TABLE command in SWAN
clear all; close all; clc;

%% Open .tbl file
workdir = 'C:\Users\Benjamin\Desktop\swanrun\BETA\resolution\';
savedir = 'G:\Min disk\NTNU\5. år\10. semester\Masteroppgave\figures2\';

tabfile1 = sprintf('%sbeta1.tbl',workdir);          % File name
tabfile2 = sprintf('%sbeta2.tbl',workdir);          % File name
tabfile3 = sprintf('%sbeta3.tbl',workdir);          % File name

% Read from .tbl file with tabDATA function
[Xp, Yp, Depth, Hs, Tm01, Tm02, Tm_10, Dir, PkDir, Dspr, RTpeak,...
    TPsmoo, Wind_x, Wind_y, Watlev, Botlev, Setup] = tabDATA(tabfile1);
[Xp2, Yp2, ~, Hs2,Tm012,~,~,~,PkDir2,~,RTpeak2,TPsmoo2,~,~,~,~,~]...
    = tabDATA(tabfile2);
[Xp3, Yp3, ~, Hs3,Tm013,~,~,~,PkDir3,~,RTpeak3,TPsmoo3,~,~,~,~,~]...
    = tabDATA(tabfile3);

%% Store results in new matrix
Hs_new(:,1) = Hs(8:10);
Hs_new(:,2) = Hs2(8:10);
Hs_new(:,3) = Hs3(8:10);
Pk_new(:,1) = PkDir(8:10)-180;
Pk_new(:,2) = PkDir2(8:10)-180;
Pk_new(:,3) = PkDir3(8:10)-180;
%% Plot properties, examples with peak wave dir. and sig. wave height

% Compass plot of peak wave dir. with length of arrow as Hs
figure()
Val=Hs_new(1,:);
u=-sind(Pk_new(1,:)).*Val;
v=-cosd(Pk_new(1,:)).*Val;
c=compass(u,v);
c1 = c(1); c2 = c(2); c3 = c(3); %c4=c(4);
c1.Color = 'k';
c2.Color = 'b';
c3.Color = 'r';
view(90,-90)
lgd=legend('1', '2', '3');
lgd.FontSize=10;
%saveas(gcf,fullfile(savedir, 'compass7HsGRIDwind'),'png')
```

```
% Plot bar of Hs results
figure()
b = bar(Hs_new, 0.7);
b(1).FaceColor='b';
b(2).FaceColor=[0.85 0.32 0.1];
b(3).FaceColor='m';
width = b.BarWidth;
for i=1:length(Hs_new(:, 1))
    row = Hs_new(i, :);
    % 0.7 is approximate net width of white spacings per group
    offset = ((width + 0.7) / length(row)) / 2;
    x = linspace(i-offset, i+offset, length(row));
    row=(round(row,2));
    text(x,row,num2str(row'),'vert','bottom','horiz','center');
end
ax = gca;
%xlabel('Measuring point', 'FontSize', 14)
ylabel('H_s [m]', 'FontSize', 14)
ylim([0 5])
somenames={'7'; '8'; '9'};
set(gca,'xticklabel',somenames)
lgd=legend('Full area', 'Nesting 1', 'Nesting 2');
lgd.FontSize=14;
ax.XGrid = 'off';
ax.YGrid = 'on';
%saveas(gcf,fullfile(savedir, 'HsBETA_RES'),'epsc')
```

F.5 mapPlot.m - Plot contour maps from BLOCK command in SWAN

```
% Plots outputs from BLOCK command in SWAN
%close all; clear all; clc;

workdir = '@jungle'; % Working directory
savedir = '@jungle'; % Save directory
file = sprintf('%sbeta1compgrid.mat',workdir); % File name
Data = load(file);                              % Loads file to matrix

% normx=0;        % For normalizing the coordinates   (SET)
% normy=0;
deg2km_y=111.549; deg2km_x=40.010;    % For BETA
% deg2km_y=111.535; deg2km_x=41.821;  % For ALPHA
Data.Xp=(Data.Xp-normx).*deg2km_x;
Data.Yp=(Data.Yp-normy).*deg2km_y;

% Remove some data for plotting direction arrows
Dir2=Data.Dir(2:14:end, 2:14:end);
PkDir2=Data.PkDir(2:14:end, 2:14:end);
Windx2=Data.Windv_x(2:14:end, 2:14:end);
Windy2=Data.Windv_y(2:14:end, 2:14:end);
Xp2=Data.Xp(2:14:end, 2:14:end);
Yp2=Data.Yp(2:14:end, 2:14:end);

% Decompose direction in x- and y-direction
Dirx=-sind(Dir2);
Diry=-cosd(Dir2);
Pkdirx=-sind(PkDir2);
Pkdiry=-cosd(PkDir2);

%% Plotting (some examples, same method for all properties)
% Singnificant wave height, Hs
figure()
pcolor(Data.Xp, Data.Yp, Data.Hsig)
title('Significant wave height')
xlabel('x-coordinate [m]')
ylabel('y-coordinate [m]')
shading flat
contourcmap('jet', [0:1:17], 'Colorbar', 'on', 'TitleString', 'H_s [m]')
% %saveas(gcf, fullfile(savedir, 'Hsig'),'epsc')

%Hs with arrows pointing in peak wave direction
figure()
```

```
pcolor(Data.Xp, Data.Yp, Data.Hsig)
hold on
q=quiver(Xp2, Yp2, Pkdirx, Pkdiry);
q.Color = 'black';
hold off
title('\theta_{peak}')
xlabel('x-coordinate [km]')
ylabel('y-coordinate [km]')
shading flat
contourcmap('jet',[0:1:17], 'Colorbar', 'on', 'TitleString', 'H_s [m]')
% saveas(gcf,fullfile(savedir, 'beta1compgrid'),'epsc')

% Depth with arrows in wind direction
figure()
pcolor(Data.Xp, Data.Yp, Data.Depth)
hold on
q=quiver(Xp2, Yp2, Windx2, Windy2);
q.Color = 'black';
hold off
title('Wind direction')
xlabel('x-coordinate [km]')
ylabel('y-coordinate [km]')
shading flat
contourcmap('jet', [0:25:650],...
    'Colorbar', 'on', 'TitleString', 'Depth [m]')
% saveas(gcf,fullfile(savedir, 'alpha1_grid1'),'epsc')
```

G Energy spectra results

G.1 ALPHA

G.1.1 Grid resolution study

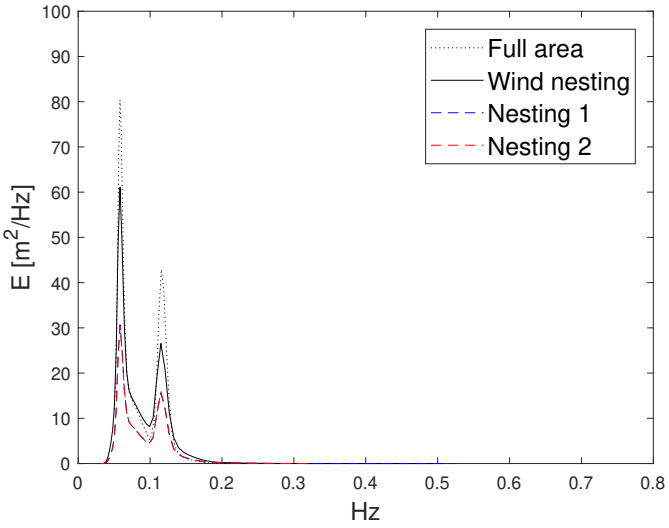

$E(f)$ at measuring point 17 for the inclusion of each nesting at location Alpha.

G.1.2 Computational domain study

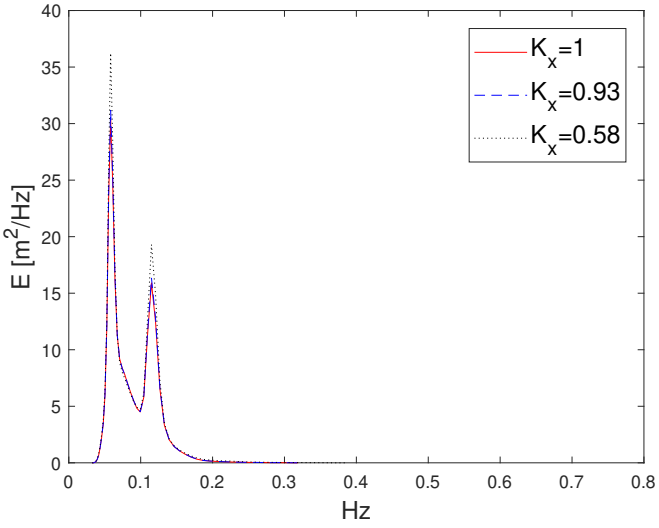

$E(f)$ for various K_x-values at point 17.

G.2 BETA

G.2.1 Grid resolution study

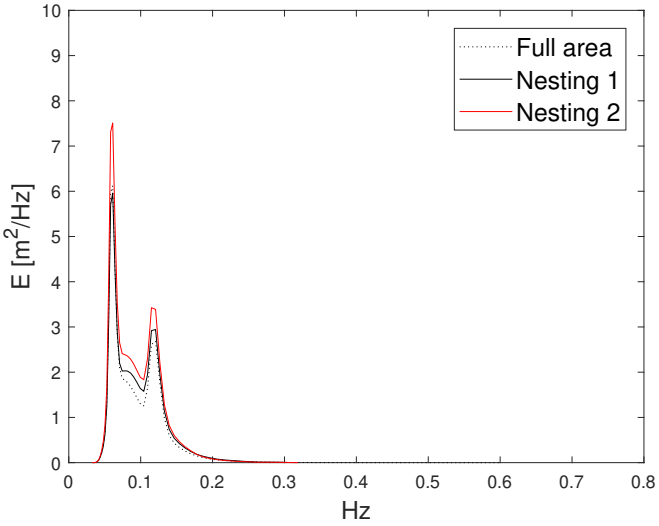

Energy spectrum at measuring point 7 for inclusion of various nesting grids.

G.2.2 Computational domain study

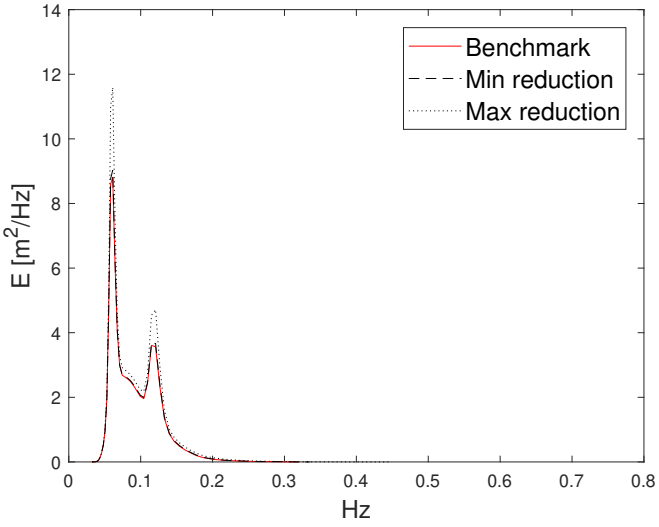

Energy spectrum at measuring point 7 for reduction of computational domain.

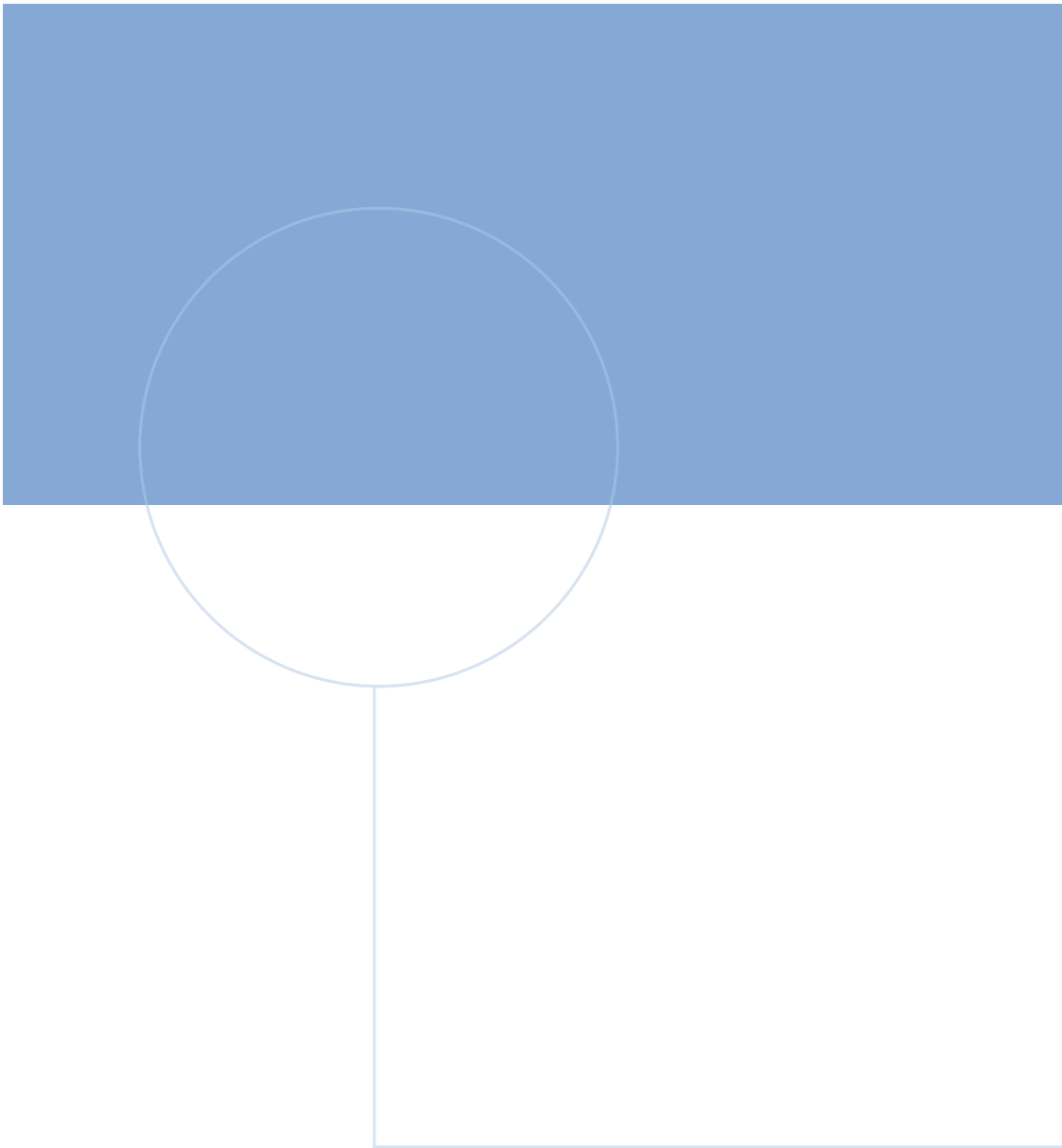

NTNU

Norwegian University of
Science and Technology